UNSTEADY FLOW IN CENTRIFUGAL PUMP AT DESIGN AND OFF-DESIGN CONDITIONS

CHEAH KEAN WEE

(B.Eng, MSc.)

A THESIS SUBMITTED

FOR THE DEGREE OF DOCTOR OF PHILOSOPHY

DEPARTMENT OF MECHANICAL ENGINEERING

NATIONAL UNIVERSITY OF SINGAPORE

2011

ACKNOWLEDGEMENTS

Many people were of great help to me in the completion of my Ph.D thesis. First and foremost, I would like to thank my supervisor Assoc. Prof T.S. Lee. It has been my honour and pleasure to be his student since I was studying for my Master of Science degree. His passion and enthusiasm in research is always a motivational factor for me, even during tough times in the Ph.D. program. Under his guidance, encouragement and supervision, I was able to approach the problems in my research in a more innovative and creative way. I truly appreciate all the time and ideas he has contributed towards completing my research. I am also grateful to have Assoc. Prof S.H. Winoto as my Ph.D research co-supervisor. With his patience and input, it is certainly help to make my research work go further and deeper.

I would like to express my gratitude to Ms. Z.M Zhao and Mr. K.Y Cheoh for their valuable professional advices and engineering inputs which enable this research work to be carried out experimentally.

Finally, I want to thank my family. Without the encouragement and support from my beloved wife Janet, it would be impossible for me to pursuit and complete this Ph.D program. Our always cheerful and joyful children, Eden and Dawn are a powerful source of inspiration. A special thought is devoted to my parents for their never-ending support.

TABLE OF CONTENTS

SUMMARY

Flow inside a centrifugal pump is three-dimensional, turbulent and always associated with secondary flow structures. Understanding the formation and development of the unsteady secondary flow structures from intake section, through centrifugal impeller and volute casing is important to design a high efficiency pump. The current work objectives are to study the inlet flow structures and strong impeller volute interaction in a centrifugal pump with a shrouded impeller that has six twisted blades by using a three-dimensional Navier-Stokes code with a standard k-ε two-equation turbulence model at design point and off-design points.

The steady and unsteady numerically predicted pump performance curves are in good agreement with experimental measurement over a wide range of flow rates. The unsteady numerical simulation at three different flow rates of $0.7Q_{design}$, Q_{design} and $1.3Q_{design}$ show that the inlet flow structure of straight intake section is flow rate dependent. The inflow change its direction either to follow impeller rotation direction at low flow rate or to oppose impeller rotation direction at high flow rate. For curved intake section pump, a pair of counter rotating vortices formed in the curved section before entering into impeller eye regardless of flow rates.

The three-dimensional turbulent flow field in a centrifugal pump is coupled with flow rate and impeller trailing edge relative position to volute tongue. Impeller passage flow at Q_{design} is smooth and follows the curvature of the blade but flow separation is observed at the leading edge due to non-tangential inflow condition. At $0.7Q_{design}$, there is a significant flow reversal and stalled flow near leading edge shroud. At $1.3Q_{design}$, the flow separation occurs on leading edge suction side and being carried downstream in impeller passage.

Analysis on pressure and suction sides of the impeller vanes show that surface streamlines are different in streamwise direction. On the vane pressure side, the streamlines follow the shroud and hub profile well. However, on the suction side, due to leading edge flow separation and flow rate influence, the streamlines are highly distorted near leading and trailing edges.

Counter rotating vortices are observed when flow from impeller discharge into the volute casing circumferentially regardless of flow rates. Streamlines starting from impeller exit near volute tongue and circumferentially advances in streamwise direction form a wrapping vortex tube before approaching volute exit. At $0.7Q_{design}$, there is flow re-entrance to volute tongue region because of negative flow incidence angle. However, wake flow formation behind volute tongue at $1.3Q_{design}$ is like a strong shearing flow due to positive flow incidence angle.

The pressure field depends on flow rate and impeller trailing edge relative position to volute tongue. This is because there is a strong pressure pulsation and change of pressure distribution around the impeller and volute casing when the impeller rotates. The blade pressure distribution difference on the pressure and suction sides of the vanes also depend on flow rate as well.

The leading edge flow separation and recirculation are affecting the distorted flow at impeller exit. This is because the impeller exit flow analysis shows that the wake flow shedding and impingement is strongly affected by the jet wake flow formation within the impeller passage and relative position of blade trailing edge. The jet wake flow pattern inside the impeller passage depends on the flow rates as well.

The impeller exit flow velocity is further resolved into radial and tangential components to study the strong impeller volute tongue interaction. When the impeller

trailing edge is aligned with the volute tongue, the radial velocity coefficient V_r/U_2 increases from suction to pressure side within blade-to-blade passage. However, when the impeller rotates, a reversal of radial velocity coefficient V_r/U_2 is observed around the volute tongue. This sudden reversal of V_r/U_2 can be characterized by the wake flow shedding and impingement.

Based on current work, it can be concluded that the curved intake pump performance is affected by inlet flow structure. Secondary flow in the impeller passage, strong impeller and volute tongue interaction are flow rate dependent.

LIST OF TABLES

LIST OF FIGURES

LIST OF SYMBOLS

A	Cross-sectional Area
b_2	Impeller outlet width
c,C	Meridional flow velocity
c_p	Pressure coefficient($=(p-p_{atm})/0.5\rho U_2^2$)
d_1	Impeller outlet diameter
d_2	Impeller outlet diameter
f_{bp}	Blade passing frequency ($=z\omega/(2\pi)$)
g	Gravity acceleration
h,H	Pump head
L.E.	Leading edge
N	Rotation speed
n_s	Specific speed ($=N\sqrt{Q} / (gH)^{3/4}$)
p,P	Pressure
P.S.	Impeller blade's pressure side
Q	Volume flow rate
r,R	Radius or radius of curvature
r_2,R_2	Impeller outer radius
Re	Reynolds number ($=U_2d_2/\nu$)
Ro	Rossby number ($= W/\omega R$)
S.S.	Impeller blade's suction side
T.E.	Trailing edge

U	Velocity
U_1	Peripheral velocity at impeller inlet
U_2	Peripheral velocity at impeller inlet
U_{ave}	Mean velocity (=Q/A)
U_{tip}	Blade tip velocity (= ωr)
V_r	Radial velocity
W	Relative flow velocity
z	Number of blades
Z	Elevation height

Greek Symbols

β_1	Blade inlet angle [degree]
β_2	Blade outlet angle [degree]
ν	Kinematic viscosity [m^2/s]
ρ	Density of fluid [kg/m^3]
ϕ	Flow coefficient, ($=Q/Nd_2^3$)
ψ	Non-dimensional head coefficient ($=gH/(N_2d_2)^2$)
ω	Rotational speed [rad/s]

CHAPTER 1 INTRODUCTION

1.1 Background

Centrifugal pumps are widely used in industrial and residential applications. Such pumps vary in size, speed, characteristics and materials they are made of. Their fundamental role is to move liquid through a fluid system and to raise the pressure of the liquid. A centrifugal pump can also be considered as energy conversion machine, where the input energy, mostly electrical, is converted to fluid energy by increasing the pressure of the fluid it is pumping.

In today's highly competitive and energy conscious world, emphasis has been placed on developing higher efficiency pumps. This is because every percentage point of efficiency gained can bring significant energy saving over the service life of the pumps. Traditionally, the design of centrifugal pumps is mainly based on the steady-state theory, empirical correlation, combination of models testing and engineering experiences. Pump design references by Stepanoff (1957), Neumann (1991), Gulich (2008), Lazarkiewicz and Troskolanski (1965), Lobanoff and Ross (1992), Wislicenus (1965), are good examples. However, a better understanding of the complex flow field and physics within the pump in order to further improve the pump performance is still needed.

The flow field inside a centrifugal pump is known to be fully turbulent, three-dimensional and unsteady with recirculation flows at its inlet and exit, flow separation, and so on. From the past researches, it showed that rotating impeller with highly complex blade curvature has great influence on the complex flow field developed either within blade passage or inside the vaned or vaneless diffuser volute casing.

Unsteadiness of the flow within the volute casing also arises due to the strong interactions between the impeller and diffuser, or impeller and volute tongue. At off-design condition, either with lower or higher design volume flow rate, the flow field can even change drastically within the pump and make it difficult to design a pump to operate for a long period of time.

Hence, to fully understand and overcome complex flow field within the pump proved to be a real challenge even with the advances of computing power, sophisticated experiments and accurate measurement system.

1.2 Literature Review

Over the past years, experimental works have been done to investigate the complex three-dimensional flow within centrifugal pumps before computational work gains momentum due to advancement of computing power and improved numerical codes.

Before looking into the complex flow field inside a centrifugal pump impeller, it is important to know that how the inflow can actually affects the flow field at impeller eye and later influence the pump performance. This is because ideal inflow condition, either zero incidence flow angle or shockless entry, is difficult to achieve in practice and distorted inlet flow structure is often encountered because of the unsatisfactory intake section design and inflow condition.

Predin and Bilus (2003) tested and analyzed the inflow of a radial impeller pump and found that the whirl flow or pre-rotation flow at the pump entrance pipe changes its direction of rotation. The pre-rotation flow direction that changed at the impeller inlet was caused by different inlet angles of flow. Depending on the flow rate, the pre-

rotation could be followed or opposed of the direction of impeller rotation. Bolpaire and Barrand (1999) and Bolpaire et al (2002) further confirmed that the recirculation flow at impeller inlet at various flow rate by using the LDV measurement. In addition, Kikuyama et al (1992) measured the static pressure changes on the impeller due to the interaction of the vortex caused by inlet swirl. The spiralling asymmetric vortex core induced by swirling flow will cause large unsteady pressure changes on the blade surfaces. Hence, the impeller is subjected to a large fluctuation of the radial force when there is a negative swirl flow.

One of the well known flow phenomena within the radial flow impeller is the "jet wake" flow pattern developed near impeller exit. The flow separation in a centrifugal impeller normally occurs on the suction surface after leading edge and forms a wake flow on the suction side. Early measurement made by Eckartd (1975, 1976) on a vaneless centrifugal compressor impeller found that pronounced jet wake patterns occurred at the exit of the impeller. The flow measurement revealed the on-set of the flow separation in shroud suction corner of the impeller flow passage. After separation on-set, there is a rapid growth of the wake area in the shroud suction-side corner of the flow channel. Similarly, analysis done by Johnson and Moore (1980) on the flow field in a centrifugal pump impeller showing that the development and location of wake flow within the impeller passage is strongly influenced by the Rossby number and by the magnitude of total pressure defect. They showed that when the wake is strong, so that a large secondary vorticity is produced, then inertia would carry the wake beyond its stable location.

The existence of jet wake flow pattern was also found in centrifugal pump impeller. Bwalya and Johnson (1996)'s experimental measurement on a centrifugal

pump impeller at peak efficiency revealed that flow separation on the shroud/pressure corner at leading edge and travelled downstream axially through the impeller to form a wake in shroud/suction corner. At the impeller exit, a reversed radial velocity is observed which is due to high blade sweep angle. However, Howard and Kittmer (1975) experimentally showed that a low flow region occurred at suction tip corner. The measurement by Murakami et al (1980) and Hong and Kang (2002) showed that jet wake flow pattern was flow rate dependent and location of wake zone can change significantly at impeller exit.

The flow field inside the impeller at off-design condition is also very different from at design point. As reported by Pedersen et al (2003), the smooth flow within the impeller at design point changed to a stalled flow at off-design point. A large recirculation cell blocked the inlet flow to the stalled passage while a strong relative eddy dominated the remaining parts of the same passage and causing backflow along the blade pressure side at large radii. Liu et al (1994) experimentally observed that the flow separation occurred on the curvature of blades at off-design condition as well. Due to decrease of flow rate, radial flow decelerated on shroud suction surface, the secondary flow and vorticity increases in the passage. By using laser Doppler anemometer measurement, Abramian and Howard (1994) showed that pressure side mean flow separation under low flow condition within the impeller passage is affected by a combined effect between a secondary vorticity initiated at the inlet and a potential vortex which dominates the flow at impeller exit. The flow within the passage of the highly backward swept blades also dominated by the rotational effect because of the changing Rossby number along the curvature of the blade from leading edge to trailing edge. Other measurements done by Wuibaut et al (2001, 2002), Westra et al (2010), Visser et al (1999), Choi et al (2004,2006) further demonstrated

that flow field within impeller passages is highly complex and depends on flow rate, number of blades, blade curvature and specific speed as well.

As the flow from the impeller is discharged into the non-symmetrical spiral volute casing, which sometimes can be fitted with a vaned diffuser, the strong interaction between the impeller and diffuser or spiral casing is expected. As reported by Gulich and Bolleter (1992) and Morgenroth and Weaver (1998), the unsteadiness arises from the interaction of impeller and casing has great influence on the pump operation such as noise and vibration.

The unsteadiness and pressure pulsation developed due to strong impeller volute interaction even before the pump achieved a stable operating speed. Tsukamoto and Oshashi (1982) and Tsukamoto et al (1986) experimentally and theoretically studied the transient characteristics of a centrifugal pump during rapid starting and stopping period. They found that the dynamic relationship between the flow coefficient and pressure rise coefficient did not always coincide with the one obtained from steady state operation. At the very beginning of the rapid starting period, the total pressure rise tends to become then the quasi-steady value due to impulsive pressure difference. However, for rapid stopping period, the large pressure rise coefficient mainly due to lag in circulation formation around the impeller vanes. Another centrifugal pump transient test made by Lefebvre and Baker (1995) showed that the higher non-dimensional head over the quasi-steady value during start of transient could drastically change after the impulsive pressure decay. The test result suggested that quasi-steady assumptions and methods for impeller design should incorporate the transient effects to improve the performance prediction capabilities.

Kaupert and Staubli (1999) experimentally investigated flow in a high specific speed centrifugal pump impeller and found that pressure fluctuations from the impeller volute interaction grew as the volume flux became further removed from the best efficiency point and as the trailing edge of the impeller approached. These fluctuations reached 35% of the pump head in deep part load. The upstream influence of the volute steady pressure field dominates the unsteady pressure field within the impeller at all off design load points.

Dong et al (1992) and Chu et al (1995) used PIV(Particle Image Velocimetry) technique to measure the velocity within the volute of a centrifugal pump at different impeller blade orientations, for on and off-design conditions to study the effect of impeller-volute tongue interaction. The measurement showed that jet wake structures and pulsating flow near impeller exit and the orientation of the blades could affect the leakage and the pressure distribution. A vortex train was generated as a result of non-uniform out fluxes from the impeller. In addition, Dong et al (1997) demonstrated that pump performance is not affected adversely by increasing the impeller and volute tongue gap up to 20% of impeller radius because of the reduced impact of non-uniform outflux from the flow around the tongue and noise. The shape and location of the volute tongue also significantly affect the pump performance such as the measurement done by Lipski (1979). Al-Qutub et al (2009) experimental study on the radial gap showed that increasing the gap reduces pressure fluctuations particularly at part load conditions. The shape of the trailing edge also produced lower pressure fluctuations while maintaining the same performance. In addition, Parrondo-Gayo et al (2002) experimental measurement, with mounting of pressure transducers on front side of volute circumferentially around impeller outlet, found that pressure fluctuations and amplitudes are to be very dependent on both angular position and

flow rate, with maximum values corresponded to the tongue region for off-design conditions.

As the flow discharge from the impeller exit into volute casing, the highly distorted radial flow, either at design or off-design condition causing unsteadiness flow in the volute casing. The flow inside the volute of a centrifugal pump is three-dimensional and depending upon the location of impeller exit relative to the centre line of volute, a single or double swirling flow occurs. Detailed measurements inside different types of compressor and pump volutes carried out by Van Den Braembussche and Hande (1990), Van den Braembussche et al (1999), Ayder et al (1993, 1994) and Elhom et al (1992) showed that the three-dimensional swirling flow has a form of wrapping layers of non-uniform total pressure and reveals the basic loss mechanism inside the volutes. Because of the dissipation of the kinetic energy at the centre of the swirl, low energy fluid accumulates at the centre of the cross-sections. In addition, the static pressure gradient pushes the fluid of low energy created in the boundary layers towards centre of the swirl. Hagelstein et al (2000) investigation on a rectangular cross section volute showed how the circumferential pressure distortion at off-design operation influences the impeller discharge flow and consequently leads to a circumferential variation of impeller operating point with a variation of total pressure and flow angle and gave further insight into the of three-dimensional swirling flow structures.

The complex flow structures within a centrifugal pump have been investigated both experimentally and analytically as reported in the literature survey above. However, to further improve the pump performances at design and off-design operating conditions, it will become extremely difficult to rely purely on the time

consuming experimental method. Hence with the advancing of computer power, significant improvement of numerical algorithms and more reliable CFD codes, it can be seen that there is an increasing trend of applying numerical methods to study the complex flow in a centrifugal pump and to improve the efficiency. Gulich (1999) discussed the importance of three-dimensional CFD in pump design and factors need to be considered in interpreting the results. A review by Horlock and Denton (2005) suggested that the capabilities of CFD are continually improving and the future of turbomahcinery designs will rely even more heavily on it.

There are several numerical studies to predict the complex impeller and volute interaction based on two-dimensional model such as those by Croba and Kueny (1996) and Morfiadakis et al (1991). For three-dimensional problem, Zhang et al (1996a, 1996b), solved the Navies-Stokes equations coupled with the standard two-equation k-ε turbulence model and found that jet wake structure occurs near the outlet of the impeller and it is independent of flow rate and locations. Their numerical results compared well with those published by Johnson and Moore (1980). He and Sato (2001) also developed a three-dimensional incompressible viscous flow solver and obtained satisfactory agreement with well established experimental data. Byskov et al (2003) investigated a six-bladed impeller with shroud by using the large eddy simulation (LES) at design and off-design conditions. At design load, the flow field inside the impeller is smooth and with no significant separation. At quarter design load, a steady non-rotating stall phenomenon is observed in the entrance and a relative eddy is developed in the remaining of the passage. Their numerical results are in good agreement with Pedersen et al (2003).

Gonzâlez et al (2002) validated the capability of CFD in capturing the dynamics and unsteady flow effects inside a centrifugal pump. The amplitude of the fluctuating pressure field at blade passing frequency is successfully captured for a wide range of flow rates. In addition, with three-dimensional numerical study, Gonzalez and Santolaria (2006) were able to find a plausible explanation for the flow structures inside the pump that is corresponding with the pressure and torque fluctuating values. Gonzalez et al (2009), Spence and Amaral-Teixeira (2008, 2009) even used three-dimensional numerical computations and obtained good agreement between numerical and experimental results for double suction pumps.

Both experimental and numerical investigation of the complex flow field inside a centrifugal pump will contribute to a better understanding of impeller-volute interaction. The explanation on the formation and development of jet wake flow near impeller exit due to strong impeller volute tongue interaction is still unclear. The increase of the overall pump performance can only be achieved if the three-dimensional flow structures and unsteadiness of impeller volute interactions can be correctly modelled and obtained through simultaneous solution of the three-dimensional unsteady Navier-Stokes equations in both the impeller and volute.

1.3 Objective and Scope

The objective of the present work is to numerically investigate the dynamic, unsteady and three-dimensional strong impeller volute casing interaction developed in a centrifugal pump at various operating conditions near its impeller exit. This numerical investigation on the complex flow field inside a centrifugal pump and near impeller exit, can contributes to a better understanding of impeller-volute interaction and the development of jet wake flow.

The centrifugal pump considered in this study consists of shrouded impeller with six backswept blades, a curved and straight intake sections, and a spiral volute casing. The specific speed, n_s of the centrifugal pump is 0.8574 with Reynolds number of $2.15x10^7$ based on the impeller outer diameter and blade tip speed. The impeller blade trailing edge is straight with blade outlet angle β_2 of 23 °. The impeller inlet diameter d_1 is 202 mm and outlet diameter d_2 is 356 mm. The impeller outlet width b_2 is 46.8 mm. The flow from impeller is discharged into a spiral volute casing with mean circle diameter d_3 of 374 mm. The impeller is designed for 1450 rpm with flow coefficient, ϕ of 0.0244 and head coefficient, ψ of 0.1033 at the best the efficiency point.

An industrial open loop test rig was used to obtain the pump characteristics curves of both curved and straight intake section. The test rig arrangement and measurement procedures are followed the ISO 9906 Rotodynamic pumps – Hydraulic performance acceptance tests – Grades 1 and 2. The measurement would include pump head, volume flow rate, motor horse power and net positive suction head for both pumps.

For numerical computation, the centrifugal pump was initially modelled and simulated under steady condition for a wide range of flow rates to obtain the pump characteristic curves which can be compared with the experimental results. Under this steady numerical condition, different eddy viscosity turbulence models such as standard k-ε, RNG k-ε , standard k-ω and Shear Stress Transport (SST) would be compared to study the accuracy of each turbulence model for prediction of global characteristics of the pump. After satisfactory results were obtained for steady condition, an unsteady or transient numerical computation will be carried out at three different flow rate conditions of 70%, 100% and 130% Q_{design}.

In this work, unsteady secondary flow structures at three different locations will be analysed. First, to study the effect of inlet flow structures, the original pump with straight intake section will be replaced with a curved intake section. Figure 1-1 and Figure 1-2 respectively show the meshed model straight and curved intake section pump.

The numerical computation will investigate the inflow structure influences on the flow field within the impeller at design and off-design conditions as well. The analysis will cover flow field in the impeller eye, within the impeller passage and at the impeller exit as well. In this way, the flow field development from leading edge to trailing edge can be captured completely.

Finally, unsteady flow field at impeller and volute exits at design and off-design flow rates will be studied in order to capture the dynamics and strong impeller-volute tongue interaction. This is because the flow field development due to relative position of trailing edge and volute tongue inside the volute casing, flow discharge circumferentially into the volute casing plus volute exit flow pattern is in great interest to understand the secondary flow structures behaviour.

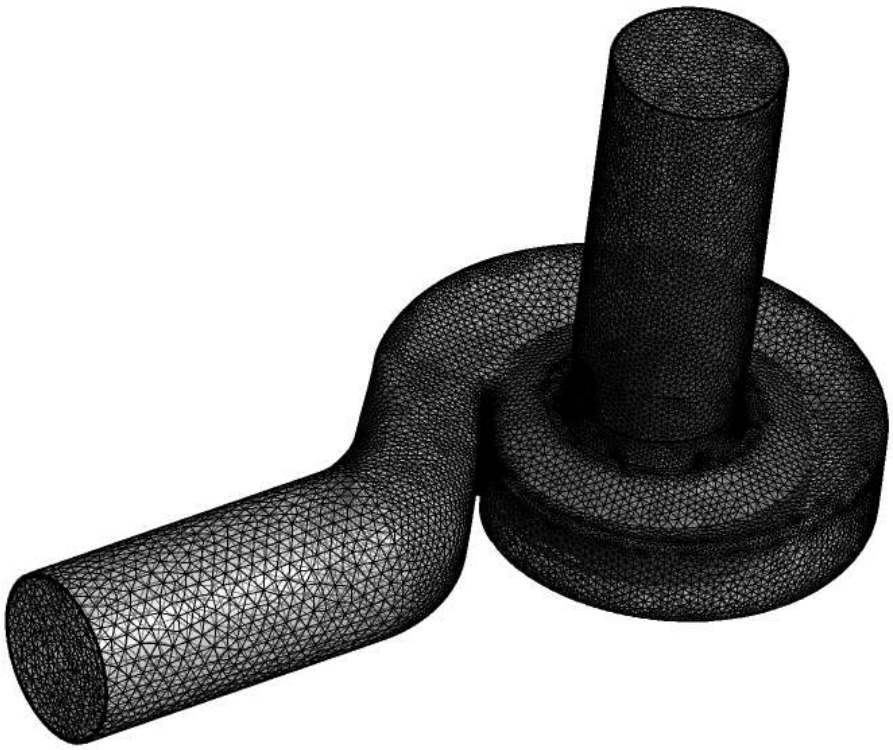

Figure 1-1 Straight intake section centrifugal pump.

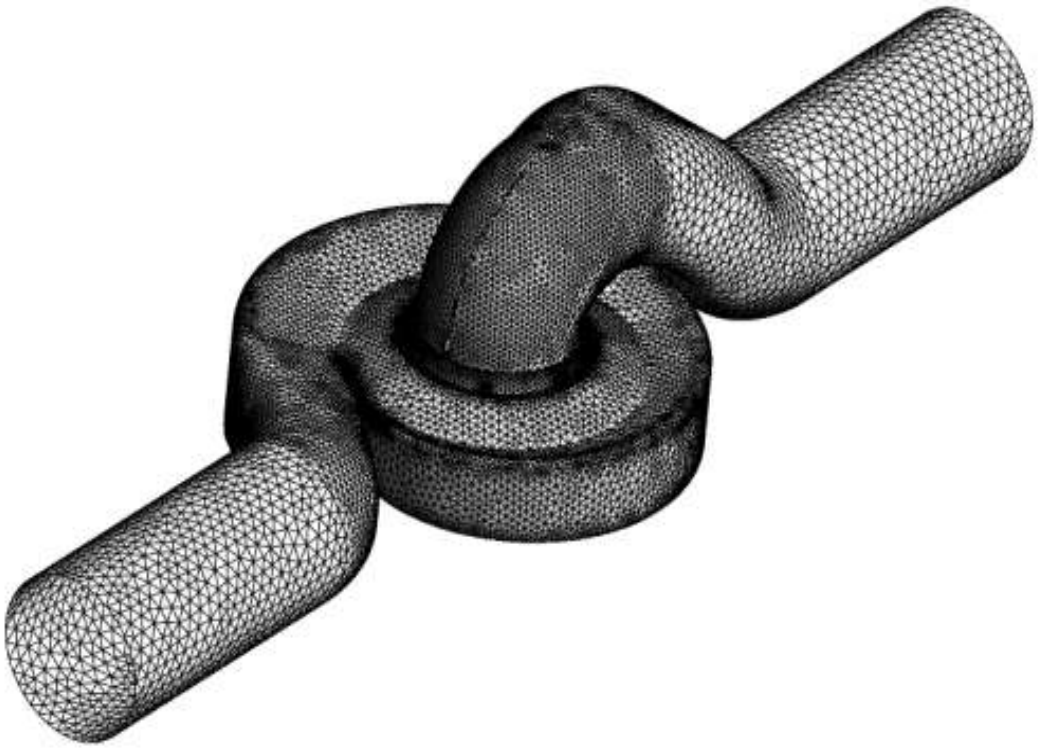

Figure 1-2 Curved intake section centrifugal pump.

CHAPTER 2 NUMERICAL METHOD

2.1 Introduction to CFX Software

A commercially available computational fluid dynamic (CFD) code, CFX 11.0 has been used to study the three-dimensional turbulent flow through the pump at design point and off design point. It is a general purpose CFD code solving three-dimensional Reynolds Averaged Navies-Stokes (RANS) equation for steady or unsteady turbulent fluid flow. This CFD code has been widely used and satisfactory agreements between the numerical and experimental results have been reported. Asuaje et al (2006) performed a quasi-unsteady flow simulation for a centrifugal pump by using the same code and obtained a satisfactory numerical result as compared to test result. The numerical results of Feng et al (2007, 2009) compared well with the PIV and LDV results qualitatively and quantitatively at different operating points for a diffuser pump.

2.2 Mathematical Models

2.2.1 Basic governing equations

For three-dimensional incompressible unsteady flow in stationary frame, instantaneous continuity and momentum equation can be expressed as follows:

Continuity Equation:

$$\frac{\partial \rho}{\partial t} + \nabla \bullet \left(\rho \boldsymbol{u} \right) = 0 \tag{2.1}$$

Momentum Equation:

$$\frac{\partial(\rho \boldsymbol{u})}{\partial t} + \nabla \bullet (\rho \boldsymbol{u} \otimes \boldsymbol{u}) = -\nabla p + \nabla \bullet \tau + \boldsymbol{S}_M \tag{2.2}$$

Where the stress tensor τ , is related to the strain rate by

$$\tau = \mu \left(\nabla \boldsymbol{u} + (\nabla \boldsymbol{u})^T - \frac{2}{3} \delta \nabla \bullet \boldsymbol{u} \right) \tag{2.3}$$

For flow in a rotating frame of reference, rotating at a constant angular velocity, additional sources of momentum are required for the effects of the Coriolis force and the centrifugal force:

$$\boldsymbol{S}_{M,rot} = \boldsymbol{S}_{Cor} + \boldsymbol{S}_{cfg} \tag{2.4}$$

where $\boldsymbol{S}_{Cor} = -2\rho\omega \times \boldsymbol{u}$ (2.5)

$$\boldsymbol{S}_{cfg} = -\rho\omega \times (\omega \times \boldsymbol{r}) \tag{2.6}$$

and where $\boldsymbol{r}$ is the location vector and $\boldsymbol{u}$ is the relative frame velocity.

2.2.2 Reynolds averaged Navier-Stokes (RANS) equations

In general, turbulence models seek to modify the original unsteady Navier-Stokes equations by the introduction of averaged and fluctuating quantities to produce the Reynolds Averaged Navier-Stokes (RANS) equations. These equations represent the mean flow quantities only, while modelling turbulence effects without a need for the resolution of the turbulent fluctuations. All scales of the turbulence field are being modelled. Turbulence models based on the RANS equations are known as Statistical Turbulence Models due to the statistical averaging procedure employed to obtain the equations.

Simulation of the RANS equations greatly reduces the computational effort compared to a Direct Numerical Simulation (DNS) and is generally adopted for practical engineering calculations. However, the averaging procedure introduces additional unknown terms containing products of the fluctuating quantities, which act like additional stresses in the fluid. These terms, called ‘turbulent' or ‘Reynolds' stresses, are difficult to determine directly and so become further unknowns.

The Reynolds (turbulent) stresses need to be modelled by additional equations of known quantities in order to achieve “closure”. Closure implies that there are sufficient number of equations for all the unknowns, including the Reynolds-Stress tensor resulting from the averaging procedure. The equations used to close the system define the type of turbulence model.

As described above, turbulence models seek to solve a modified set of transport equations by introducing averaged and fluctuating components. For example, a velocity $\boldsymbol{u}$ may be divided into an average component $\boldsymbol{U}$ and a time varying component $\boldsymbol{u'}$ that is:

$$\boldsymbol{u} = \boldsymbol{U} + \boldsymbol{u}' \tag{2.7}$$

Where the averaged component $\boldsymbol{U}$ is given by:

$$\boldsymbol{U} = \frac{1}{\Delta t}\int_{t}^{t+\delta t} \boldsymbol{u}.dt \tag{2.8}$$

where Δt is a time scale that is large relative to the turbulent fluctuations, but small relative to the time scale to which the equations are solved. For transient flows, the equations are ensemble-averaged. This allows the averaged equations to be solved for

transient simulations as well. The resulting equations are sometimes called Unsteady Reynolds Averaged Navier-Stokes equations (URANS).

Substituting the averaged quantities into the original transport equations will gives:

$$\frac{\partial \rho}{\partial t} + \nabla \bullet \left(\rho \boldsymbol{U} \right) = 0 \tag{2.9}$$

$$\frac{\partial \left(\rho \boldsymbol{U} \right)}{\partial t} + \nabla \bullet \left(\rho \boldsymbol{U} \otimes \boldsymbol{U} \right) = -\nabla p + \nabla \bullet \left\{ \tau - \rho \overline{\boldsymbol{u}' \otimes \boldsymbol{u}'} \right\} + \boldsymbol{S}_M \tag{2.10}$$

where τ is the molecular stress tensor. Equations above are called Reynolds-averaged Navier-Stokes (RANS) equations. They have the same general form as the instantaneous Navier-Stokes equations, with the velocities and other solution variables now representing time-averaged values. Additional terms now appear that represent the effects of turbulence. These are the Reynolds stress, $-\rho \overline{\boldsymbol{u}' \otimes \boldsymbol{u}'}$. These terms arise from the non-linear convective term in the un-averaged equations. The Reynolds stress must be modelled in order to close Eq. (2.10).

2.2.3 Eddy viscosity turbulence models

In eddy viscosity turbulence models it is suggested that turbulence consists of small eddies which are continuously forming and dissipating, the Reynolds stresses are linked to the velocity gradient via the turbulent viscosity. This relation is called the Boussinesq assumption, where the Reynolds stresses tensor in the time averaged Navier-Stokes equation is replaced by the turbulent viscosity multiplied with the velocity gradients. The eddy viscosity hypothesis assumes that the Reynolds stresses can be related to the mean velocity gradients and eddy (turbulent) viscosity by the

gradient diffusion hypothesis, in a manner analogous to the relationship between the stress and strain tensors in laminar Newtonian flow:

$$-\rho\overline{\boldsymbol{u}'\otimes\boldsymbol{u}'}=\mu_t\left(\nabla\boldsymbol{U}+\left(\nabla\boldsymbol{U}\right)^T\right)-\frac{2}{3}\delta\left(\rho k+\mu_t\nabla\bullet\boldsymbol{U}\right) \tag{2.11}$$

where μ_t is the eddy viscosity or turbulent viscosity. This has to be modelled. The above equations can only express the turbulent fluctuation terms of functions of the mean variables if the turbulent viscosity, μ_t, is known. Both the *k*-ε and *k*-ω two-equation turbulence models provide this variable.

Subject to these hypotheses, the Reynolds averaged momentum and scalar transport equations become:

$$\frac{\partial\left(\rho\boldsymbol{U}\right)}{\partial t}+\nabla\bullet\left(\rho\boldsymbol{U}\otimes\boldsymbol{U}\right)=\boldsymbol{B}-\nabla p'+\nabla\bullet\left(\mu_{eff}\left(\nabla\boldsymbol{U}+\left(\nabla\boldsymbol{U}\right)^T\right)\right)+\boldsymbol{S}_M \tag{2.12}$$

where $\boldsymbol{B}$ is the sum of the body forces, and μ_{eff} is the Effective Viscosity defined by:

$$\mu_{eff}=\mu+\mu_t \tag{2.13}$$

and p' is a modified pressure, defined by:

$$p'=p+\frac{2}{3}\rho k+\frac{2}{3}\mu_t\nabla\bullet\boldsymbol{U} \tag{2.14}$$

2.2.4 Standard k-ε two-equation turbulence model

The *k*-ε use the gradient diffusion hypothesis to relate the Reynolds stresses to the mean velocity gradients and the turbulent viscosity. The turbulent viscosity is modelled as the product of a turbulent velocity and length scale. In *k*-ε model, the

turbulence velocity scale is computed from the turbulent kinetic energy, which is provided from the solution of its transport equation. The turbulent scale is estimated from two properties of the turbulent field, usually the turbulent kinetic energy and its dissipation rate. The dissipation rate of the turbulent kinetic energy is provided from the solution of its transport equation. *k* is the turbulence kinetic energy and is defines as variance of the fluctuation in velocity. ε is the turbulence eddy dissipation. In the *k*-ε turbulence models, the momentum can be written as follow:

$$\frac{\partial(\rho \boldsymbol{U})}{\partial t}+\nabla.(\rho \boldsymbol{U}\otimes \boldsymbol{U})-\nabla.\left(\mu_{eff}\nabla \boldsymbol{U}\right)=\nabla.p'+\nabla.\left(\mu_{eff}\nabla \boldsymbol{U}\right)^{T}+\boldsymbol{S}_{M} \tag{2.15}$$

where μ_{eff} is the effective viscosity accounting for turbulence and *p*' is modified pressure, both defined as:

$$p'=p+\frac{2}{3}\rho k \tag{2.16}$$

and $$\mu_{eff}=\mu+\mu_t \tag{2.17}$$

where μ_t is the turbulence viscosity. The $k-\varepsilon$ model assumes that the turbulence viscosity is linked to the turbulence kinetic energy and dissipation via the relation

$$\mu_t=C_\mu \rho\frac{k^2}{\varepsilon} \tag{2.18}$$

where C_μ is a constant. Its value is 0.09. The values of k and ε come directly from the differential transport equations for the turbulence kinetic energy and turbulence dissipation rate:

$$\frac{\partial(\rho k)}{\partial t}+\nabla\bullet(\rho \boldsymbol{U} k)=\nabla\bullet\left[\left(\mu+\frac{\mu_t}{\sigma_k}\right)\nabla k\right]+P_k-\rho\varepsilon \tag{2.19}$$

$$\frac{\partial(\rho \varepsilon)}{\partial t}+\nabla\bullet(\rho \boldsymbol{U} \varepsilon)=\nabla\bullet\left[\left(\mu+\frac{\mu_t}{\sigma_\varepsilon}\right)\nabla \varepsilon\right]+\frac{\varepsilon}{k}(C_{\varepsilon 1}P_k-C_{\varepsilon 2}\rho\varepsilon) \tag{2.20}$$

where $C_{\varepsilon 1}$ =1.44, $C_{\varepsilon 2}$ =1.92, σ_k =1.0 and σ_ε =1.3 are constants. The P_k in above equations is the turbulence kinetic energy production term, which for incompressible is:

$$P_k=\mu_t\nabla\boldsymbol{U}\bullet\left(\nabla\boldsymbol{U}+\nabla\boldsymbol{U}^T\right)-\frac{2}{3}\nabla\bullet\boldsymbol{U}\left(3\mu_t\nabla\bullet\boldsymbol{U}+\rho k\right) \tag{2.21}$$

For incompressible flow, $\nabla\bullet\boldsymbol{U}$ is small and the second term on the right side of Eq. (2.21) does not contribute significantly to the production term. The term $3\mu_t$ in Eq. (2.21) is based on the "frozen stress" assumption. This prevents the values of *k* and ε becoming too large through shocks, a situation that becomes progressively worse as the mesh is refined at shocks.

2.2.5 The RNG *k*-ε model

The RNG-based *k*-ε turbulence model is derived from the instantaneous Navier-Stokes equations, using a mathematical technique called "renormalization group" (RNG) methods. The analytical derivation results in a model with constants different from those in the standard *k*-ε model, and additional terms and functions in the transport equations for *k* and ε. The transport equations for turbulence generation and dissipation are the same as those for the standard *k*-ε model, but the model constants differ, and the constant $C_{\varepsilon 1}$ is replaced by the function $C_{\varepsilon 1RNG}$.

The transport equation for turbulence dissipation becomes:

$$\frac{\partial(\rho\varepsilon)}{\partial t}+\nabla\bullet(\rho\boldsymbol{U}\varepsilon)=\nabla\bullet\left[\left(\mu+\frac{\mu_t}{\sigma_{\varepsilon RNG}}\right)\nabla\varepsilon\right]+\frac{\varepsilon}{k}(C_{\varepsilon 1RNG}P_k-C_{\varepsilon 2RNG}\rho\varepsilon) \tag{2.22}$$

where:

$$C_{\varepsilon 1RNG}=1.42-f_\eta \tag{2.23}$$

and:

$$f_\eta=\frac{\eta\left(1-\frac{\eta}{4.38}\right)}{1+\beta_{RNG}\eta^3} \tag{2.24}$$

$$\eta=\sqrt{\frac{P_k}{\rho C_{\mu RNG}\varepsilon}} \tag{2.25}$$

2.2.6 The k-ω model

One of the advantages of the *k-ω* formulation is the near wall treatment for low-Reynolds number computations. The model does not involve the complex non-linear damping functions required for the *k-ω* model and is therefore more accurate and more robust. A low-Reynolds k-ω model would typically require a near wall resolution of $y^+<0.2$, while a low-Reynolds number *k-ω* model would require at least $y^+<2$. In industrial flows, even $y^+<0.2$ cannot be guaranteed in most applications and for this reason, a new near wall treatment was developed for the *k-ω* model. It allows for smooth shift from a low-Reynolds number form to a wall function formulation. The *k-ω* model assumes that the turbulence viscosity is linked to the turbulence kinetic energy and turbulent frequency via the relation:

$$\mu_t = \rho \frac{k}{\omega} \tag{2.26}$$

2.2.6.1 The Wilcox *k-ω* model

The starting point of the present formulation is the *k-ω* model developed by Wilcox (1986). It solves two transport equations, one for the turbulent kinetic energy, *k*, and one for the turbulent frequency *ω*. The stress tensor is computed from the eddy-viscosity concept.

k-equation:

$$\frac{\partial(\rho k)}{\partial t} + \nabla \bullet (\rho \mathbf{U} k) = \nabla \bullet \left[\left(\mu + \frac{\mu_t}{\sigma_k} \right) \nabla k \right] + P_k - \beta' \rho k \omega \tag{2.27}$$

ω-equation:

$$\frac{\partial(\rho \omega)}{\partial t} + \nabla \bullet (\rho \mathbf{U} \omega) = \nabla \bullet \left[\left(\mu + \frac{\mu_t}{\sigma_\omega} \right) \nabla \omega \right] + \alpha \frac{\omega}{k} P_k - \beta \rho \omega^2 \tag{2.28}$$

In addition to the independent variables, the density, ρ, and the velocity vector, U, are treated as known quantities from the Navier-Stokes method. P_k is the production rate of turbulence, which is calculated as in the k-ε model. The model constants are given by:

$\beta' = 0.09$

$\alpha = 5/9$

$\beta = 0.075$

$\sigma_k = 2$

$\sigma_\omega = 2$

The unknown Reynolds stress tensor, τ, is calculated from:

$$\tau = \mu_t 2s - \rho \frac{2}{3} \delta k \tag{2.29}$$

2.2.7 The Shear Stress Transport (SST)

The *k*-ω based SST model accounts for the transport of the turbulent shear stress and gives highly accurate predictions of the onset and the amount of flow separation under adverse pressure gradients.

The SST model combines the advantages of the Wilcox and the *k*-ε model, but still fails to properly predict the onset and amount of flow separation from smooth surfaces. The reasons for this deficiency are given in detail in Menter (1994). The main reason is that both models do not account for the transport of the turbulent shear stress. This results in an over prediction of the eddy-viscosity. The proper transport behaviour can be obtained by a limiter to the formulation of the eddy-viscosity:

$$\nu_t = \frac{a_1 k}{\max\left(a_1 \omega, SF_2\right)} \tag{2.30}$$

where

$$\nu_t = \frac{\mu_t}{\rho} \tag{2.31}$$

Again F_2 is a blending function similar to F_1, which restricts the limiter to the wall boundary layer, as the underlying assumptions are not correct for free shear flows. S is an invariant measure of the strain rate.

The blending functions are critical to the success of the method. Their formulation is based on the distance to the nearest surface and on the flow variables.

$$F_1 = \tanh\left(\arg_1^4\right) \tag{2.32}$$

with:

$$arg_1 = \min\left\{\max\left(\frac{\sqrt{k}}{\beta'\omega y}, \frac{500\nu}{y^2\omega}\right), \frac{4\rho k}{CD_{kw}\sigma_{w2}y^2}\right\} \tag{2.33}$$

where y is the distance to the nearest wall, ν is the kinematic viscosity and:

$$CD_{kw} = \max\left(2\rho\frac{1}{\sigma_{w2}\omega}\nabla k\nabla\omega, 1.0\times10^{-10}\right) \tag{2.34}$$

$$F_2 = \tanh\left(\arg_2^2\right) \tag{2.35}$$

with:

$$\arg_2 = \max\left(\frac{2\sqrt{k}}{\beta'\omega y}, \frac{500\nu}{y^2\omega}\right) \tag{2.36}$$

2.2.8 Modelling flow near the wall: Log-law wall functions

When there is non-slip wall boundary condition applied the CFD model solid wall, a log-wall function is employed. In the log-law region, the near wall tangential

velocity is related to the wall shear stress, τ_w by means of a logarithmic relation and is given by:

$$u^+ = \frac{U_t}{u_\tau} = \frac{1}{\kappa}\ln\left(y^+\right) + C \tag{2.37}$$

where $y^+ = \frac{\rho \Delta y u_\tau}{\mu}$ (2.38)

$$u_\tau = \left(\frac{\tau_\omega}{\rho}\right)^{1/2} \tag{2.39}$$

u^+ is the near wall velocity, u_τ is the friction velocity, U_t is the known velocity tangent to the wall at a distance of Δy from the wall, y^+ is the dimensionless distance from the wall, τ_ω is the wall shear stress, κ is the von Karman constant and C is a log-layer constant depending on wall roughness.

In the log-region, an alternative velocity scale u^* can be used instead of u^+:

$$u^* = C_\mu^{1/4} k^{1/2} \tag{2.40}$$

This is because Eq. (2.21) becomes singular at separation points where the near wall velocity, U_t approaches zero. The above scale has the useful property as it does not go to zero even if U_t goes to zero due to the fact that in turbulent flow k is never completely zero. With this relationship, the following explicit equation for u_τ can be obtained:

$$u_\tau = \frac{U_t}{\frac{1}{k}\log\left(y^*\right)+c} \tag{2.41}$$

The absolute value of the wall shear stress τ_ω is then obtained from:

$$\tau_\omega = \rho u^* u_\tau \tag{2.42}$$

where $y^* = \left(\rho u^* \Delta y\right)\big/\mu$ (2.43)

and u^* is as defined earlier by Eq. (2.40)

One of the major drawbacks of the wall-function approach is that the predictions depend on the location of the point nearest to the wall and are sensitive to the near-wall meshing. The problem of inconsistencies in the wall-function, in the case of fine meshes, can be overcome with the use of the Scalable Wall Function. The basic idea behind the scalable wall-function approach is to limit the y* value used in the logarithmic formulation by a lower value of $y'^* = \max\left(y^*, 11.06\right)$. 11.06 is the intersection between the logarithmic and the linear near wall profile. The computed y'^* is therefore not allowed to fall below this limit. Therefore, all mesh points are outside the viscous sublayer and all fine mesh inconsistencies are avoided. The upper limit for y^+ is a function of the device Reynolds number. Nevertheless, a fine near wall spacing is required to ensure a sufficient number of nodes in the boundary layer.

2.3 Computational Grids

For the numerical simulation, an unstructured tetrahedral meshing for all the computational domains is used. The reason of using unstructured mesh in current analysis is due to the complexity and irregular profile of the intake section, impeller

and volute geometry. The meshes of three computational domains, the intake section, impeller and volute casing, are generated separately. The computational domains at the inlet of intake section and outlet of volute section are extended to allow recirculation. The extension is equal to two times of intake inlet and volute outlet diameter, which is the same as the actual pressure measurement location in the test rig. A localized refinement of mesh is employed at regions close to volute tongue area, impeller blade leading and trailing edge in order to accurately capture the flow field structure. This is because the flow field properties variation such as pressure and velocity at these regions are expected to be substantial.

Figure 2-1 shows the mesh assembly of intake, impeller and volute sections. The number of elements used in the numerical simulation is fixed after the mesh independence study. Mesh independence study results will be discussed in later section.

Figure 2-2 shows the plan-view of the pump and the mid-plane is located at z/b = 0.5. Eight cross-sectional planes are cut in according to the various angular locations in volute casing for later discussion. Plane I at 0 ° is closest to volute tongue and the following Plane II to Plane VIII are spaced with an increment of 45 ° in anti-clockwise angular direction up to 315 °. The impeller passages are labelled from 1 to 6 in anti-clockwise direction with Passage 1 closest to the volute tongue. Similarly, the impeller blades are labelled as Blade 1 to 6 in anti-clockwise direction with Blade 1 is between Passage 1 and 6, Blade 2 is between Passage 1 and 2, and so on.

2.4 Boundary Conditions

Boundary conditions are a set of properties or conditions on surfaces of computational domains, and are required to fully define the flow simulation. It is

important, to understand the meaning of well-posed boundary conditions and how to specify it in the CFD model. The boundary conditions are specified in current centrifugal pump simulation are as follows:

2.4.1 Inlet boundary

An inlet boundary condition is used where the flow is predominantly directed into the domain. The absolute inlet pressure is specified because the pressure measurement at the inlet is a known value. Turbulent intensity was specified to be 5%.

2.4.2 Solid walls

Walls are solid (impermeable) boundaries to fluid flow. Walls allow the permeation of heat and additional variables into and out of the domain through the setting of flux and fixed value conditions at wall boundaries. The volute casing and intake section walls are in stationary frame and modelled using a no-slip boundary condition. A scalable wall function is applied.

2.4.3 Outlet boundary

An outlet boundary condition is used where the flow is predominantly directed out of the domain. The hydrodynamic boundary condition specification (that is, those for mass and momentum) for a subsonic outlet involves some constraint on the boundary static pressure, velocity or mass flow. In the simulation, the different mass flow rate at the outlet is specified. However, due to strong recirculation and backflow at the outlet, there will be convergence difficulties if the volute outlet section is not extended.

2.5 Steady Flow Computation

The steady numerical computation is carried out with a multiple frames of reference (MFR) approach because the impeller flow field is with reference to a rotating frame whereby the volute casing and intake section refer to a stationary frame. The dissimilar meshes of the tetrahedral elements of intake section, impeller and volute that generated separately are connected by means of a "Frozen-Rotor" interface. For this kind of interface, the flow field variation across the interface is preserved. For steady calculations the relative position between impeller and volute casing modelled in the inter frames of reference is fixed in time and space. In this case, this Frozen-Rotor interface transfers the non axis-symmetric flow distribution developed only at the given relative position between the impeller and the stationary components to the neighbouring region. Any circumferential flow distribution change due to the variation of the relative position between the impeller and volute casing is not considered in this interface. Although Frozen-Rotor interface is mainly used for the axis-symmetric flow problem, but the fast convergence of this model can save large computational time to obtain the overall pump performance curve. The numerical computation is considered converged when the maximum residual 10^{-4} is reached.

2.6 Unsteady Flow Computation

For the unsteady computation, the dissimilar mesh at the intake, impeller and volute interfaces are connected by means of "Transient Rotor-Stator" interface. For this mesh interface, the surface fluxes of each side of the interface are first computed at the start of each time step at current relative position. The result from the quasi-steady state computation is used to initialize the unsteady computation. The time step of the unsteady computation has been set to 3.4483×10^{-4} second. This time step size is

equivalent to 3° per time step for the rotational speed of the impeller of 1450 rpm. One complete impeller revolution is performed after 120 time steps. The total number of time step is 1320, which is equal to 11 revolutions of the impeller and the total time is 0.45517 second. The chosen time step is sufficient to obtain the necessary time resolution after comparing three different time step sizes. The determination of the time step size and total number of revolutions will be discussed later. The maximum number of iterations in each time step has been set to 10. This number of iterations is sufficient to reduce the maximum residuals by three orders of magnitude.

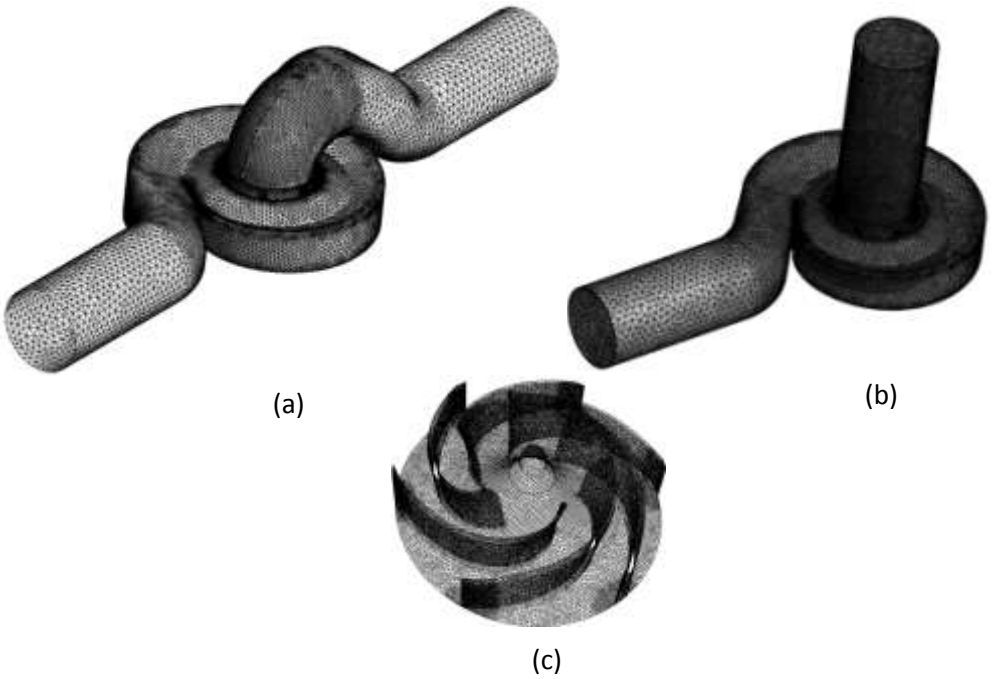

Figure 2-1 Unstructured mesh for the centrifugal pumps (a) curved intake section pump, (b) straight intake section pump, (c) impeller mesh.

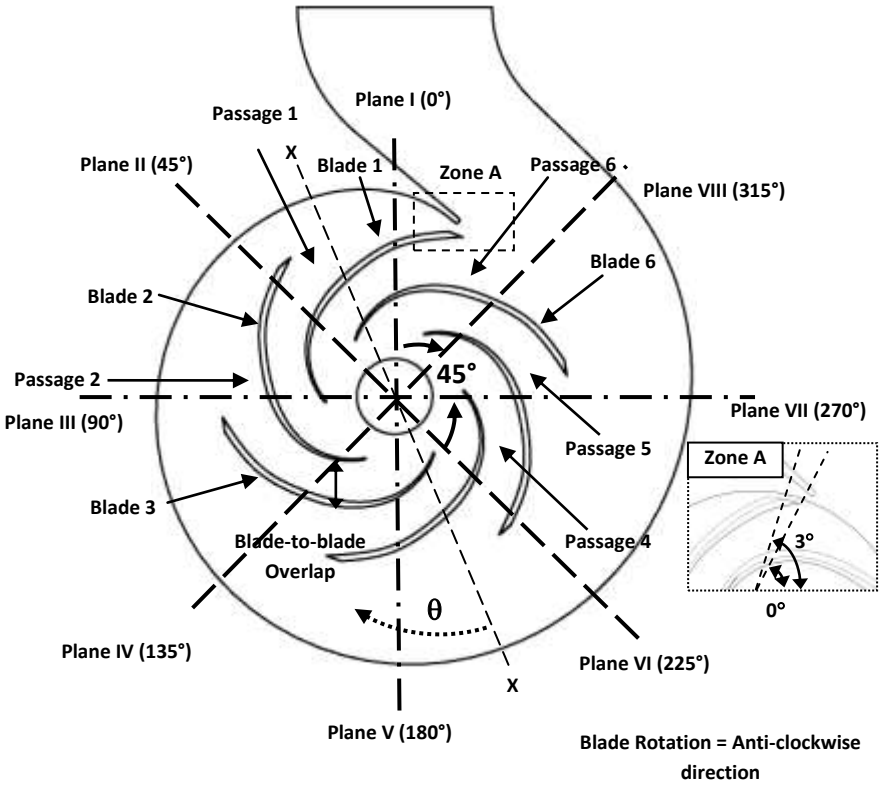

Figure 2-2 Cross-sectional view of the centrifugal pump.

CHAPTER 3 DESCRIPTION OF EXPERIMENT

3.1 Experimental set up

In order to validate the accuracy of numerical computation, it is necessary to conduct an experiment to assess the pump performance. The experimental work was carried out according to the commonly adopted industrial test standard. The centrifugal pump test stand is an open test loop that designed for pumps to be tested in accordance to ISO 9906 Rotodynamic pumps – Hydraulic performance acceptance tests – Grades 1 and 2. The pump performance curve was measured with accuracy according to Grade 2 and the medium of fluid used was clean cold water. Flow rate, pump head, net positive suction head, pump speed and power were measured to plot the pump performance curves.

The pump was tested in standard configuration with pressure transmitters were used at suction and discharge sides to measure the pump head across the pump. The pressure tapping points were located two diameters upstream of the suction flange and two diameters downstream of the discharge flange respectively. The pressure transmitter used was Endress and Hauser Cerebar PMC 731 model. The measurement range of the suction pressure transmitter is -100 to 200 kPa while the discharge pressure transmitter is -0.1 to 4 MPa.

The volume flow rate was measured by a magnetic flow meter, Danfoss MAGFLO MAG3100 series at the downstream of pump and was controlled by a control valve. The accuracy of the magnetic flow meter is 0.25% of the reading and with an output signal of 0~10kHz.

The power was measured by using an Ampere Meter, a Volt Meter and a Power Factor Meter. To measure the pump speed, a magnetic sensor was attached to the pump shaft coupling. An in house designed program was used to collect all the test parameters, as well as to calculate and plot the pump characteristic curves. Figure 3-1 and 3-2 show the industrial test stand and in-house programme used to collect the test data.

The total head at the pump suction section is given by:

$$h_1 = z_1 + \frac{p_1}{\rho g} + \frac{U_1^2}{2g} \tag{3.1}$$

and that at the discharge section

$$h_2 = z_2 + \frac{p_2}{\rho g} + \frac{U_2^2}{2g} \tag{3.2}$$

The pump total head across the pump is the difference between discharge and suction head, that is:

$$H = z_2 - z_1 + \frac{p_2 - p_1}{\rho g} + \frac{U_2^2 - U_1^2}{2g} \tag{3.3}$$

where the mean flow velocity U, is equal to the volume flow rate Q divided by the pipe cross section area A. p_1 and p_2 are the pressure at the suction or discharge respectively.

To accommodate the motor speed fluctuation due to wide flow range operation, it is necessary to translate those data collected according to the affinity law as below:

$$\frac{Q_1}{Q_2} = \frac{N_1}{N_2} \tag{3.4}$$

$$\frac{H_1}{H_2} = \left(\frac{N_1}{N_2} \right)^2 \tag{3.5}$$

$$\frac{P_1}{P_2} = \left(\frac{N_1}{N_2} \right)^3 \tag{3.6}$$

where N is the motor speed , H is the pump head, Q is the volume flow rate and P is motor brake horsepower.

For a three-phase motor, the active power absorbed is given by:

$$P_1 = \frac{P_n}{\eta_m} \tag{3.7}$$

where P_1 is the active motor power uptake at motor terminal, P_n the nominal power output at motor shaft end and η_m the motor efficiency. If the nominal current I_n, nominal voltage V_n and power factor $cos\varphi$ are measured and known, then the P_n can be calculated and the overall pump efficiency can be obtained as follows:

$$P_n = \frac{\sqrt{3}\, I_n\, V_n \cos\varphi}{1000\, \eta_m} \tag{3.8}$$

The overall pump efficiency is calculated based on the pump shaft power, flow rate, total pump head, that is:

$$\eta_{overall} = \frac{\rho g H Q}{P_n} \tag{3.9}$$

Net positive suction head (NPSH) is to measure the energy or head available at the inlet section of the pump to prevent cavitation to occur. NPSH also represents the

difference of the total energy or head at the inlet and the pumping liquid vapour energy. The NPSH available (NPSHa) referred as the head available at the inlet of pump. Assuming that p_v is the vapour pressure at the pumping fluid temperature, the NPSHa at the inlet section of the pump can be calculated as below:

$$NPSHa = \frac{p_{atm} - p_v}{\rho g} \pm h_{suction} - h_{losses} \tag{3.10}$$

The $h_{suction}$ is defined as suction lift when the pumping liquid level is below the pump centreline and as suction head when the liquid surface is above the pump centreline. The h_{losses} is referred to all losses developed from the reservoir towards intake of the pump.

However, NPSH required (NPSHr) is referred to the head required by pump at which the cavitation starts to appear. For industrial test and practical purpose, NPSH3 is commonly adopted. NPSH3 correspond to the degree of cavitation where the associated total head drop is equal to 3% of the normal total head at a particular flow rate.

3.2 Experimental Procedure

To measure the pump performance, the first step is to start the pump with the discharge valve closed after priming the pump. The readings of the flow rate, pump head at suction and discharge, power, motor speed are recorded automatically by using the in house data acquisition program. The test is continued by adjusting the discharge valve for other measurement point until the maximum flow rate. At each flow rate, 3 readings of suction and discharge pressure, rotational speed and input

power were taken within 0.5 second and the mean value is obtained by averaging them.

The NPSH3 test in this case is measured under constant flow rate. By adjusting the suction valve, the head available is reduced. The pump total head will remain constant if the NPSHa is more than the NPSHr. The suction valve is throttled further until there is 3% drop in total pump head and NPSH3 is recorded. This procedure is repeated for other flow rate so that a NPSHr curve is obtained.

A detailed description of the experimental set-up and measurement procedures can be found from the work done by Zhao (2002).

3.3 Results and Discussion

Depending on the specific speed, the slope of the pump characteristics curves can vary from steep to flat. According to the pump design data, the specific speed of the pump is

$$n_s = \frac{N\sqrt{Q}}{(gH)^{3/4}} = 0.8574 \tag{3.11}$$

From this specific number, the pump can be classified as radial flow pump. For radial flow pump, the H-Q curve can be generally characterized as parabolic curve.

Theoretically the pump head can be modelled by Euler head equation which is given by:

$$
\begin{aligned}
H_{th} &= \frac{U_2^2}{g} - \frac{U_2 c_m}{g \tan \beta_2} \\
&= \frac{U_2^2}{g} - \frac{U_2 c_m \cot \beta_2}{g \pi D_2 b_2} Q \\
&= A - BQ
\end{aligned}
\tag{3.12}
$$

According to the Euler head equation, the pump head will reduce linearly as the flow increase. However, due to various losses in the pump, the H-Q is not linear but in parabolic form. Among all the losses, the shock and frictional losses are significantly contributing to shape of the pump performance curve. Shock loss which define as loss arises from the mismatch of flow incidence angle on the vane leading edge and frictional loss which account for energy dissipation due to contact of fluid with solid boundaries are directly proportional to the square of the flow rate. At maximum efficiency, the shock loss is minimal. The mechanical losses such disk frictional and bearing losses do not affect the pump characteristics curve shape but only the input power and the overall efficiency of the pump.

Figure 3-3 shows the pump performance curve for the straight and curved intake section centrifugal pump over the entire flow range at 1450 rpm. For straight intake section pump, the best efficiency point (BEP) of the pump is at flow coefficient ϕ of 0.0243 with a head coefficient ψ of 0.1079. The corresponding efficiency is 79.93%. For the curved intake section pump, the best efficiency point is at flow coefficient ϕ of 0.0244 with a head coefficient ψ of 0.103. The best efficiency is 79.63% which is slightly lower than the straight intake section pump. Even though both pumps have similar efficiency, the head coefficient of curved intake section pump is lower than the straight intake section pump at the same flow coefficient ϕ.

Both pumps are showing stable head-flow rate characteristics where the pump head decreasing progressively from shut-off (zero flow rate) as the flow rate increases, there is always a negative slope with respect to flow rate axis. In addition, the head is a function of flow rate.

The pump efficiency increases in parabolic manner until it reaches a maximum or best efficiency point and then decreases. The highest efficiency of a pump occurs at the flow where the incidence angle of the fluid entering the hydraulic passages best matches with the vane angle. The efficiency decrease can be explained by the fact that the more energy imparted by impeller dissipated into losses within the pump. The shock loss is one of the losses affecting by the change of the inlet flow angle. According to the flow velocity triangle, as the flow rate increases, inlet angle will be more than 90 degree and created pre-rotation of flow in the opposite direction. The other losses that also contribute to this is the frictional loss arises when flow passing the impeller passage.

Figure 3-4 shows the power curve rises to peak and then decreases slowly. The power characteristics of both pumps are the non-overloading type. Non-overloading power characteristics curve means it is impossible for the pump to transmit large power to the liquid after the best efficiency point. In this case, the non-overloading power curve rise up to the peak after best efficiency point and fall slowly.

For practical purpose, it is accepted that NPSHr can be expressed as:

$$NPSHr = C_1 \frac{c_m^2}{2g} + C_2 \frac{u_1^2}{2g} \tag{3.13}$$

C_1 and C_2 are constants that depend on the geometry of the pump, operating condition and fluid properties. Based on the above equation, it is expected that the NPSHr will be proportional to the square power of the flow rate at fixed speed. Figure 3-5 shows the NPSHr measured for straight and curved intake pumps. The pump head and flow rate, NPSHr are normalized with the pump's BEP head and flow rate respectively. It is obvious that the NPSHr increases at a rate of square of the flow rate. The curved intake section pump is using the same impeller design as the straight intake section pump. However, the NPSHr of curved intake pump is slightly higher that straight intake pump, which means that the curved intake pump needs more suction pressure at the intake section to avoid cavitation to occur.

3.4 Concluding Remarks

A comparison of the pump performance in term of head-flow curve, efficiency, power consumption and NPSHr show that there is a difference between the straight intake section and curved intake section pumps. At best efficiency point, the pump head and power absorbed of straight intake section pump is higher than curved intake section pump, by 4% and 3.7% respectively. The efficiency of both pumps only less than 0.4% difference. However, the NPSHr of straight intake section pump is about 42% lower than curved intake section pump.

The impeller and volute casing being used for both pumps are the same design. For straight intake section pump, there is a guide vane, or swirl breaker just before impeller eye. However, for curved intake section pump, the guide vane, a quadrant shape between the inner and outer wall, is dividing the flow equally into the impeller eye. Based on the geometry difference of the both intake sections, it is believed that

pump performance is strongly affected by the flow field and loss mechanism at the inlet of the impeller.

It has been documented in the literature that curved pipe flow will cause secondary flow along and after the curve with the presence of centrifugal forces. According to free vortex flow theory in a curved pipe flow, the pressure is increasing from radially outward from the centre of curvature while the velocity is reducing according to the relationship, VR = constant. Where V is the streamline velocity and R is the radius of curvature of the pipe. Often, flow separation occurs at the inner wall and spiralling cross flow motion appears at the centre of the pipe towards the outer wall. Because of this secondary flow, it is believed that the flow into the impeller eye increases shock loss and reduces the pump head generated for curved intake section pump. The CFD results in later part will explain more the influence of this inlet flow structure on the pump performance.

Figure 3-1 Industrial test rig for experimental work.

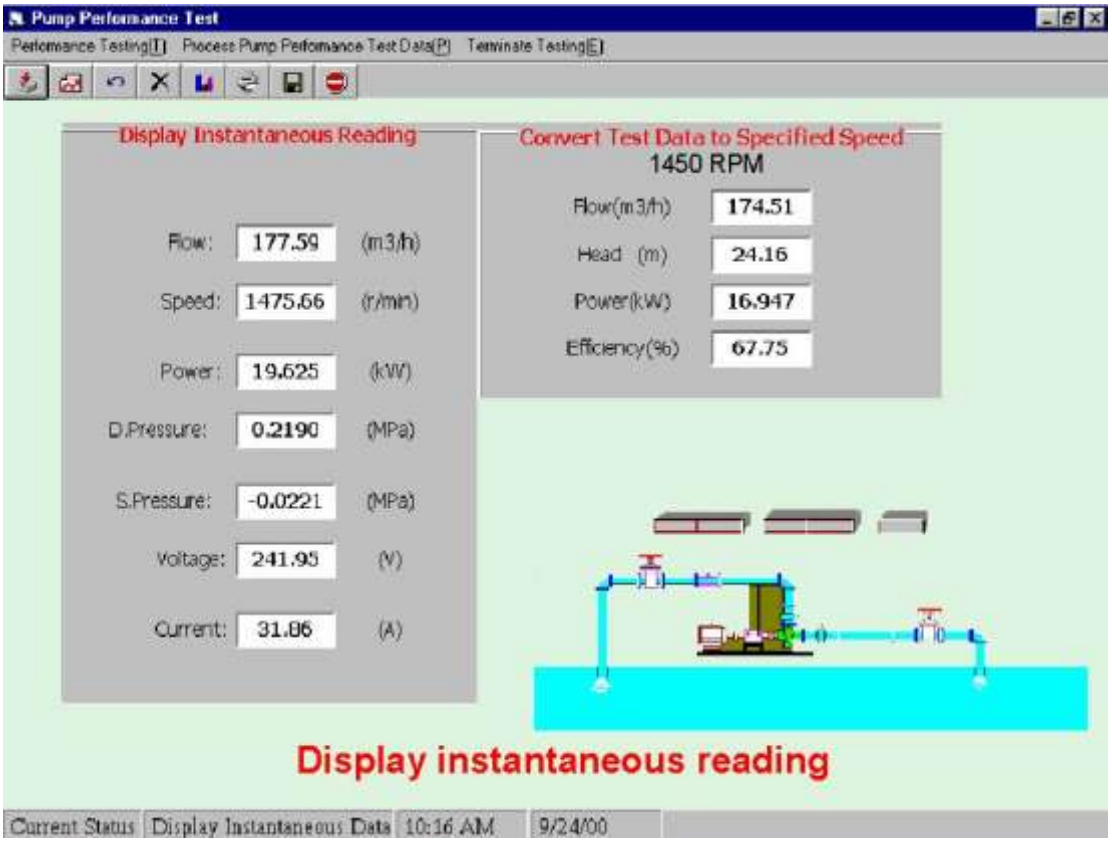

Figure 3-2 In-house developed data acquisition programme.

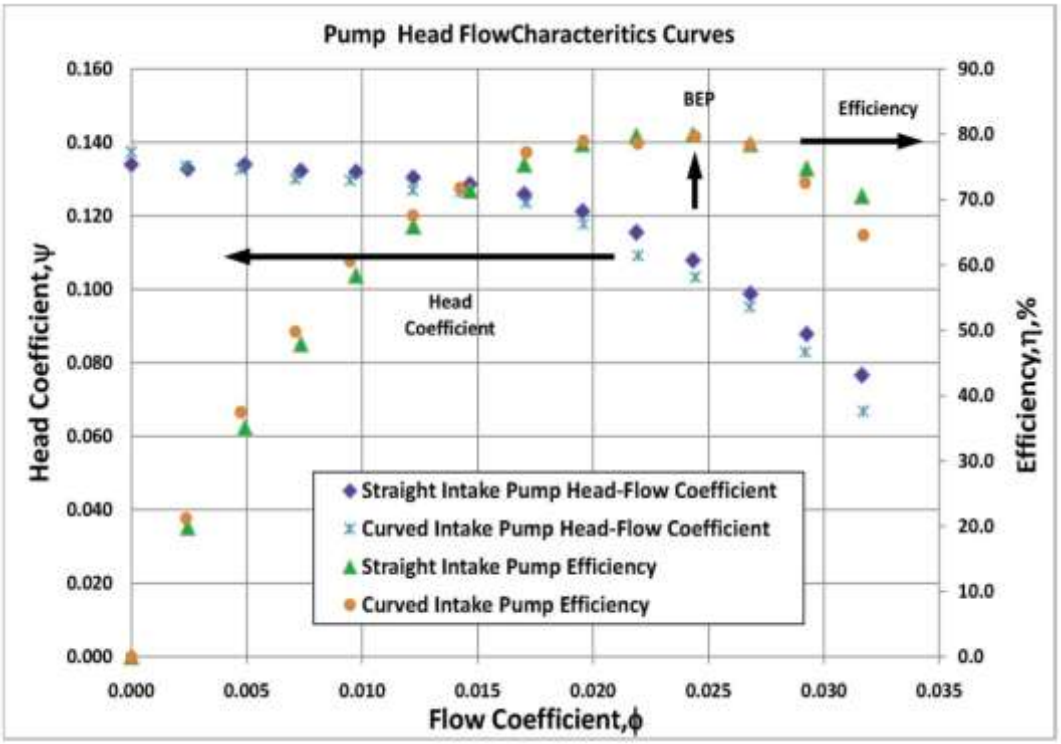

Figure 3-3 Pump performance curves of straight and curved intake section pump.

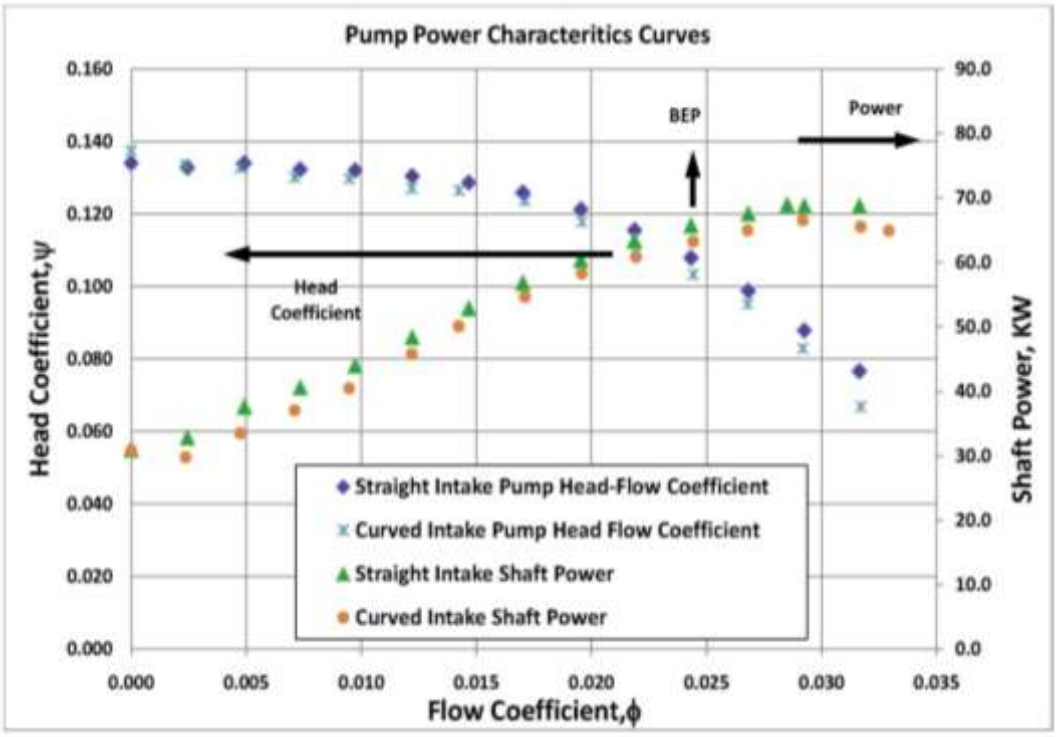

Figure 3-4 Pump power characteristic curves.

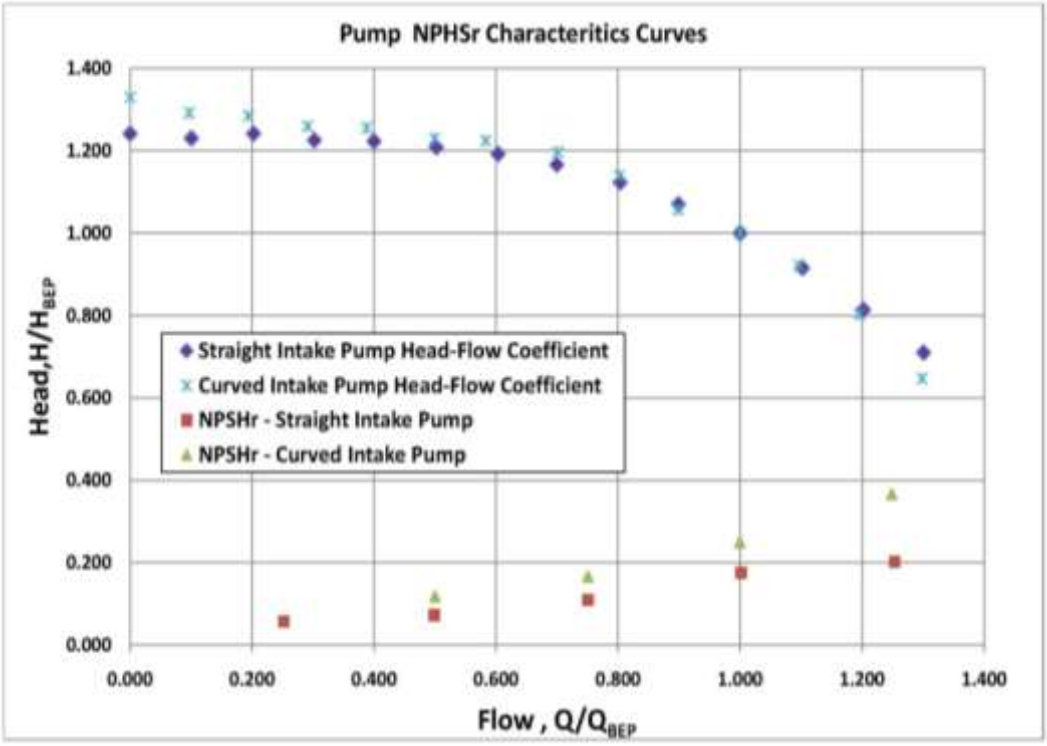

Figure 3-5 NPSHr test for straight and curved intake pumps.

CHAPTER 4 STEADY AND UNSTEADY COMPUTATION

4.1 Steady Computation

As previously discussed in Chapter 2, the steady numerical computation is carried out with a multiple frames of reference approach because the impeller flow field is with reference to a rotating frame whereby the volute casing and intake section refer to a stationary frame. Before discussing any CFD results, it is necessary to check some of the fundamental numerical setting such as the boundary conditions and meshing that could be possibly affects the accuracy of the numerical results.

4.1.1 Inlet and outlet boundary conditions

There are many ways to set the inlet and outlet boundary conditions for numerical simulation of fluid flow in a centrifugal pump. Gonzáez et al (2002) used the total pressure at the inlet and a variable static pressure proportional to the kinetic energy at the outlet for their unsteady pump analysis. For the flow rate, it is changed by modifying the static pressure to kinetic energy ratio at the outlet condition, which simulates different closing positions of a valve. They suggested that although using a fixed flow rate at the inlet provides a better stability and faster convergence, but this condition was found to be less physically correct, because the pressure fluctuations obtained were quite different to the measured ones. Huang (2006) prescribed mass flow rate, 5% turbulence intensity and hydraulic diameter at the inlet of the computational domain. Flow rates at different exits are allocated according to leakage quantity. Miner (2000) specified constant axial velocity at inlet based on the through flow for the pump. The only specification made at the outlet is that the static pressure in the absolute frame is uniform and set to zero.

Table 4-1 shows a comparison of numerical results using different combination of inlet and outlet boundary conditions. There is a difference between outlet and opening type of boundary condition. If there is a flow recirculation at the boundary, the former one does not allow flow entrainment but the later one does allow the flow entrainment. Opening type of boundary condition is useful if there is recirculation and flow entrainment at the outlet of volute. For each set of boundary conditions, it is found that no significant difference for the solution to converge. The first type of boundary condition was chosen as it resembled to actual measurement where the inlet total pressure are known through measurement and the outlet pressure is measured in order to obtain the total pressure rise across the pump with various volume or mass flow rate.

4.1.2 y^+ and mesh sensitivity

To validate the accuracy of the numerical computation, it is important to study the y^+ and the mesh sensitivity of the computation domain. y^+ is defined as the dimensionless distance from the wall and is used to check the location of the first node away from a wall. The same mesh density and turbulence model then should be used to compare the influence of y^+ value.

The k-ε turbulence model is known to be unsuitable for low turbulent Reynolds number computations and ceases to be valid in the vicinity of near-wall region such as viscous sub-layer within the boundary layer flow, where viscous stress is dominant. Complex damping functions can be added to the k-ε model, as well as the requirement of highly refined near-wall grid resolution ($y+ < 0.2$) in an attempt to model this kind of flow. This method often leads to numerical instability. In order to overcome this problem, the wall function approach is preferred to model the flow over near wall

region. In this approach, the viscosity affected sub-layer region is bridged by employing empirical formulas to provide near-wall boundary conditions for the mean flow and turbulence transport equations. Hence, it is unnecessary to fully resolve the flow in this region. In the log-law region, the near wall tangential velocity is related to the wall-shear-stress, τ_w, by means of a logarithmic relation, or more well known to be log-law wall function. These formulas connect the wall conditions such as the wall-shear-stress to the dependent variables at the near-wall mesh node which is presumed to lie in the fully-turbulent region of the boundary layer. The major advantage of the wall function approach is that the high gradient shear layers near walls can be modelled with relatively coarse meshes, yielding substantial savings in computational time and storage. The log law of the wall is applicable for $20 < (y^+) < 300$ and the upper limit of y^+ is Reynolds number dependent. In this current study, the Reynolds number is 2.15×10^7 based on the impeller outer diameter and blade tip speed.

Comparison has been made for the centrifugal pump best efficient point with five different y^+ values within the impeller passage, on the pressure and suction sides of the impeller blades. The y^+ value is changed by adjusting the first node distance from the impeller blades wall while other mesh parameters and density is being kept constant. From Table 4-2, it shows that the head coefficient obtained at design flow rate with less than 0.5% difference for Case (a) and (e) as the y^+ value decreasing. Based on this, it can be said that the y^+ value is adequate for current study and does not have strong effect on the numerical result due the high Reynolds number for the flow within the impeller.

To further confirm the mesh sensitivity, 5 cases with different impeller mesh level as shown in Table 4-3, were studied while keeping the volute casing and intake section mesh level constant, 114045 and 61211 nodes respectively. Again, there is no significant difference between the head coefficient obtained with different mesh levels. Figure 4-1 shows the graph of head coefficient ψ versus y^+ value and mesh density variation. To minimize computation time, the computation of global pump characteristics is carried out using the mesh density of Case (IV), with 151866 nodes and with y^+ value about 250.

4.1.3 Turbulence models

The turbulence models selection and used in this centrifugal pump is based on the comparison of some of the widely used turbulence models in turbomachinery application, such as like *k-ε, k-ω,* RNG *k-ε* and Shear Stress Transport (SST) turbulence models. Two-equation turbulence model k-ε is widely used, as it offers a good compromise between numerical effort and computational accuracy. The RNG *k-ε* model is an alternative to the standard *k-ε* model. In general it offers little improvement compared to the standard *k-ε* model. The *k-ω* model does not involve the complex non-linear damping functions required for the *k-ε* model and considered to be more robust and more accurate. The *k-ω* based Shear-Stress-Transport (SST) model is highly accurate for prediction of the onset and the amount of flow separation under adverse pressure gradients by the inclusion of transport effects into the formulation of the eddy-viscosity.

In this study, the head coefficient is used to gauge the overall accuracy of the turbulence models while the pressure coefficient C_p on the blade is to compare the capability of the turbulence to model the flow characteristics and predict the onset of

flow separation. The C_p is used for the numerical comparison as there is no actual experimental measurement to compare the accuracy of each turbulence model to predict the onset of flow separation. The C_p is defined as:

$$C_p = \frac{p - p_{ref}}{1/2 \rho U_2^2} \tag{4.1}$$

From Table 4-4, the head coefficients obtained with different turbulence models are not significantly different. The *k-ω* turbulence model predicted higher head coefficient than other turbulence models and about 1.3% higher than the *k-ε* turbulence model. However, in terms of convergence speed, *k-ε* turbulence model is faster and more robust. In term of overall pump efficiency, *k-ε* turbulence model is still comparable to *k-ω* turbulence model with only 0.95% difference. Figure 4-2 shows the C_p on the impeller Blade 4 using different turbulence models. It can be seen that there is no significant difference among all the turbulence models. As such, the standard *k-ε* turbulence model is chosen for this study.

4.1.4 Results and discussion

Prior to any discussion of the secondary flow structures developed in the pump, a comparison of the numerical and experimental performance curves for the curved and straight intake pumps are shown in Figure 4-3 and Figure 4-4. The numerical global characteristics curves obtained are based on the steady computation.

The numerically predicted pump characteristic curve over a wide flow range is in good agreement with the experimental results for both curved and straight intake section pumps. The numerically predicted ψ is slightly lower than the experimental

value but the numerically predicted pump efficiency η is slightly higher than experimental value.

For curved intake pump, the numerically predicted ψ is 0.099 as compared to the experimental ψ of 0.103, with a difference of about 4% at the best efficiency point with ϕ of 0.024. At higher flow rate, 130% of Q_{design}, or with ϕ of 0.032, the numerical ψ is 0.064 as compared 0.067, which is 5 % difference. However, at lower flow rate condition, 70% Q_{design}, or ϕ of 0.017, the numerical ψ is 0.114 as compared to 0.123, which is about 7.3% lower.

For straight intake section pump, similar accuracy of numerical result is obtained as well. At best efficiency point, the numerically predicted ψ is 0.104 as compared to experimental ψ of 0.108, with a different of 3.7 %. At 130% Q_{design}, the numerical ψ is 0.074 as compared to experimental value of 0.077, which is 3.9% difference. However, at part load condition, 70% Q_{design}, the numerical ψ is 0.117 as compared to experimental value of 0.126, which is about 7.1% lower.

The curved and straight intake section pumps numerical predicted efficiency is 82.71% and 85.87% respectively. However, the actual pump best efficiencies are at 79.86 % and 79.93 % only. In both cases, the numerically predicted efficiencies are higher than the experimental values. This is because the numerically predicted efficiency only considered the torque within the rotating impeller without taking into account the mechanical and leakage losses arise in the actual pump model. When modelling the centrifugal pump without side spaces and leakage path, the numerical torque is lower than measured shaft torque and this will increase the numerical

efficiency of the centrifugal pump. If disk frictional and leakage losses are included, good agreement between numerical and experimental will be able to achieve.

The computation stopped at 60% of the Q_{design} due to convergence problem caused by large recirculation within the impeller passage and volute casing. At lower flow rate, the difference between the numerical and experimental result is slightly larger and it is believed that the numerical computation is over predicting losses incurred by the highly turbulent and recirculation flow inside the volute. However, it could not match the experimental head one-to-one as reported by Gonzâlez et al (2002), but it has similar accuracy as predicted by Byskov et al (2003).

4.2 Unsteady Computation

In the previous section, the steady numerical computation over the wide range of flow rate showed a good agreement between the numerical and experimental pump performance. However, as the centrifugal pump is operating under a relative high speed condition, the unsteady flow field developed due to impeller and volute tongue interactions is highly turbulent and unsteady. To capture the dynamics and strong impeller volute interaction, it is necessary to carry out an unsteady numerical computation.

As previously discussed in Chapter 2, the result from steady numerical computation is used to initialize the unsteady computation. The total pressure at inlet and mass flow rate boundary conditions are used. For the unsteady computation, the dissimilar mesh at the intake, impeller and volute interfaces are connected by means of “Transient Rotor-Stator” interface. For this mesh interface, the surface fluxes of each side of the interface are first computed at the start of each time step at current

relative position. Hence, it is necessary to investigate and ensure that the time size used is sufficiently fine to capture the flow dynamics.

4.2.1 Impeller revolution convergence and time step size study

As mentioned before, the unsteady computation is initialized from the steady computation. The converged solution of the steady computation will be used as initial condition for the unsteady computation. Blanco-Marigorta et al (2002) revealed that at least 5 impeller revolutions were needed in order to achieve periodic unsteady solution convergence. Majidi (2005) and Gonzalez et al (2002) similarly carried out a numerical investigation on the unsteady flow in centrifugal pumps by using five impeller revolutions. However, for a double suction pump, Gonzalez et al (2009) reported that at least 10 impeller revolutions are needed to achieve similar convergence. Hence, the unsteady computation requires several revolutions before reaching a "steady state" value again.

Not only the number of revolution for unsteady computation is affecting the unsteady computation result, it is also important to have sufficiently small time scale resolution in order to capture the substantial flow field change. This is because time step size selected for numerical computation is affecting the accuracy and stability of the analysis as well. Majidi (2005) used time step size of 2.0243×10^{-4} seconds for the impeller speed of 1482 rpm (=155.22 rad/s) while Gonzalez et al (2002) used 2.94×10^{-4} second for rotational speed of 1620 rpm (=169.65 rad/s). In this case, the pump speed is different, which is 1450 rpm, an appropriate time step size has to be established to obtain satisfactory result.

To study the number of revolutions required to achieve a "steady" value and time step size sensitivity, a total of 11 revolutions and three different time step size of 6.8966×10^{-4}, 3.9943×10^{-4} and 2.2989×10^{-4} seconds that are equivalent to 6 °, 3 ° and 2 ° impeller rotation per time step are being studied. The converged solution from steady computation is used to initialize the unsteady computation.

Figure 4-5 shows the global pump head coefficient fluctuates as the unsteady computation continued from the steady computation solution. The global pump head coefficient is used to judge the revolution convergence of unsteady computation. For the first two revolutions with two degree time step, the head coefficient ψ increases to 0.996 when the unsteady computation is initiated by the steady computation. After that, the head coefficient ψ drops significantly at third and fourth revolution to 0.0968 before increases steadily again to 0.0975. Regardless of different time step sizes, as the number of impeller revolutions increases, the global head coefficient reached a steady value. Based on this study, at least 8 revolutions are needed to achieve a steady-state solution for current pump speed at 1450 rpm.

The periodical global head coefficient is used to judge the time step size sensitivity such that it is sufficient and able to capture the substantial flow field changes due to impeller-volute interaction. Figure 4-6 shows the periodic fluctuating head coefficient at different time step sizes plotted against the relative angular position of impeller Blade 1 from the volute tongue after 11 impeller revolutions. Impeller Blade 1 is the blade that with trailing edge closest to volute tongue as shown in Figure 2-2. Impeller Blade 1 trailing edge initially aligned with volute tongue at 0 °. Relative angular position 0 °, 60 °, 120 °, 180 °, 240 °, and 300 ° are where the impeller Blade 1 trailing edge rotated every 60 ° away from the volute while other blades

trailing is aligned with the volute tongue. Since the impeller has six blades, the pitch of the trailing edge is 60 °. At relative angular position of 30 °, 90 °, 150 °, 210 °, 270 ° and 330 °, the volute tongue is positioned at between two trailing edges.

For 6 ° impeller rotation per time step, the global head coefficient rise and lower smoothly and periodically. When the blade trailing edge is aligned with the volute tongue, the head coefficient is at minimum about 0.097. While the volute tongue is positioned between the blade-to-blade trailing edges, the head coefficient ψ is at maximum about 0.102. So the difference between minimum and maximum head coefficient is 0.005, which is about 5% of the of flow coefficient.

For smaller time step size of 2 ° and 3 °, the global head coefficient fluctuation shows a similar periodic behaviour but captured additional information. The head coefficient rising from lowest point 0.0959 and shows a saddle point after first peak, before reaching the second peak value at 0.1008 which is also about 5% higher. The saddle point before the peak is due to the highly unsteady flow discharged from the impeller exit. There is no significant head coefficient difference between time step of 2 ° and 3 °.

Based on impeller revolution convergence and periodical global head coefficient study, it is concluded that the numerical computational by using 3 ° blade rotation or time step equivalent to 3.9943×10^{-4} second and after 11 impeller revolutions is sufficient to capture the substantial flow field changes

4.2.2 Results and discussion

The unsteady numerical computation is carried out at three different flow rates of $0.7Q_{design}$, Q_{design} and $1.3Q_{design}$ respectively at time step of 3.4483×10^{-4} second or 3 °

per impeller rotation after the impeller revolution convergence and periodical global head coefficient study.

Figure 4-7 shows the head and flow coefficient curve of experimental measurement, steady and unsteady computation. For curved intake section, the numerical predicted head coefficient ψ is about 0.097 as compared to the experimental head coefficient ψ of 0.103, which is about 6% lower. If compared to the steady computation head coefficient ψ which is 0.100, the unsteady head coefficient ψ is only 3% lower. At $1.3Q_{design}$, the head coefficients ψ are 0.060, 0.064 and 0.067 respectively for unsteady computation, steady computation and experimental measurement. For $0.7Q_{design}$, the head coefficients ψ for steady and unsteady computations are 0.117 and 0.114 as compared to experimental value ψ of 0.123. Based on these three different flow rates, the unsteady computation is in good agreement with experimental measurement and follows the head flow curve trend very well.

The straight intake section unsteady computation head coefficient also shows a similar trend with experimental one. Figure 4-8 shows the head and flow coefficient curve of experimental measurement, steady and unsteady computation of straight intake section. For steady and unsteady computation head coefficients ψ are 0.099 and 0.104 as compared to the experimental measurement of 0.108 at Q_{design}. The difference for unsteady computation and experimental head coefficient ψ is about 8%. For $0.7Q_{design}$, the head coefficients ψ for steady and unsteady computations are 0.118 and 0.118 as compared to experimental value of 0.126. At $1.3Q_{design}$, the head coefficients ψ are 0.065, 0.074 and 0.077 respectively for unsteady computation,

steady computation and experimental measurement. The unsteady head coefficient at higher flow rate is slightly lower than the experimental ψ.

From the comparison of Figure 4-7 and Figure 4-8 between the steady and unsteady computation, the steady computation approach can be used to obtain the overall pump performance for less computational time and yet give a reasonable accuracy. However, as mentioned before, for steady calculations the relative position between impeller and volute casing modelled in the inter frames of reference is fixed in time and space. Only the non axis-symmetric flow distribution developed only at the given relative position between the impeller and the stationary components to the neighbouring region. But any circumferential flow distribution change due to the variation of the relative position between the impeller and volute casing is not considered. For unsteady computation, the surface fluxes of each side of the interface are first computed at the start of each time step at current relative position. Hence the rotation of impeller and relative position volute tongue is taking into consideration and strong impeller volute interaction can be studied in details.

Inlet	Outlet	Outlet Boundary Condition Type	ψ
Total Pressure	Mass Flow Rate	Outlet	0.0994
Mass Flow Rate	Total Pressure	Opening	0.0992
Mass Flow Rate	Mass Flow Rate	Outlet	0.0995
Mass Flow Rate	Static Pressure	Outlet	0.0992

Table 4-1 Different inlet and outlet boundary conditions.

y^+ Ave/Case	(a)	(b)	(c)	(d)	(e)
Pressure Side	357	314	250	186	121
Suction Side	381	314	249	184	120
ψ	0.0996	0.0995	0.0994	0.0994	0.0993

Table 4-2 y^+ sensitivity check.

Mesh	(I)	(II)	(III)	(IV)	(IIV)
No. Nodes	88336	102903	122746	151866	190503
ψ	0.0996	0.0995	0.0994	0.0994	0.0993

Table 4-3 Impeller mesh sensitivity check.

	ψ	Overall pump efficiency, η, %
k-ε	0.0994	76.71
RNG k-ε	0.0984	75.88
k-ω	0.1007	77.66
SST	0.1003	77.35

Table 4-4 Turbulence models comparison.

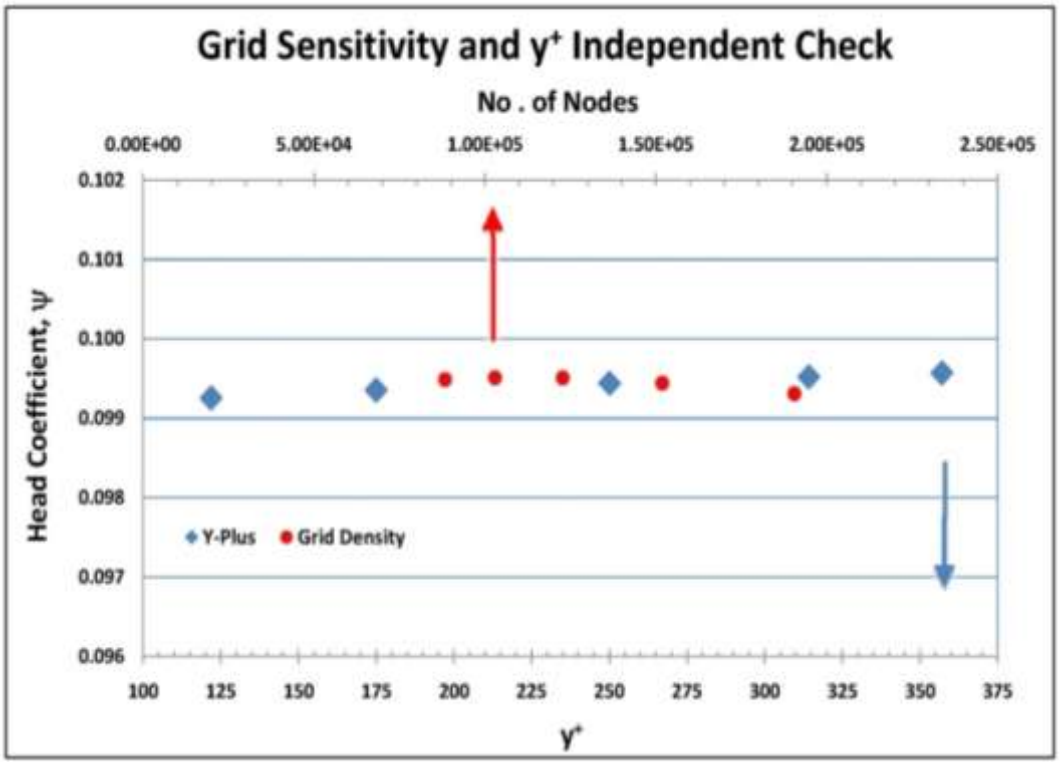

Figure 4-1 Mesh sensitivity and y^+ independent study.

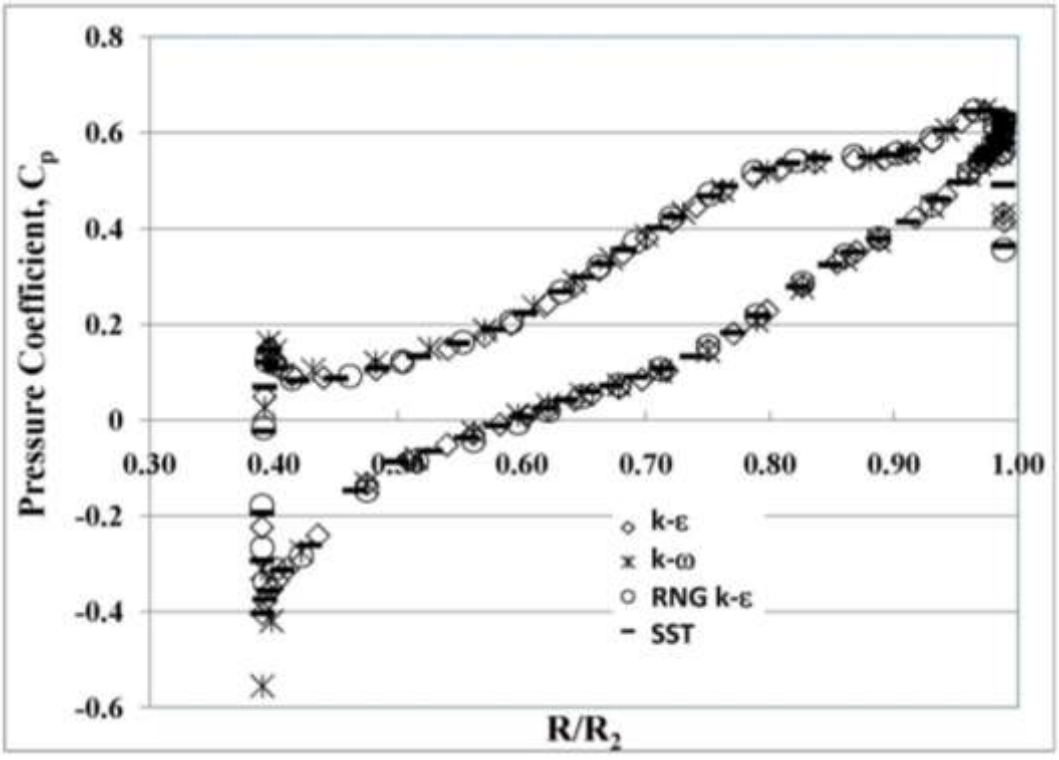

Figure 4-2 Comparison of C_p with different turbulence models.

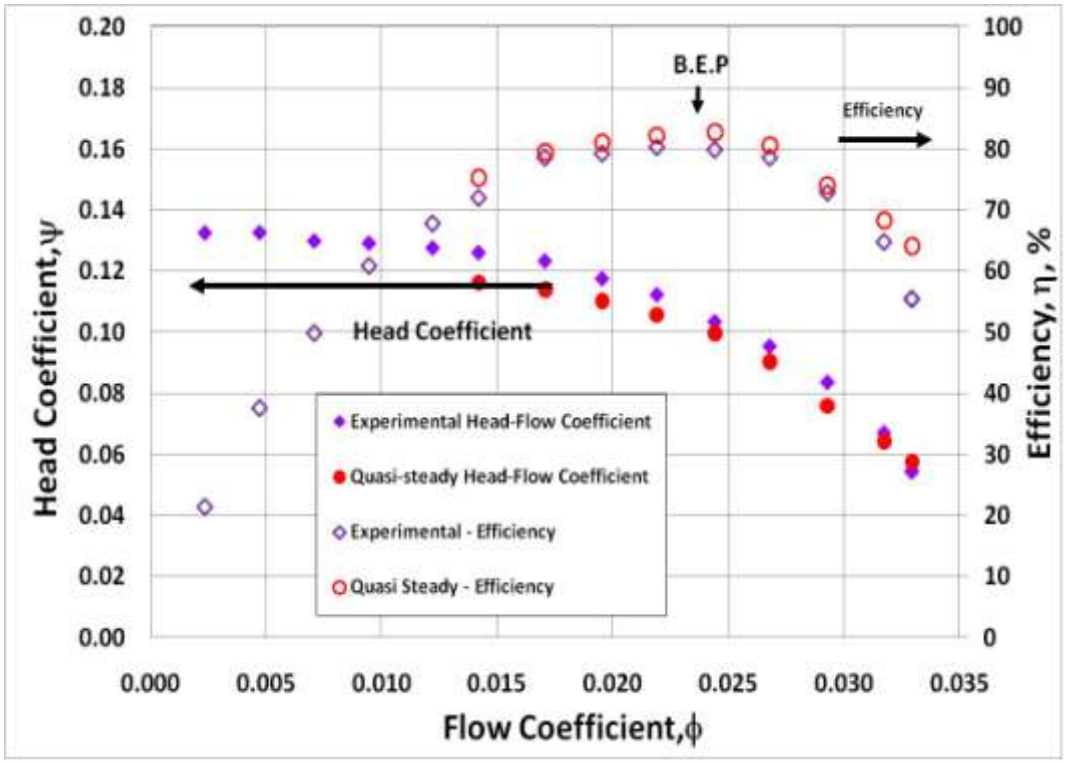

Figure 4-3 Curved intake pump performance curves.

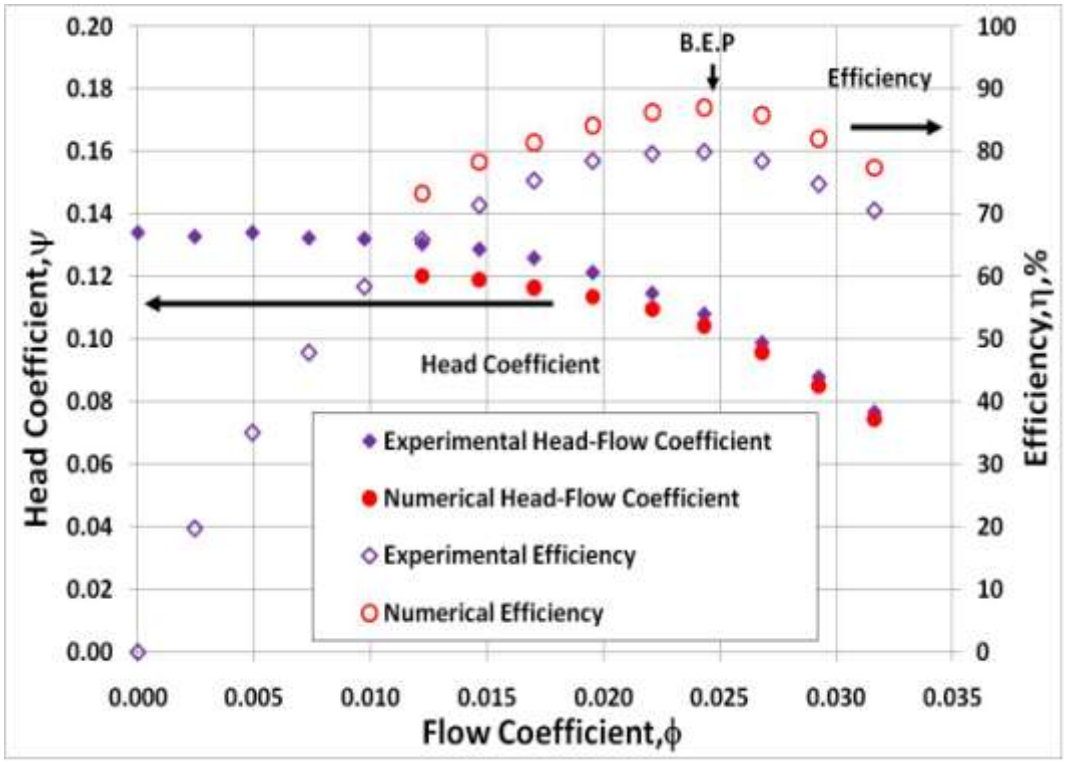

Figure 4-4 Straight intake pump performance curves.

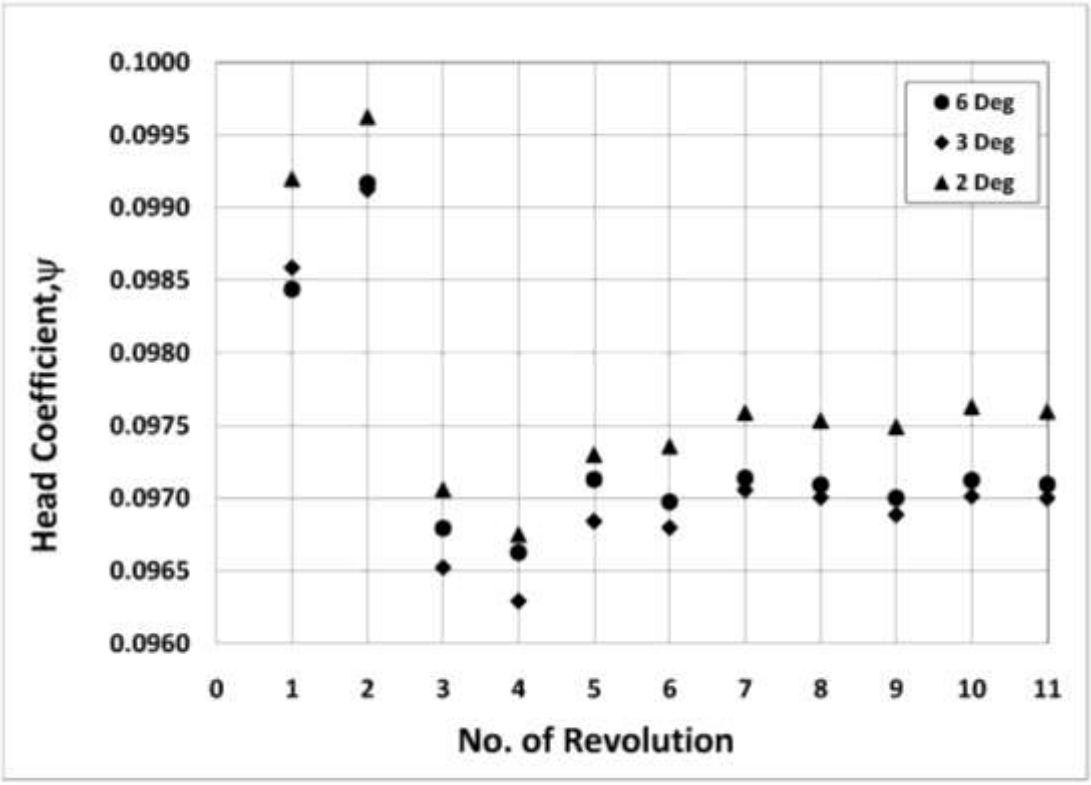

Figure 4-5 Unsteady head coefficient convergence history.

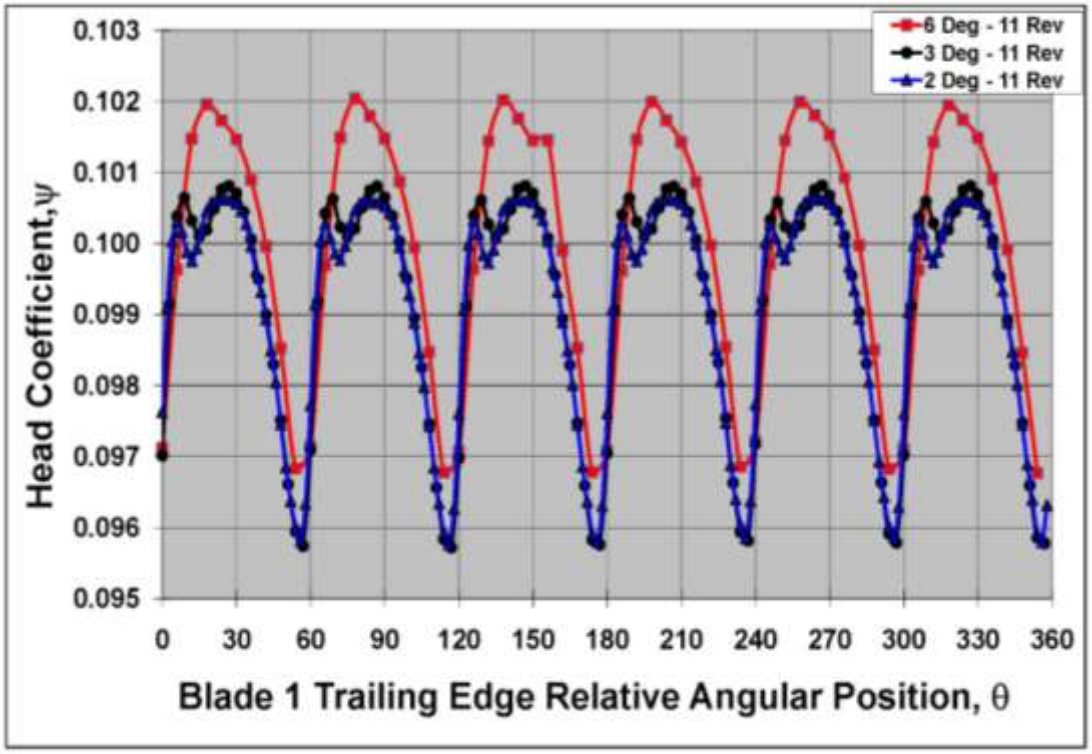

Figure 4-6 Head coefficient and relative angular position of impeller Blade 1 trailing edge from the volute tongue.

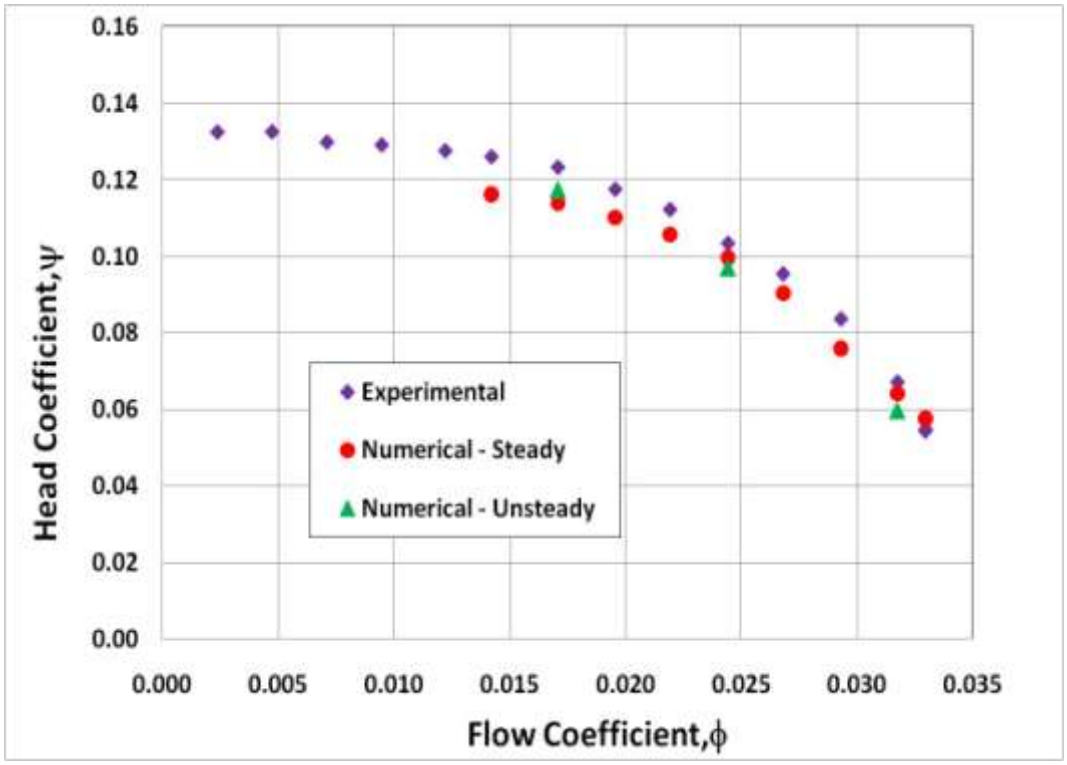

Figure 4-7 Curved intake pump head flow characteristic curve.

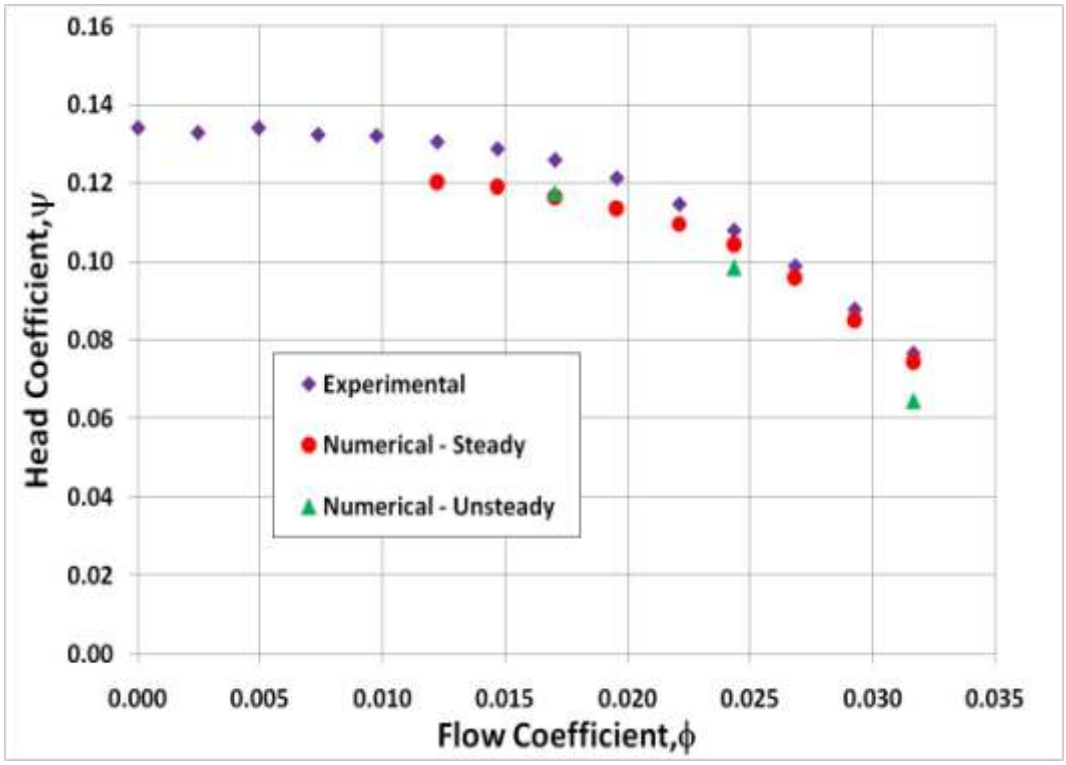

Figure 4-8 Straight intake pump head flow characteristic curve.

CHAPTER 5 SECONDARY FLOW IN CENTRIFUGAL PUMP[1]

In Chapter 4, the overall pump performances obtained by using steady and unsteady computations were discussed. The numerically predicted pump performances are in good agreement with the experimental curves. With this, the detail flow field analysis within the centrifugal pump will be studied.

5.1 Flow Field at Intake Section

5.1.1 Curved intake section

Figure 5-1 shows the cross-section view of the intake section. The intake section is designed in such a way that it has a non-circular but constant cross-sectional area to ensure the fluid velocity is constant. The inlet section connecting to upstream pipe is circular and progressively change to a corner-rounded rectangle section at mid-span and becomes circular again just before the impeller eye. A straight partition vane is located at the middle intake section before the impeller eye and is shown as dotted line in Figure 5-1. The distance from the centre of the impeller to the intake section just before extension L is 500 mm. The intake extension is two times of intake diameter. The dimensionless distances of plane P1 to P3, x/L, to the centre of the impeller are 0.24, 0.38 and 0.5 respectively. After plane P3, the planes P4 to P8 are advancing in angular direction with an increment 18 ° with reference to the centre of the curvature. The curved intake section has a Dean number of 8.52×10^5, with a Reynolds number of 1.04×10^5 at best efficiency point flow rate. The Dean number is defined as:

[1] Part of this work has been published in:
K.W.Cheah, T.S. Lee and S.H. Winoto, 2010, "Numerical Study of Inlet and Impeller Flow Structures in Centrifugal Pump at Design and Off-design Points", International Journal of Fluid Machinery and Systems, Vol. 4, No.1, pp. 25-32

$$De = \mathrm{Re}\left(\frac{D}{2R}\right)^{1/2} \tag{5.1}$$

where Re is the Reynolds number, D and R are the diameter and radius of curvature of the curved pipe.

At the intake section, the secondary flow is developed upstream and has great influence to the flow entering impeller eye. It is well known and documented in the literature that curved pipe flow will cause secondary flow along and after the curve due to centrifugal force. A detailed review of the flow in curved pipe is given by Berger and Talbot (1983). As fluid flows through a straight pipe or duct and into a bend, the pressure which in the straight section is uniform across the flow, must adjust in the bend to counter centrifugal force. The centrifugal pressure gradient is greatest at the outer wall and least at the inner wall. This can be related to free vortex flow theory in a curved pipe where the pressure increases radially outward from the centre of curvature while the velocity decreases, as described by:

$$\frac{dp}{dR} = \rho\frac{V^2}{R} \tag{5.2}$$

where p is the pressure, R the radius of curvature and V velocity along the curved path. Flow separation often occurs at the inner wall and spiralling cross flow motion appears in the centre of the pipe towards the outer wall.

Starting from plane P1, the flow is very steady, not yet influenced by the bend but the flow at top wall region becomes unstable and starts separating. This can be seen clearly on plane P1 in Figure 5-2 and Figure 5-3. The fluid is slightly accelerated near the inner wall in accordance with the favourable radial pressure gradient from inner wall to outer wall as shown in plane P1 in Figure 5-4.

At plane P2, the fluid near the outer wall is decelerated due to change of pressure gradient. The curvature effect starts to influence the main flow to cause a secondary flow forming on the top wall region.

Further downstream at plane P3, the secondary flow due to the centrifugal force appears in the cross over and grows up rapidly, forming two counter rotating vortices that circulate inward in the top central part of the curved pipe. It is also observed that outside the core of the counter rotating vortex, streamline from inner core decelerating and dividing to upper wall diagonally. This is due to the pressure at this plane P3 increases near the outer wall in radial direction and the fluid near the outer wall starts to decelerate.

The curved intake section, starting from the intake inlet to plane P3, can be considered as S-shaped duct. For this kind of duct, the secondary flow developed would be a pair of inward counter-rotating vortices as shown by Whitelaw and Yu (1993).

At plane P4, where the partition vane starts dividing the main flow, the fluid near the inner bend is accelerated by the secondary flow. The results show the development of strong pressure-driven secondary flows in the form of a pair of counter-rotating vortices in the stream wise direction. Asymmetrical flow is observed near the lower part of the partition vane. This is because the flow at impeller eye is started interacting with flow main flow entering it. The slower fluid near the outer wall continues in circular motion towards the top wall. It is observed that another secondary counter rotating vortex flow on the side walls. The formation of the side wall vortex is originated from the plane P3, where spiralling flow is started.

Further downstream at plane P5 to P7, the two pair of counter rotating vortices are being suppressed by the momentum of fast moving fluid. The core of the main vortex is shifted to the closer centre of the bend while the secondary vortex core is pushed to the side walls. However, these secondary vortex flows within a circular cross section are not reported by the measurements of water flows such as those obtained using laser doppler velocimetry by Enayet et al. (1982) and Azzola et al. (1986).

As noticed in plane P8, the asymmetrical vortical flow structure will propagate further downstream into impeller eye. This results in greatly distorted velocity contours. Figure 5-4 also shows the highly distorted pressure contour due to this impeller and secondary flow structures interaction. Because of this secondary flow, shock loss increases and reduces the pump head generated for curved intake section pump.

Figure 5-5 shows streamline across different location at different flow rates. At off-design point, with $0.7Q_{design}$ and $1.3Q_{design}$, no significant flow structure difference from the Q_{design}. This is because of the straight partition vane placed in the curved intake section which dividing the counter rotating vortex into half. However, just before the impeller eye at plane P8, the streamline at $0.7Q_{design}$ is asymmetric as compared to Q_{design} and $1.3Q_{design}$. The vortex core on the left side of the intake section is suppressed on the centre while the vortex core on the right side of the intake section is stretched and smeared. This is an evidence to show the inflow at intake section interact with the flow in impeller eye.

5.1.2 Straight intake section

For straight intake section pump, the flow is very uniform across the intake section from the inlet up to the swirl breaker or a straight partition vane just before the impeller eye. This is because the numerical simulation is using a fully developed flow profile. However, there is still a strong interaction of the flow structure just before the impeller eye due to the pre-swirl or pre-rotation flow development.

From the Euler entrance velocity triangle, as the flow rate varies, the flow angle will change accordingly. At design flow rate, assuming shockless entry, meridional flow angle α_1 will be 90 ° and perpendicular to the U_1. For $Q < Q_{design}$, α_1 will be less than 90 °. When the main flow entering the impeller eye, swirling flow or pre-rotation flow will developed in the direction of impeller rotation. However, for $Q > Q_{design}$, α_1 will be more than 90 ° and the swirling flow developed should be in opposite direction.

In order to visualize how the pre-rotation or pre-swirl flow developed upstream before impeller eye for the straight intake section pump, Figure 5-6 shows how the velocity and pressure contours change according to flow rate.

At $0.7Q_{design}$, it is observed that the pre-swirl flow is developed near the right top corner of the intake section but blocked by the swirl breaker as shown in Figure 5-6 (a). A small pre-swirling flow zone is also observed at the lower right corner. But a low flow zone is formed behind the vane and this represents a small flow blockage due to possible a flow reversal from impeller eye. Figure 5-6 (d) shows the pressure contour at $0.7Q_{design}$ with high pressure zone concentrated at the low flow region.

When the pump is running at best efficiency point, a more uniform flow velocity and pressure contour observed in Figure 5-6 (b) and (e). This is already explained that

at design flow rate the flow has zero incidence flow angle and tangent to the blade leading edge.

On contrary to lower flow rate, at higher flow rate $1.3Q_{design}$, the pre-swirling flow is developed at the left top corner of the intake. However, the flow behind the vane is not totally stalled as what has seen in the low flow rate case. In fact, there is a continuous flow velocity contour. This suggested that at higher flow rate, the pre-swirling flow has higher momentum the interaction with the impeller eye is stronger.

As previously discussed, it can be concluded that the inlet flow distortion developed upstream of the impeller eye can cause additional losses and circumferentially distorted flow patterns in the impeller passage. This distorted flow or pre-rotation flow is flow rate dependent. This can results in increased losses, unsteady blade loading and increased NPSH.

5.2 Flow Field inside Centrifugal Impeller

In the previous sections, the emphasis is on how flow field developed within the intake sections before entering the impeller. It can be seen that there is already a strong interaction between the flow in the intake sections and near impeller eye. In this section, more focus will be on the instantaneous secondary flow field developed within the pump impeller.

5.2.1 Velocity vector at front shroud leading edge

Figure 5-7 shows the cascading view of the flow within the impeller passage near impeller front shroud at three different flow rates. When main flow is being diverted into the blade-to-blade passage, the leading edge flow separation pattern is flow rate

dependent. In most cases, inflow incident angle is non-tangent to the blade leading edge.

Figure 5-7 (a) shows the suction side of the blade forming a secondary flow or vortex flow at the mid-section of blade-to-blade passage at $0.7Q_{design}$. This phenomenon also known as stalled flow where the slowing moving fluid is blocking the main flow through the main passage. The main flow is being diverted by the core of the vortex flow. Reversed flow is observed near the suction side of the leading edge as well. The core of counter clock wise vortex flow is also affecting the flow at adjacent passage as well by inducing a pressure side leading edge separation. The main flow in the passage becomes smooth again after passing the stalled flow.

Due to the unsteady effect developed at upstream of the curved intake section, the flow entering the passage is no longer tangential to the leading edge of impeller blade. The shockless velocity entry to impeller passage cannot be achieved even though at the best efficiency point. At Q_{design}, Figure 5-7 (b), the leading edge flow separation occurred on the suction side leading edge. The slowing moving fluid appears at the main passage is stretching over the "throat" or overlap region of the leading edge. On the adjacent blade pressure side leading edge, the main flow is partially blocked by the suction side leading edge separation. Even the main flow carries certain momentum but it is unable to overcome the reversed flow caused by suction side leading edge separation.

However, at $1.3Q_{design}$, there is no obvious flow separation on the leading edge on either pressure or suction sides. The main flow entering the blade passage appears to be smooth and congruent to the blade profile very well.

5.2.2 Velocity vector at mid-plane of impeller

Figure 5-8 shows the velocity vector at mid-span of the impeller passage, z/b = 0.5 at different flow rate. Figure 5-8 (a) shows that when the centrifugal pump is running with $0.7Q_{design}$, a strong recirculation flow develops on the blade suction towards downstream of the passage. Compared to the front shroud velocity vector in Figure 5-7 (a), which only shows the recirculation flow near suction side leading edge due to stalled flow, the mid span velocity vector plot clearly showed the wake flow zone on the suction side of the impeller extending downstream after the leading edge. Further downstream, slow moving fluid is attached to the suction side before leaving the impeller exit into the volute casing. This phenomenon could be considered as jet-wake structure development phase as reported by many researchers. The jet-wake structure is found to be caused by leading edge flow separation on suction side.

At Q_{design} and $1.3Q_{design}$,, the leading edge flow separation is still there. The flow separation could stretch up to 15% of the blade cord length downstream. The recirculation flow behind the leading edge is experiencing a shearing effect exerted by the main flow in impeller passage. This leading edge separation could lead to energy loss in the pump and could further influence the flow field in impeller passage in stream wise direction. Overall, the velocity vector inside impeller passage can be considered smooth and follows the blade curvature profile from impeller passage entrance till the exit without any separation on blade pressure side. This is matching the potential flow theory for flow pass turbomachinery blade.

5.2.3 Surface streamlines on impeller blades

To further investigate the flow pattern within the impeller passage, Figure 5-9, Figure 5-10 and Figure 5-11 show the surface streamlines on pressure and suction

sides of the impeller blades. As demonstrated by Murakami et al (1980) and Hamkins and Bross (2002), their experimental investigation showed that surface oil flow patterns can be analyzed to directly obtain quantitative information about a flow field because of good agreement between numerically computed surface streamline and experimental flow visualization results.

Figure 5-9 shows the surface streamlines at $0.7Q_{design}$. On the pressure side from Blade 1 to 6, the streamlines are not parallel to the blades shroud and hub sides. Near the shroud leading edge, where the flow just turned radially from axial direction, the surface streamlines on the blade pressure side are negatively inclined, before flowing in parallel to the hub and shroud downstream near trailing edge. This can be explained that when the main flow is entering the blade-to-blade passage, the axial momentum of the fluid carried upstream of impeller is dominating near the leading edge. Once the flow passed the leading edge, the centrifugal and coriolis forces start to influence the fluid flow. When the main flow turned completely from axial to radial direction, the main flow is deflected from hub to shroud surface approaching the trailing edge in nearly parallel form.

However, on the suction side of Blade 1 to 6, the flow pattern is highly irregular. There is a distinct line dividing the streamline from the shroud and hub sides due to the reversed streamlines from hub and shroud surfaces. This suggested that three-dimensional flow recirculation is occurring within the blade-to-blade passage. Based on the surface streamline direction, it can be explained as follow. The streamlines that reversed from the front shroud surface after the leading is due to the stalled flow as shown in Figure 5-7. As mentioned previously, the stalled is blocking the main flow in the passage but at the same time reversing the flow on the suction side leading edge.

From Figure 5-8, the mid plan velocity vector shows a leading edge separation on the suction side as well. Hence the flow is reversed to the leading edge as well from the hub surface. Because the leading edge flow separation occurred near the front shroud and hub, the reversed flow actually is wrapping over the suction side leading edge. Further downstream of the impeller passage, the flow from the shroud and hub surfaces merged before leaving the impeller passage. Based on the merging pattern of the surface streamlines, it is suggested that there could be a surface vortex and detached flow from shroud side towards hub side.

When the flow rate increases to Q_{design} and $1.3Q_{design}$, Figure 5-10 and Figure 5-11 show a similar flow pattern observed on the pressure side of the blades at $0.7Q_{design}$. The main flow after leading edge is deflected from the hub surface and approaching the impeller exit being parallel to the hub and shroud surfaces. The streamlines are pressure driven and remain attached to the impeller blade because of the pressure increases in radial direction. When flow approaching the impeller exit, the flow velocity is increases as well due to energy gained from the rotating impeller.

On the suction side, a low velocity zone is observed near hub leading edge and the reversed streamlines flowing from hub to shroud leading edge. As compared 0.7 Q_{design}, there is no reversed flow from the shroud side. In Figure 5-8 (b) and (c), it shows that the leading edge is stretching more than 15% from the leading but there is no flow separation on shroud. This suggested that the leading edge flow separation is pointing from hub to the shroud leading edge corner. As compared to the pressure side, suction side always have lower pressure and the flow detached from the vanes surfaces that caused the surface streamlines irregularity.

Another observation on the blades suction sides is that there is no surface streamlines wrapping and merging at Q_{design} and $1.3Q_{design}$. In fact, the surface streamlines originated from the hub leading edge flow towards impeller exit at a positive flow angle. This suggested than the streamline is dominated by axial flow components.

5.2.4 Secondary flow formation inside the impeller passage

Figure 5-12 shows the instantaneous flow pattern within the impeller passage at different flow rates. The velocity contour used is a non-dimensional contour of C_m/U_2. These cross-sectional view of the impeller passage are located within the impeller passage at r/r2 at 0.955, 0.899, 0.843, 0.786, 0.730, 0.674, 0.618 and 0.562 respectively. The cross-sectional plane is labelled as S1 near impeller leading edge to S8 near impeller exit. The secondary flow structures within the impeller passage are flow rate and as well we streamwise dependent.

At $0.7Q_{design}$, the suction shroud corner has a wake flow zone. This is a leading edge separation as discussed Section 5.2.1 and shown in Figure 5-7 (a). As the flow moving downstream in streamwise direction of the passage, a high velocity core emerges on the pressure side of the blade from plane S1 to S4. At the same time, the wake flow zone on the suction side is diffused and diminishing. The mixing process of the high velocity jet flow and low velocity wake flow is due to the strong coriolis and centrifugal forces present in the impeller passage. Further downstream of the impeller passage, the jet and wake flow is blended due to the strong mixing process. Based on the velocity contour, it can be said that the jet wake flow is carried downstream because of vortex flow within the impeller passage. When the flow approaches the impeller exit at plane S7 and S8, there is the low velocity wake flow

zone shifted to the hub side and blocking a significant portion of the passage. A high velocity zone emerges on the shroud pressure corner to fill up the momentum deficit created by the hub wake flow.

At Q_{design}, the flow pattern is very different from $0.7Q_{design}$. When flow is just entering the impeller passage at plane S1, the high velocity flow near pressure shroud corner is dominant. As the flow moves downstream from plane S1 to S5, the high velocity core is spanning from shroud pressure corner to hub suction corner diagonally. This suggested that there is a strong vortex formation within the passage. At plane S6, as the high velocity flow moved to the suction hub corner, a low velocity wake flow is emerging to fill up the low flow region. The low velocity wake flow core continues to evolve until the flow reach the impeller exit with a wake flow zone appears at the centre of impeller exit.

At $1.3Q_{design}$, no wake flow zone appears at plane S1 near passage inlet. The high velocity flow is concentrating on the pressure shroud corner as well as suction shroud corner. The secondary flow structures formation is similar to Q_{design} in streamwise direction. At plane S3 and S4, the high velocity flow cores are at the shroud and hub sides. As the flow move further downstream as in plane S6 to S8, the high velocity core move to the suction hub corner and leave a low flow zone behind it. The low flow zone is spanning diagonally across the impeller exit.

5.3 Secondary Flow Developed inside Volute Casing[2]

5.3.1 Vortex flow inside volute casing

There are two approaches to determine the volute casing design, constant angular momentum and constant velocity. For constant angular momentum design method, the tangential component of velocity (in absolute frame) multiplied by the radius of the any cross-section across the volute casing. For constant velocity approach, the mean velocity is assumed constant across all cross sectional of volute starting from cut water. The cross-section of the volute could be rectangular, circular or trapezoidal according to the pump specific number. In this case, the volute casing is trapezoidal shape designed according to the constant angular momentum approach.

Figure 5-13 shows the flow discharged into the volute casing at $0.7Q_{design}$. At Plane I, a strong counter rotating vortex flow developed near volute tongue and evolving into asymmetrical vortex flow in angular direction downstream. The flow discharged from the impeller exit is jet flow like with a high velocity core flow near shroud and retarded flow near hub. A small recirculation flow near impeller hub exit side is observed. This high momentum core jet and flow shearing between the core and sides flow further enhanced the formation of the counter-rotating vortex formation and development. The confined volute flow passage profile at plane I to III and distorted velocity profile at impeller outlet as seen in Figure 5-8 (a) also attributed to this counter-rotating vortex formation.

As the flow advances in the angular direction according to the cross-sectional plane with θ = 45 °, 90 °, 135 °, 180 °, 225 °, 270 °, 315 ° and finally at the exit plane, the

[2] Parts of this work has been published in:
K.W. Cheah, T.S. Lee and S.H. Winoto ,2011, "Unsteady Analysis of Impeller-Volute Interaction in Centrifugal Pump", International Journal of Fluid Machinery and Systems, Vol. 4, No. 3, pp. 349-359

symmetrical counter rotating vortex flow continues to develop into an asymmetrical vortex flow. The asymmetrical vortex flow developed downstream is due to high velocity jet discharged from impeller exit near front shroud inclined at a positive angle, reached the curved volute wall, reversed and formed a wrapping layer around the main flow.

Another observation is the average velocity within the cross-sectional plane of the volute casing is low because of lower flow rate. This is expected because lower flow rate will have lower angular momentum. The deceleration of the flow within the volute casing will result in a static pressure rise or energy recovery. However, the vortex flow will create diffusion and eddy losses.

Figure 5-14 shows vortex flow inside the volute casing at Q_{design},. At Plane I to III, the counter-rotating vortex is formed and symmetrical. However, starting from Plane IV the jet flow core no longer at the centre of the impeller exit and shifted to the shroud side. Because of this, the symmetrical counter rotating vortex flow is distorted with larger vortex core at lower corner of the volute casing. As the flow advances in the angular direction towards the volute exit, the spiralling counter rotating vortex flow continues to evolve. The larger vortex at lower corner gained higher momentum by suppressing top corner vortex and forcing smaller vortex to disappear downstream.

As compared to $0.7Q_{design}$, the average velocity within the cross-sectional plane is higher at Q_{design}. As explained earlier, higher flow rate which means higher angular momentum as well. This in turn will increase the static pressure rise around the volute casing.

At $1.3Q_{design}$ the jet flow discharged from the impeller exit does not formed a counter-rotating vortex at the top and lower corner of the volute casing near volute

tongue as seen previously. This is because the flow leaving the impeller a larger radial and smaller tangential velocity in absolute frame. The high angular momentum flow from impeller exit suppressed the formation of the vortex at Plane I and II as shown in Figure 5-15. In addition, the flow from the volute exit region re-enter the volute tongue also disrupting the vortex flow at this narrow gap. Only after Plane III, the asymmetrical counter-rotating vortex can be seen on the top and lower corner of the casing but not as strong as those seen in $0.7Q_{design}$ and Q_{design}. However, the asymmetrical counter rotating vortex is losing momentum at Plane VI. When the flow reached Plane VII and VIII, the vortex flow developed into a single core near impeller exit. This is because the fluid in the volute casing is having higher momentum and pushing the flow back to the impeller.

For $1.3Q_{design}$, a larger radial flow velocity than the tangent velocity in absolute frame within the volute section is observed. As opposite to $0.7Q_{design}$ and Q_{design} the volute will cause acceleration of the fluid and results in a static pressure decrease along the volute. The dissipation of the high swirl energy, resulting from the large radial velocity component, is the major source of losses at large mass flow.

The numerical result is in good agreement with Elhom et al (1992) LDV measurement inside a logarithmic volute. Their results show that impeller exit radial velocity transformed into a swirling flow with a forced vortex type velocity distribution at centre and a nearly constant swirl velocity away from it. They summarized that the circumferential curvature of the volute is responsible for a radial gradient of the through flow velocity and strength of the cross-sectional swirling flow.

The single and double vortical flow structures inside the volute casing also have been reported by many researchers. Investigation done by Nursen and Ayder (2003)

on an external type volute with a rectangular cross-sectional shape that having a constant axial width and also investigation by Majidi and Siekmann (2000) with single volute casing that is designed according to the theory of a constant average velocity for all sections of the volute showed the development of vortical flow structures within the volute casing.

It can be concluded that the spiralling vortex flow formed inside the volute is sensitive to the volute geometry and flow rate dependent. The relative gap between the shroud and volute casing, hub and volute casing will have influence on the vortex flow formation as well in stream wise direction. This is because there will be always a back flow (leakage) from the gaps between hub, shroud and volute casing.

5.3.2 Wake flow at volute casing exit

Figure 5-16 shows the absolute frame velocity vector at the mid impeller span, z/b=0.5 near volute tongue with different flow rates. At $0.7Q_{deisgn}$, the flow discharged from the impeller make a positive incidence angle when approaching volute tongue. The flow passes through the gap of volute tongue and impeller trailing edge and re-enter into volute casing. As seen in Figure 5-13, the flow discharge from the impeller exit is distorted partially due to this flow re-entering. On the suction side of the volute tongue, a small flow recirculation region is observed due to this flow re-entering. The flow recirculation is because the flow re-enter the gap with high velocity as seen in Figure 5-16 (a), and the gap expands in circumferential direction to induce the flow reversal on suction side of tongue. The flow re-entering into volute casing will cause additional losses.

At Q_{design}, a near zero incidence flow angle at volute tongue is observed. The flow approached the volute tongue tangentially and no flow recirculation observed near

either suction or pressure sides. As compared to $0.7Q_{design}$, the flow discharged from impeller is made a flow incidence angle zero to the volute tongue. In this case, it means, the β_2 is same as the volute tongue. Based on this observation, it is suggested that this flow rate is may be optimum for this particular volute casing tongue angle design.

At $1.3Q_{design}$ a significant backflow is re-entering passage 6 through volute tongue because of the negative incidence flow angle. When the flow is leaving the impeller, the meridional flow angle β_2 is severely distorted as compared to β_2 at Q_{design}. The flow on the pressure side of the impeller blade is having a larger β_2. According Euler velocity triangle at impeller exit, the C_{m2} is proportional to volume flow rate. Due to this distorted outlet flow angle, the flow is blocked and stalled on the suction side of volute tongue as shown in Figure 5-16 (c). As compared to $0.7Q_{design}$, there is no flow reversal and all stalled flow is following the expanding direction of the volute casing wall. However, a wake flow region is observed on the pressure side of the volute tongue due to the blocked flow.

Figure 5-17 shows the velocity vector at mid plane of the volute casing near impeller exit. This is an extension from Figure 5-16 to capture the overall flow phenomenon at the volute exit. At $0.7Q_{design}$ and Q_{design}, the flow follows the curvature of the outer wall of casing very well. But on the inner wall, the flow is spiralling and forms a wrapping layer on the main flow at the centre of the volute casing. At higher flow rate, $1.3Q_{design}$, there is a distinct flow region, jet and wake flow behind the volute tongue. Near the inner wall behind volute tongue, because of the negative flow angle, there is a large wake flow zone. On the outer wall, there is a high velocity zone. Due to the mismatch of velocity, of these flow zones, a high shearing flow is expected.

This kind of flow pattern can be characterised as jet wake flow that is similar to jet wake flow inside the impeller passage.

5.3.3 Vortex tube inside the volute casing

To further visualize the vortex flow formation from impeller exit near volute tongue and evolution of secondary flow up to volute exit, Figure 5-18 shows the three -dimensional streamlines inside the volute casing at different flow rates. Starting from the volute tongue, the fluid discharges from impeller into volute casing at smallest volute radius. Circumferentially further downstream, flow discharges from impeller into volute casing at increasing volute radius, starts wrapping around the upstream fluid. Regardless of flow rate, the streamlines flowing out circumferentially from impeller exit will form a wrapping vortex tube starting from volute tongue to volute throat. This wrapping of streamlines is an evidence of the vortex flow as discussed in Section 5.3.1.

After the volute throat, the streamlines direction behind the volute tongue and near volute exit is flow rate dependent. As mentioned earlier, the flow behind volute tongue at $0.7Q_{design}$ and Q_{design} formed a wrapping velocity vector pattern. This is clearly seen in Figure 5-18 (a) and (b), where the streamline crossing over and forming the vortex flow again. The streamlines on the outer wall is smooth and follow the curvature of the outer wall. However, at $1.3Q_{design}$, the streamlines behind volute tongue is not crossing over but instead formed as reversed flow streamlines. This flow reversal is same as in Figure 5-17 (c). The streamlines are only crossing over in the straight section of the volute exit.

5.4 Pressure Distribution in the Centrifugal Pump

Due to the spiralling geometry of the volute casing and position of the tongue, the flow discharged from the impeller is unmatched. Because of this, it is expected that the radial force will be unbalanced at various operating conditions. Stepanoff (1967) showed that the pressure distribution around the volute casing is flow rate dependent. This is further confirmed by the measurement done by Iversen et al (1960) about static pressure difference across volute wall in circumferential direction.

Figure 5-19 shows the pressure distribution within the impeller and volute casing at various flow rates. The pressure increases gradually along stream-wise direction within impeller blade-to-blade passage and has higher pressure on pressure surface than suction surface for each passage. The pressure contour isobar lines are not all perpendicular to the pressure side of the blade inside the impeller passage especially near the leading edge due to the flow separation as mentioned above. The static pressure on the casing also indicated that there is a pressure change from lower flow rate to higher flow rate. At $0.7Q_{design}$, more positive pressure is observed near the volute outlet and a uniform pressure around the volute casing at Q_{design}. At $1.3Q_{design}$, higher pressure around the volute casing rather than the volute outlet. From the pressure contour plot, it can be seen how the pressure distribution changing according to flow rate and this will in turn affect the blade loading and radial thrust on the impeller.

Figure 5-20 shows the pressure coefficient distribution around the volute casing. It can be seen that at Q_{design}, the pressure rise from volute tongue towards the casing exit is smooth and pressure distribution around the casing is uniformly distributed as

compared to other flow rates. The pressure distribution around the volute casing at Q_{design} is illustrated in Figure 5-19 (b).

However, at $0.7Q_{design}$, the pressure rises from volute tongue towards casing exit is very steep and large uneven radial force is expected. The uneven pressure distribution around the volute casing is illustrated in Figure 5-19 (c). This is because the volume flow rate discharged from the impeller circumferential is lower than the volume flow rate required to fills up the volute casing. The volute casing is design based on the constant angular momentum. If the flow rate is low, volute casing will act as diffuser where the larger pressure will be recovered near volute throat and cause uneven pressure distribution.

As compared to high flow rate, $1.3Q_{design}$, the pressure rise reaching to the maximum when it is half of angular distance from the volute tongue towards casing exit. This suggested that the radial force at higher flow rate is more towards to the vertical direction rather than horizontal direction for the lower rate.

5.5 Pressure Loading on Impeller Blades

The pressure loading on the impeller blades at different flow rates are plotted in Figure 5-21. The pressure coefficient Cp on the pressure and suction sides are plotted against the normalized radial direction with r/r_2.

At lower flow rate $0.7Q_{design}$, there is a considerable pressure difference between the pressure and suction side. The smallest pressure coefficient difference is about 0.11 at $r/r_2=0.6$ and largest difference of 0.41 at $r/r_2=0.80$. The pressure load almost increases linearly along the streamwise direction on pressure side of impeller blade. The increase of the pressure on the pressure side can be explained that the flow

streamline is in curvilinear form described as in Eq (5.2). The flow on the pressure side of the blade is considered as pressure driven flow as shown in surface streamlines plot in Figure 5-9. The pressure coefficients on blade 3 and 4 are different because of the jet wake flow pattern inside the passage flow as explained in Section 5.2.2 and illustrated in Figure 5-8. However, on the suction side, due to flow separation and recirculation, the pressure coefficient near the leading edge decreases before increases further downstream.

Another observation is on the blade leading and trailing edge pressure difference. Figure 5-21 (a) shows that the pressure coefficient on the leading edge always has a saddle region, decrease from the first point before increase again after about 10% chord length downstream. However, on the suction side of the leading edge, the pressure coefficient increases slowly to the trailing edge without any pressure drop. At the trailing edge, the pressure coefficient on the pressure and suction sides are overlapping each other. This is because after the blade trailing edge overlap region, or so called the "throat", the flow on the pressure side is no longer being "impel" by the impeller. Hence there will be sudden pressure drop at the trailing on the pressure side.

However, the pressure difference at Q_{design} on the pressure and suction sides are more uniform. Again, near the leading edge, there is a saddle region on pressure side. On the suction side, the pressure coefficient is affected by the recirculation at 25% downstream from the leading edge. The pressure difference on the pressure suction sides also smaller as compared to $0.7Q_{design}$. The smallest pressure coefficient difference is about 0.06 at r/r_2=0.60 and largest difference of 0.33 at r/r_2=0.80.This again proved that at Q_{design}, the pressure is uniformly distributed around the casing and on the blades as well.

At 1.3Q_{design}, the pressure coefficient on the pressure and suction sides start to converge from the leading edge and coincide each other at r/r_2=0.55. Then after the pressure coefficient starts to diverge before overlapping at the blade trailing edge. The largest pressure coefficient difference is about 0.75 at r/r_2=0.80. From the suction side pressure loading on the blades, it can be concluded that there is a flow separation after leading edge where the static pressure is reduced up to a certain point. As the fluid flow downstream, there is a reattachment of the flow on the blade profile and this increase the wall pressure again. However, just after the overlap region at the trailing edge, it can be seen that the pressure different is reducing again because the flow on the suction and pressure sides trying to merge together.

The blade loading trend agree well with those measured by Kosyna et al (2001), Rose (2004) and Kikuyama et al (1992) even with different profiles. This is because the blade loading is much depends on the curvature of the blade and thickness and also flow rate dependent.

5.6 Concluding Remarks

The secondary flow structures from the intake section to the volute exit have been analyzed and a few conclusions can be drawn.

The inlet secondary structures are flow rate dependent. For straight intake section pump, for $Q < Q_{design}$, the pre-rotation flow at inlet follows the impeller rotation direction. For $Q > Q_{design}$, the pre-rotation flow opposes the direction of impeller rotation. However, for curved intake section, the secondary flow structures are affected by the geometry of intake section rather than the flow rate due to proximity of guide vane and impeller eye.

The velocity vector near impeller shroud is strongly coupled with the flow rate. At low flow rate, a stalled flow is observed near impeller shroud leading edge blocking the main flow. As the flow rate increases, the leading edge separation and recirculation is improving due to better flow incidence angle. At $1.3Q_{design}$, flow enters the impeller passage smoothly without any leading edge separation.

The characteristic of the jet/wake flow structure is recognized with a present of low meridional velocity flow core on the shroud/suction corner. The jet wake flow pattern also is flow rate dependent. A cross-sectional view of the impeller passage from leading edge to impeller exit shows that jet wake flow formation is affected by upstream velocity pattern. As the wake flow convected downstream, the wake flow cores location is moving from shroud to hub side and diffused.

With the analysis on the surface streamlines, it can be concluded that the surface streamlines patterns on pressure and suction sides are flow rate dependent and affected by upstream flow condition near front shroud as well. The streamlines on the pressure side are pressure driven and remained almost parallel to shroud and hub surface after turning axially to radial direction. However, on suction side of the blade, irregular surface streamlines indicate that the strong flow separation on the blade leading and vortex formation on blade surface in streamwise direction.

A strong vortex flow developed inside volute casing when flow is discharged from impeller circumferentially into casing. This circumferential flow forms a wrapping vortex stream tube starts from volute tongue and advances angularly downstream to volute throat and exit. The secondary and wake flow at the back of volute tongue is flow rate dependent. At $0.7Q_{design}$ and Q_{design}, the wake flow is just behave like a wrapping vortex flow due to the flow incidence angle on the volute

tongue. However, at $1.3Q_{design}$, due to higher angular momentum of the vortex flow and large positive flow incidence angle, a jet wake flow is formed behind the volute tongue.

Based on the static pressure distribution around the volute casing, it can be concluded that the radial forces on the pump is uniform and minimum at Q_{design}. At $0.7Q_{design}$ and $1.3Q_{design}$, the uneven pressure distribution will generate unbalance forces on the pump itself. On the pressure and suction sides of the impeller blades, the pressure coefficients increase in streamwise direction regardless of flow rate. But there is a saddle region due to leading edge flow separation. At $1.3Q_{desgin}$, the pressure and suction side pressures converged to same value near leading edge before diverging downstream.

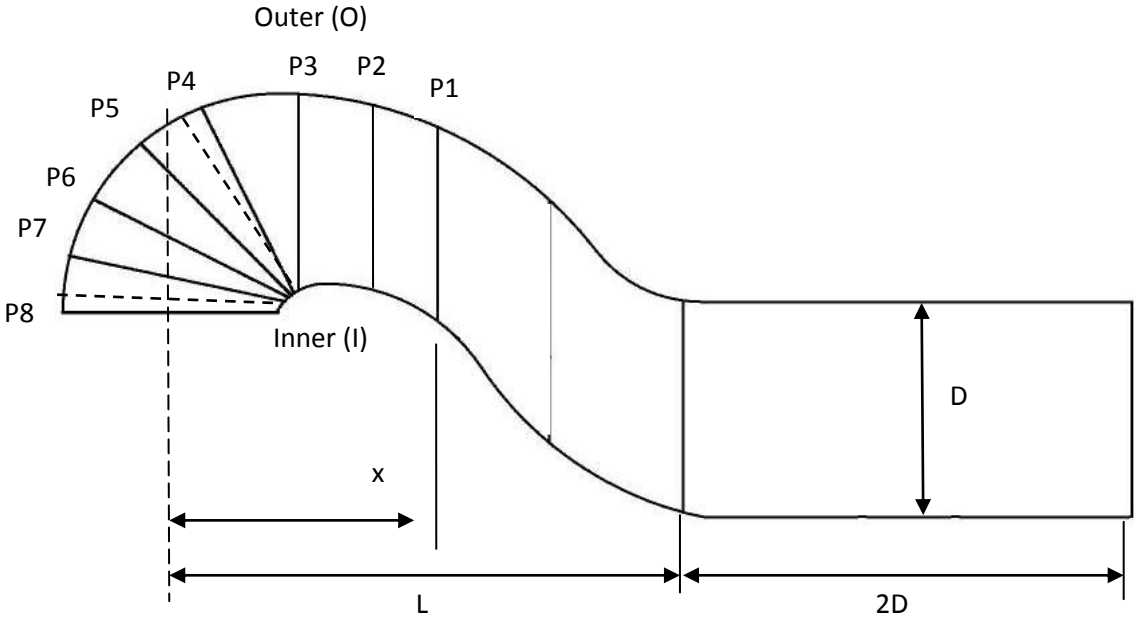

Figure 5-1 Cross-sectional view of curved intake section.

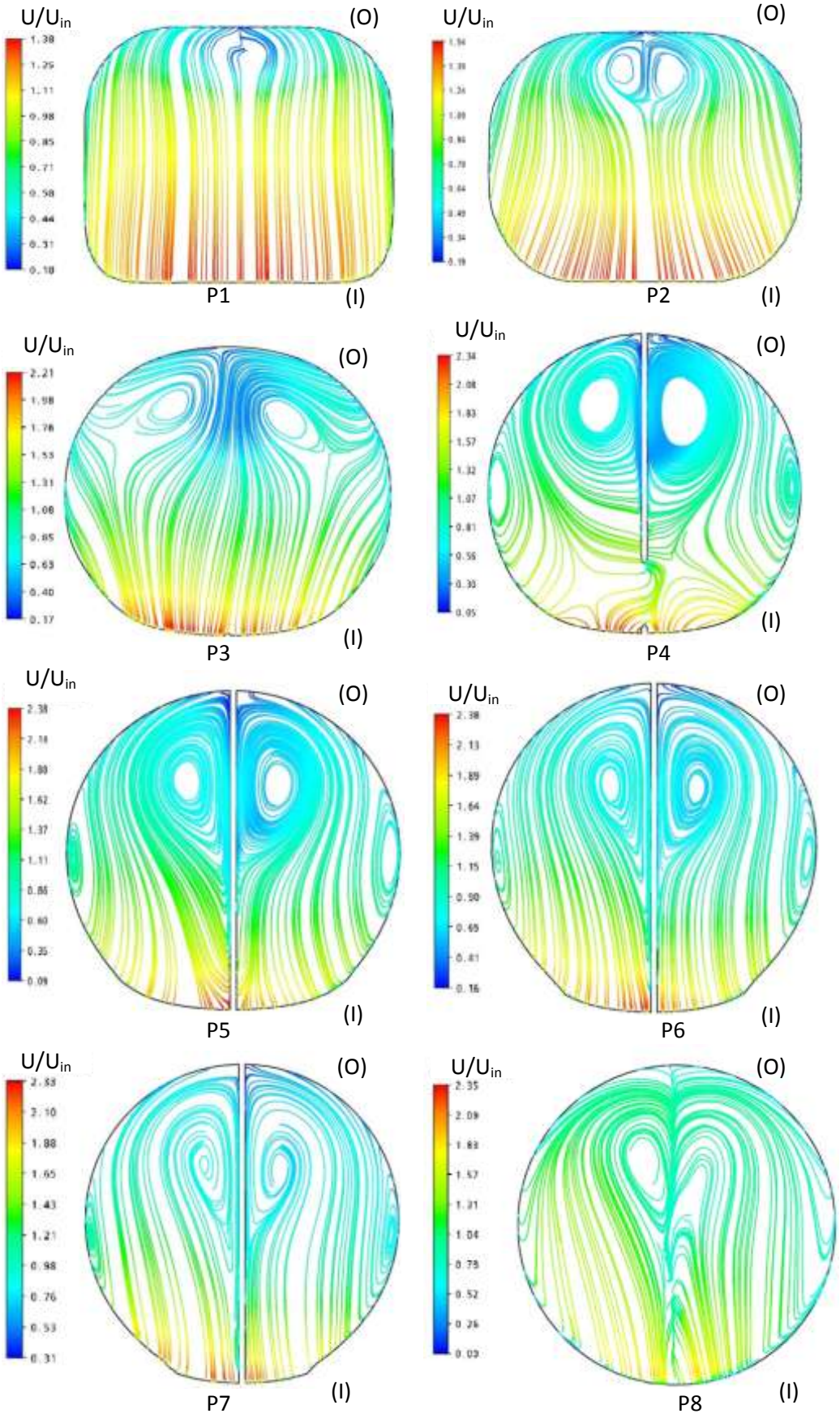

Figure 5-2 2D Streamline across the intake section at Q_{design} .

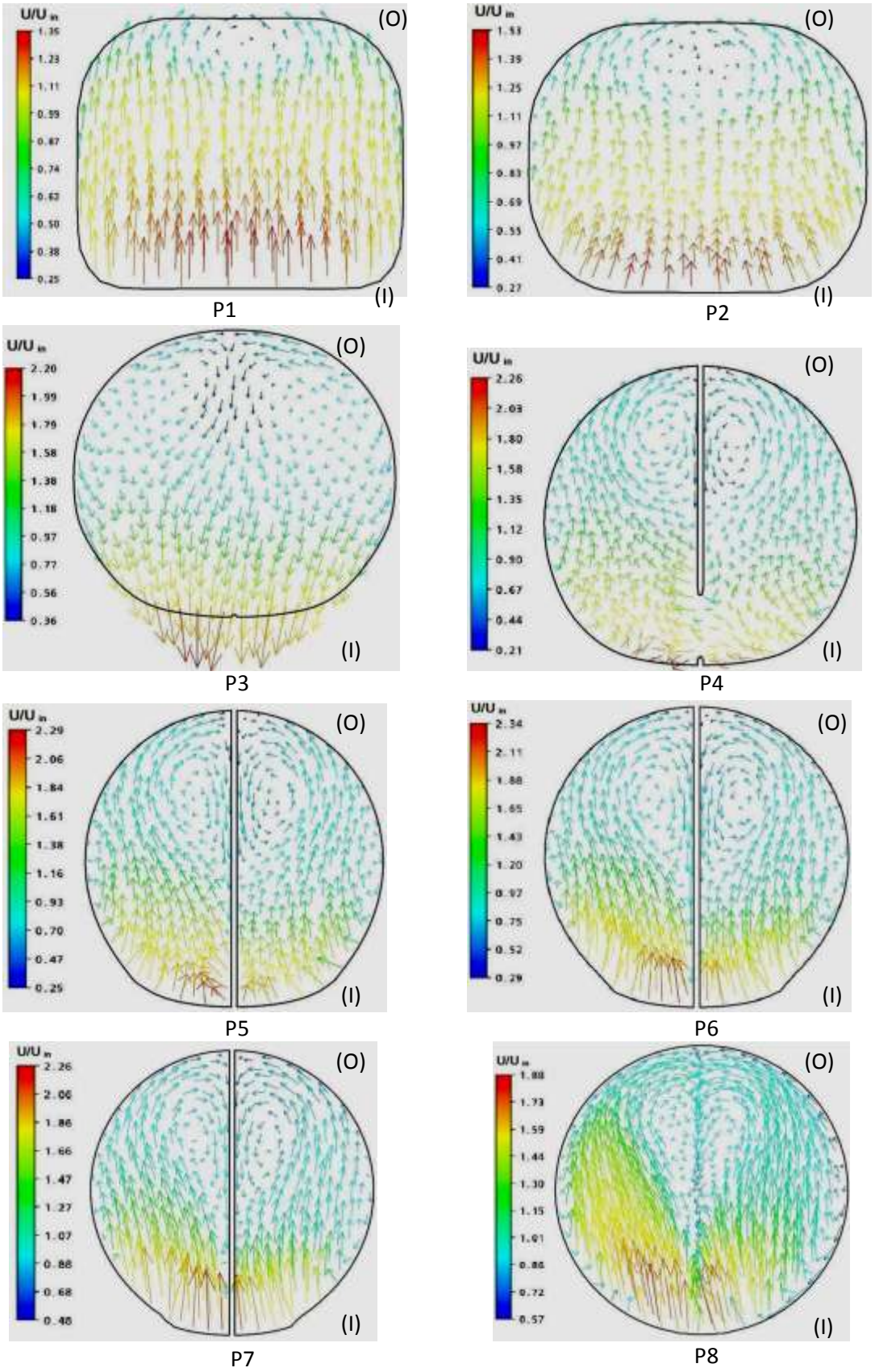

Figure 5-3 Velocity vector in the curved intake section at Q_{design}.

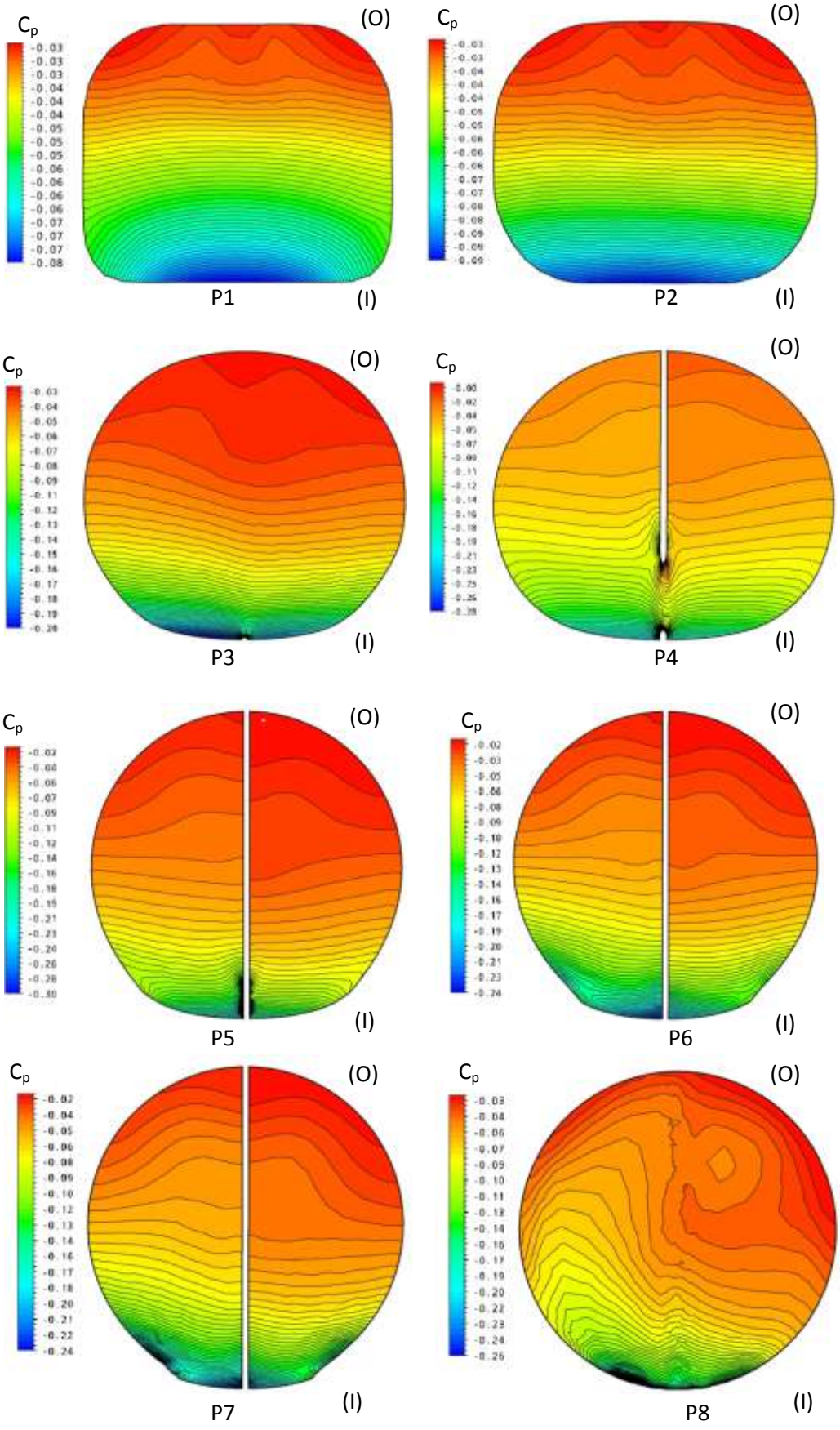

Figure 5-4 Pressure contour across the curved intake section at Q_{design}.

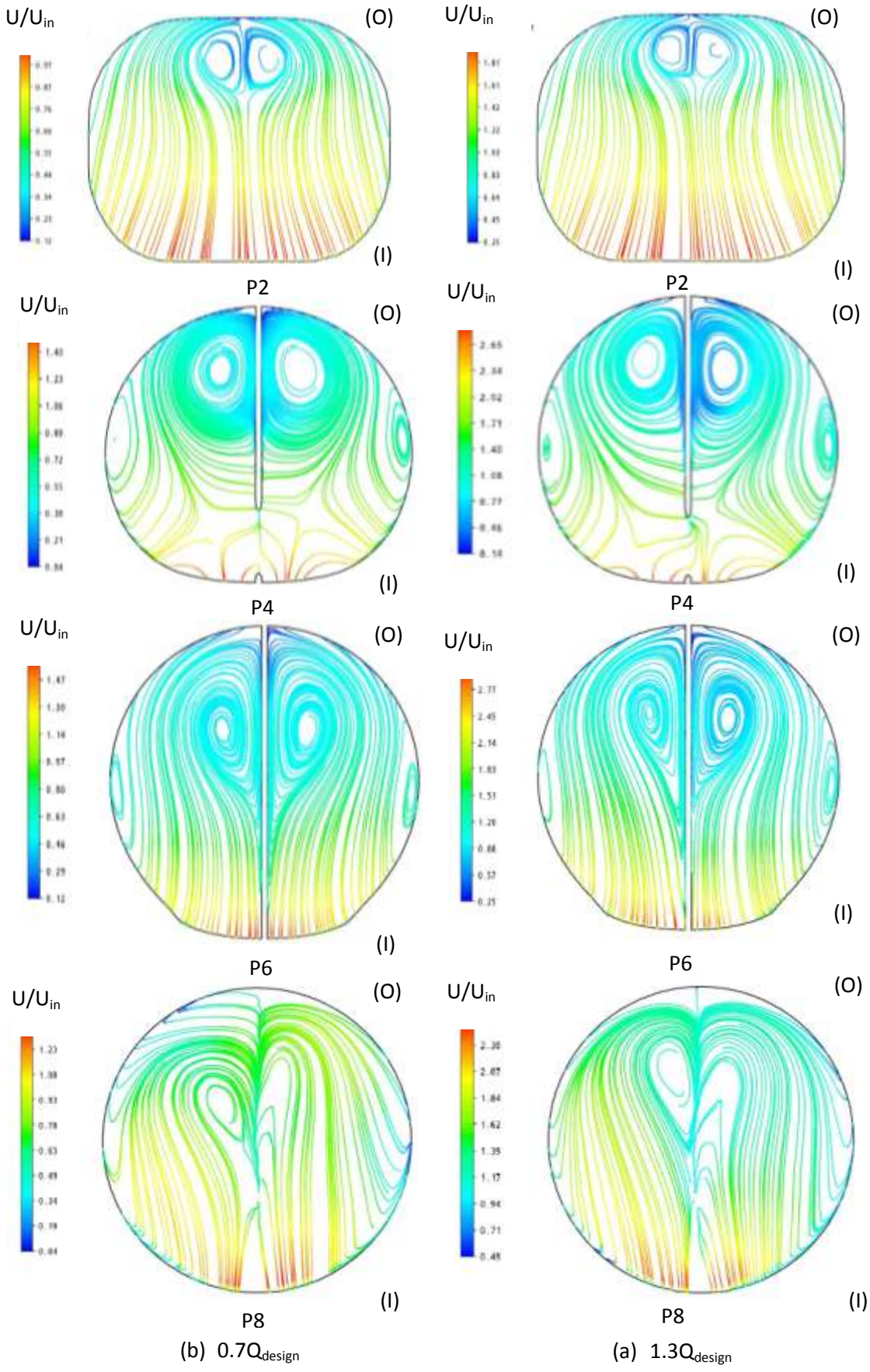

Figure 5-5 2D Streamline across the curved intake section at 0.7 and 1.3Q_{design}.

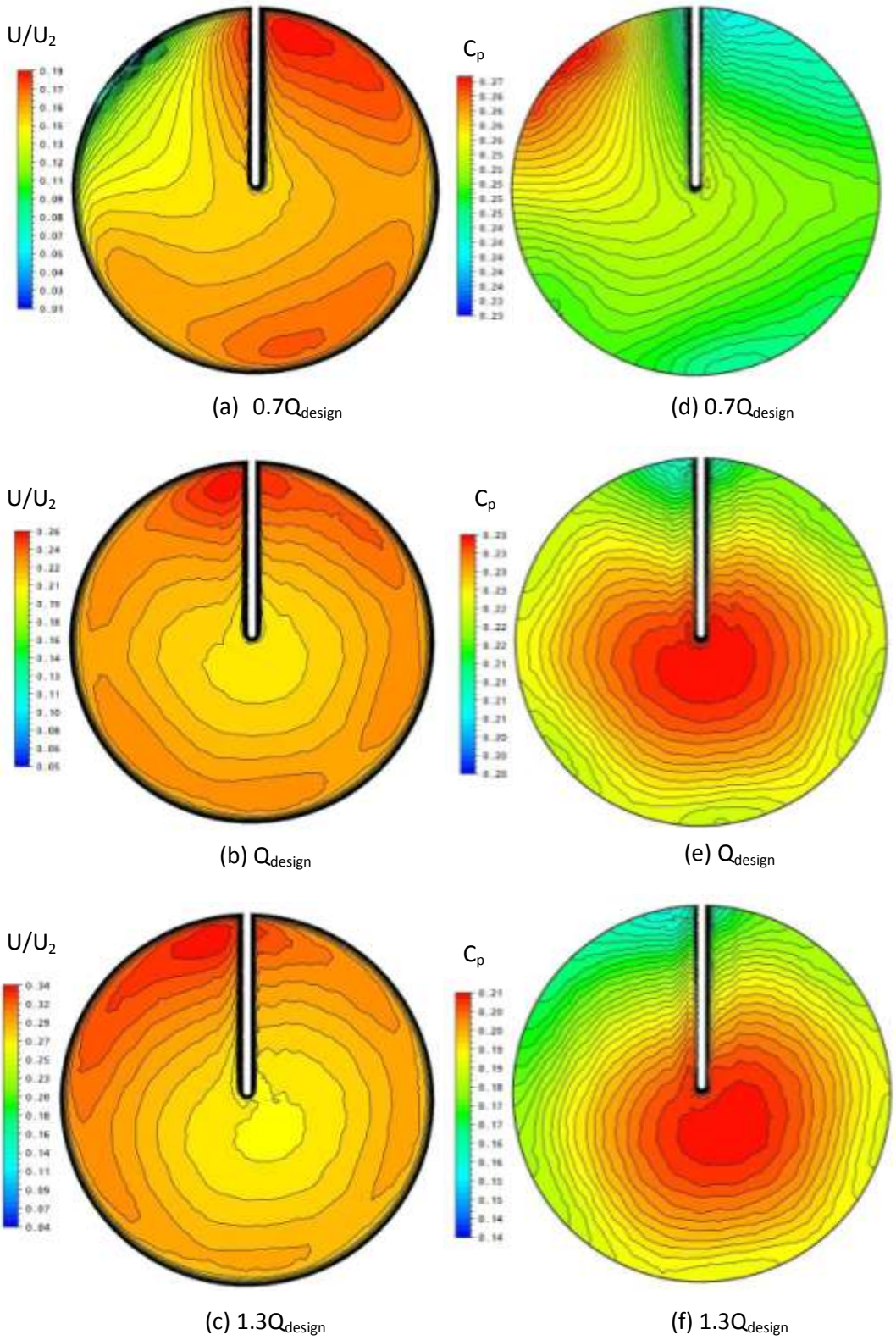

Figure 5-6 Velocity contour (a)-(c) and pressure contour (d)-(f) near impeller inlet at $0.7Q_{design}$, Q_{design} and $1.3Q_{design}$.

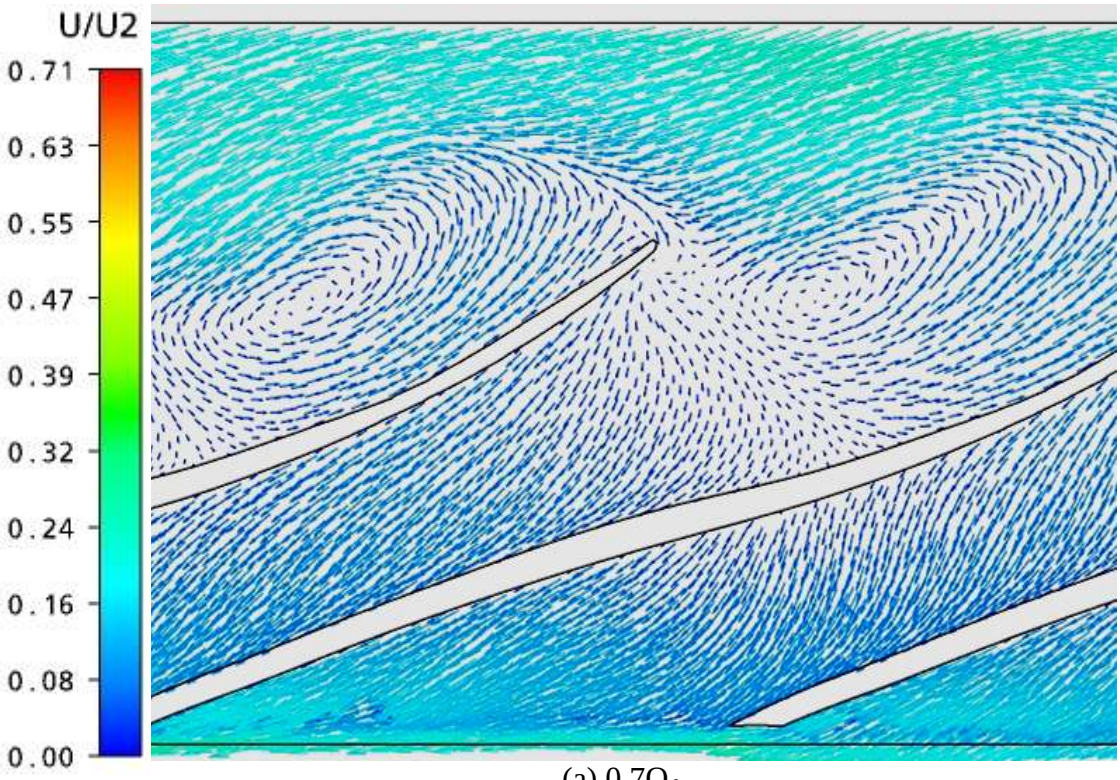

(a) $0.7Q_{design}$

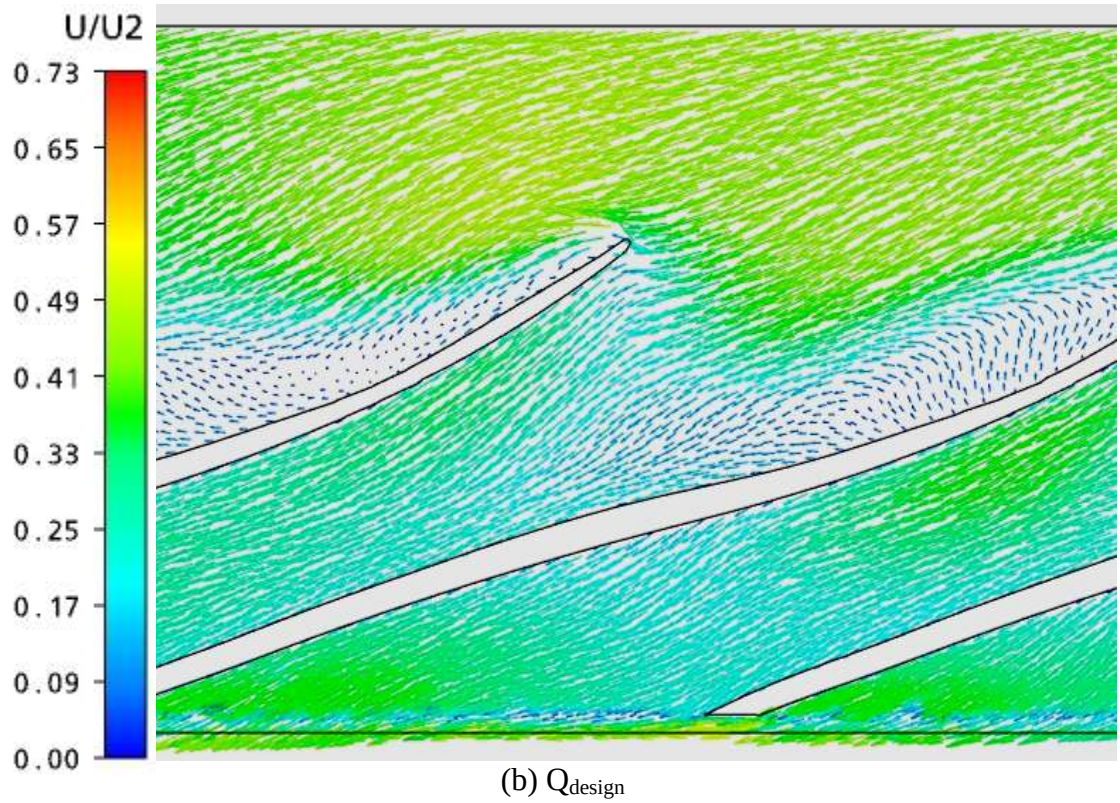

(b) Q_{design}

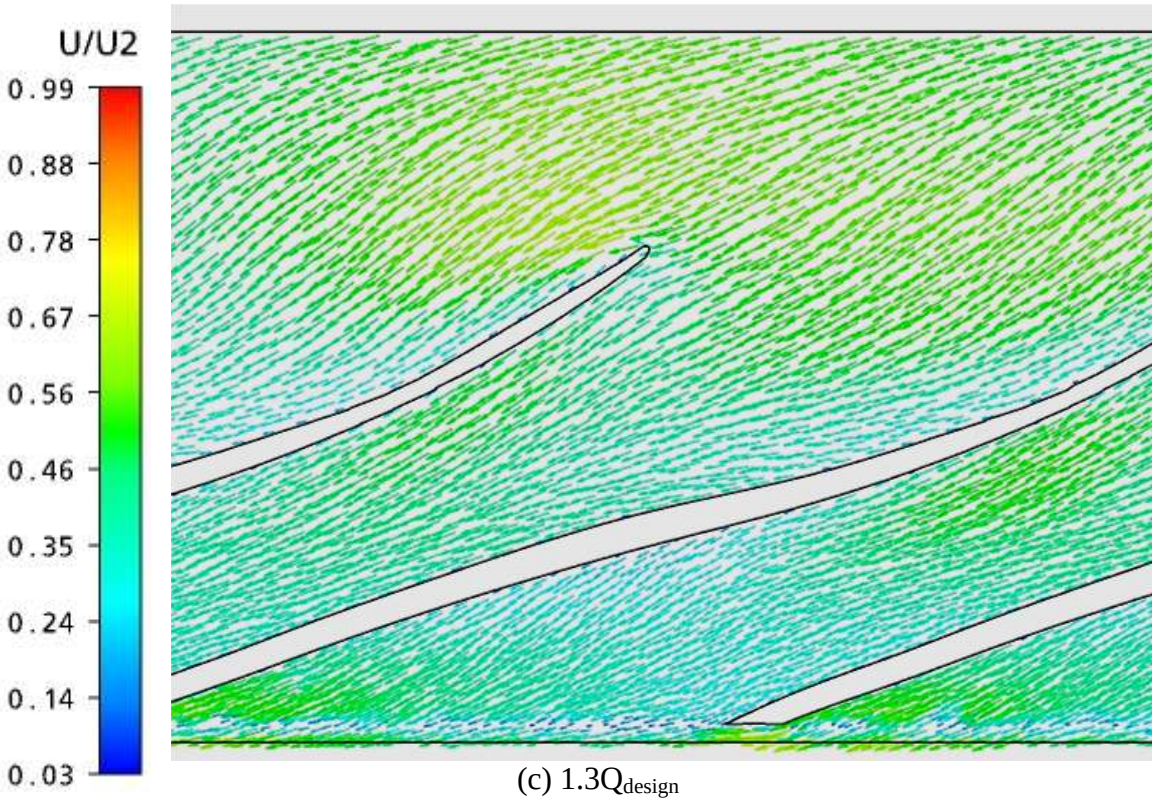

(c) $1.3Q_{design}$

Figure 5-7 Cascading view of flow within impeller passage at different flow rates near impeller shroud.

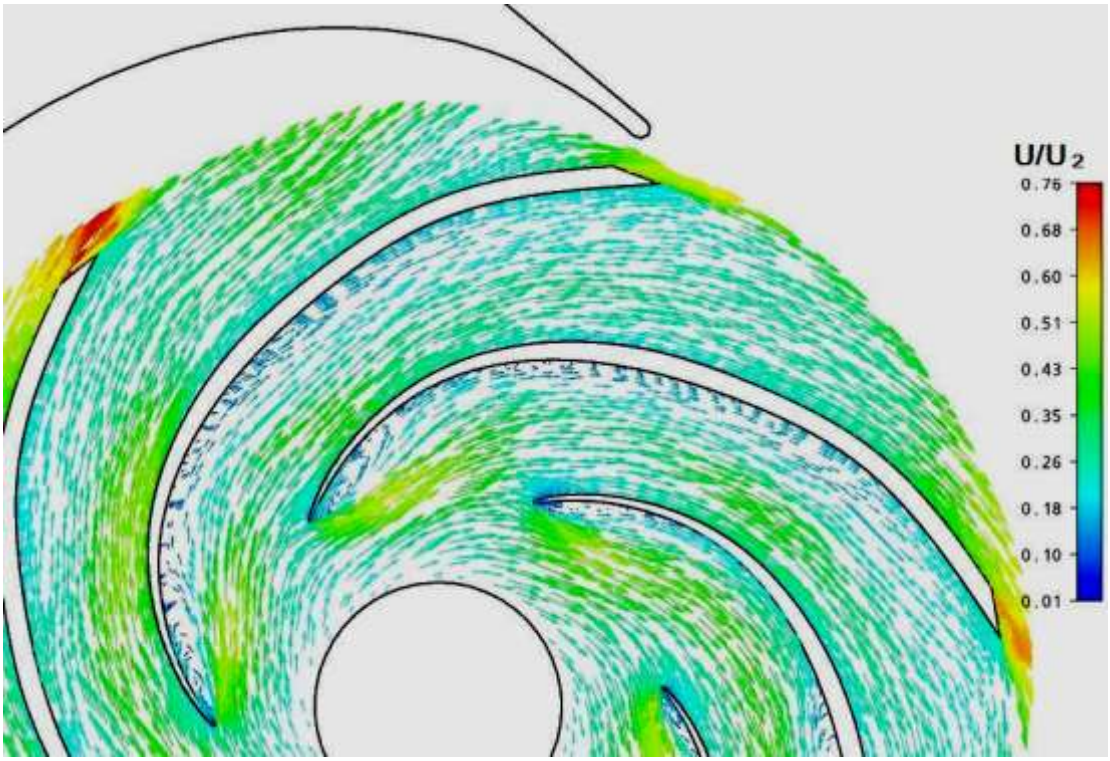

(a) $0.7Q_{design}$

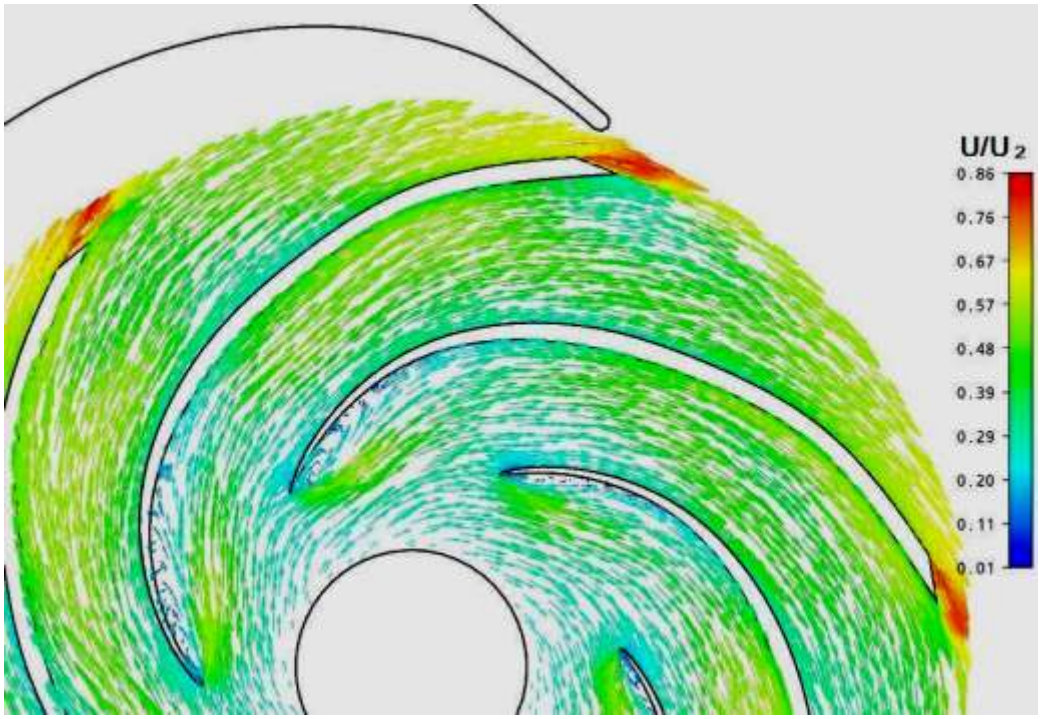

(b) Q_{design}

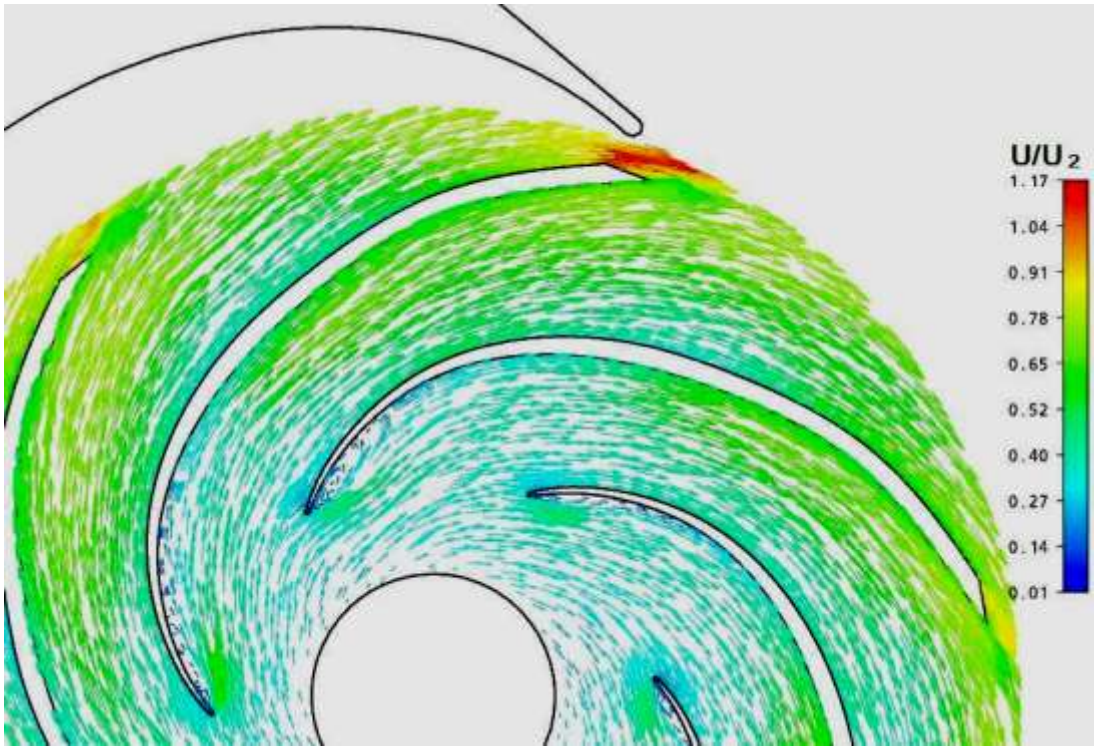

(c) $1.3Q_{design}$

Figure 5-8 Velocity vector at mid plan of impeller at $0.7Q_{design}$, Q_{design} and $1.3Q_{design}$.

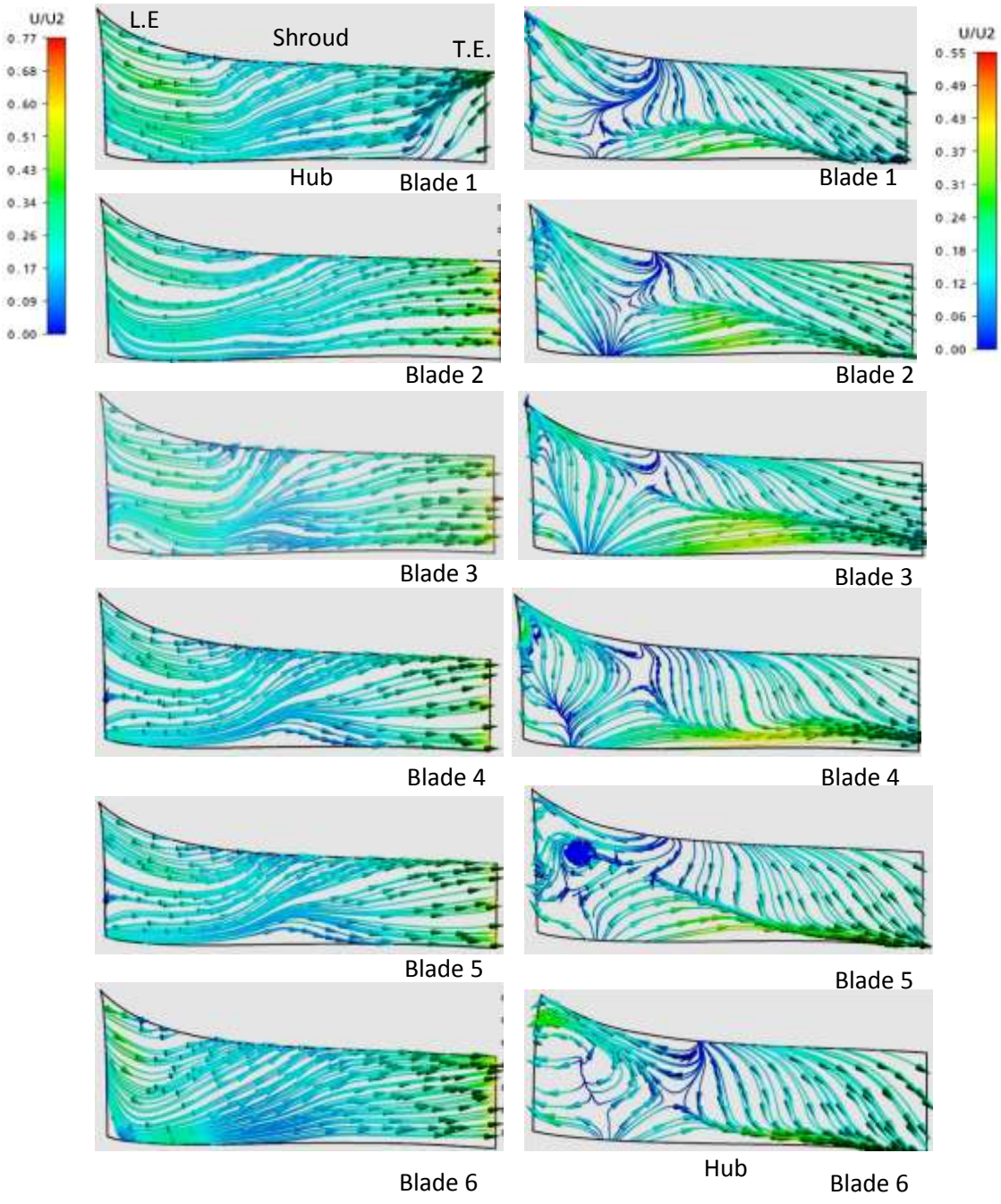

(a) Pressure Side (b) Suction Side

Figure 5-9 Surface streamlines on impeller blades surfaces at $0.7Q_{design}$.

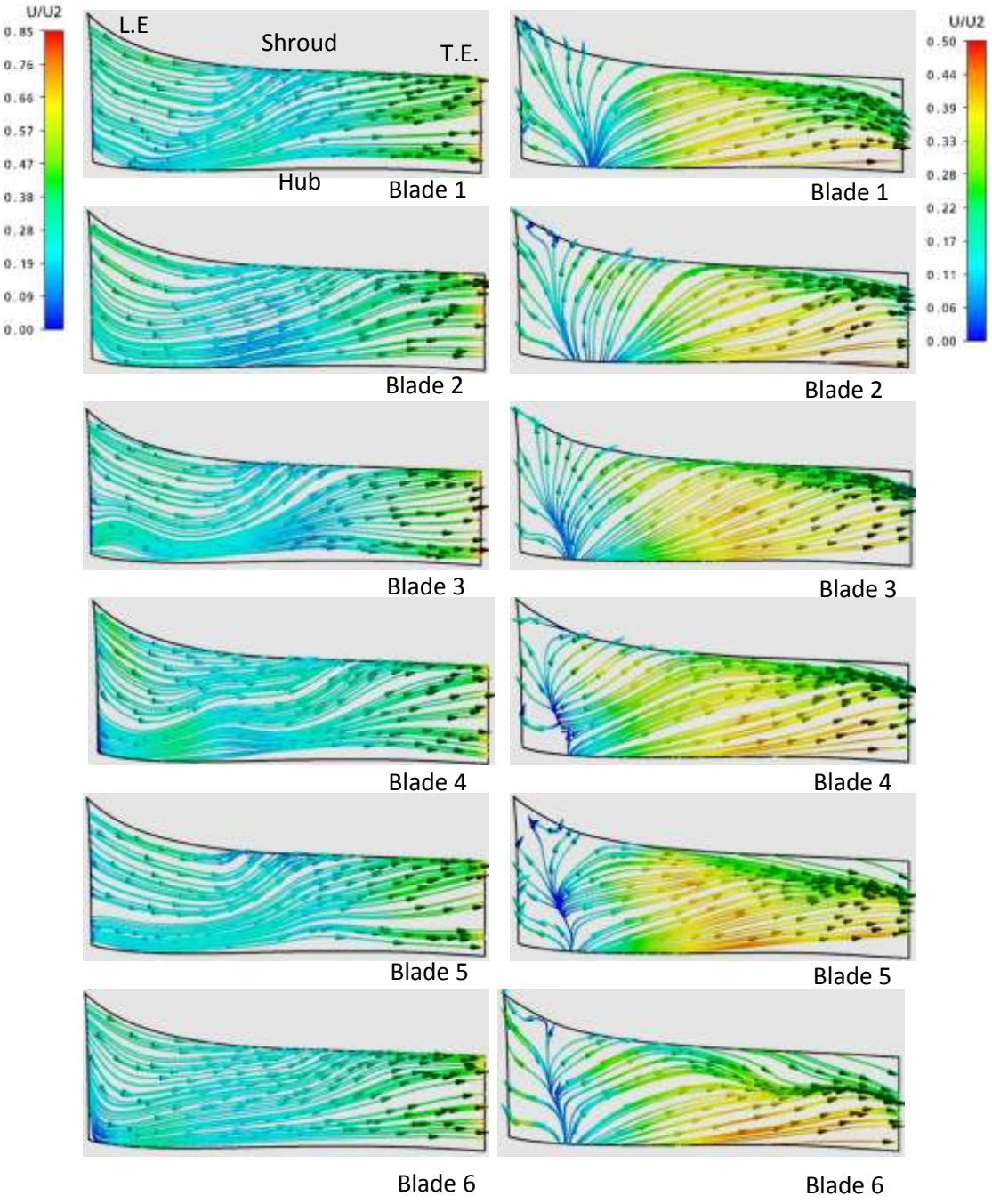

(a) Pressure Side (b) Suction Side

Figure 5-10 Surface streamlines on impeller blades surfaces at Q_{design} .

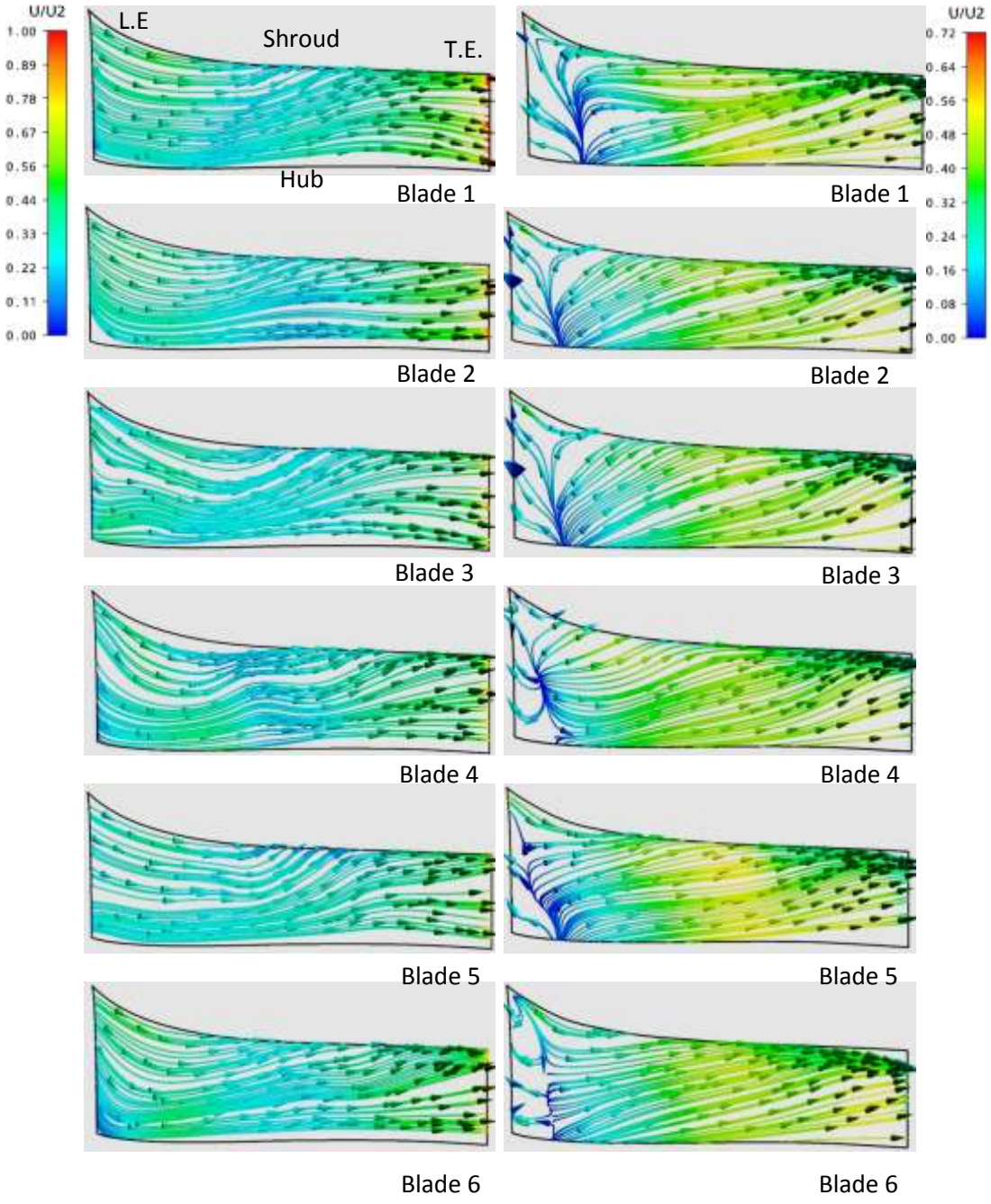

(a) Pressure Side (b) Suction Side

Figure 5-11 Surface streamlines on impeller blades surfaces at $1.3Q_{design}$.

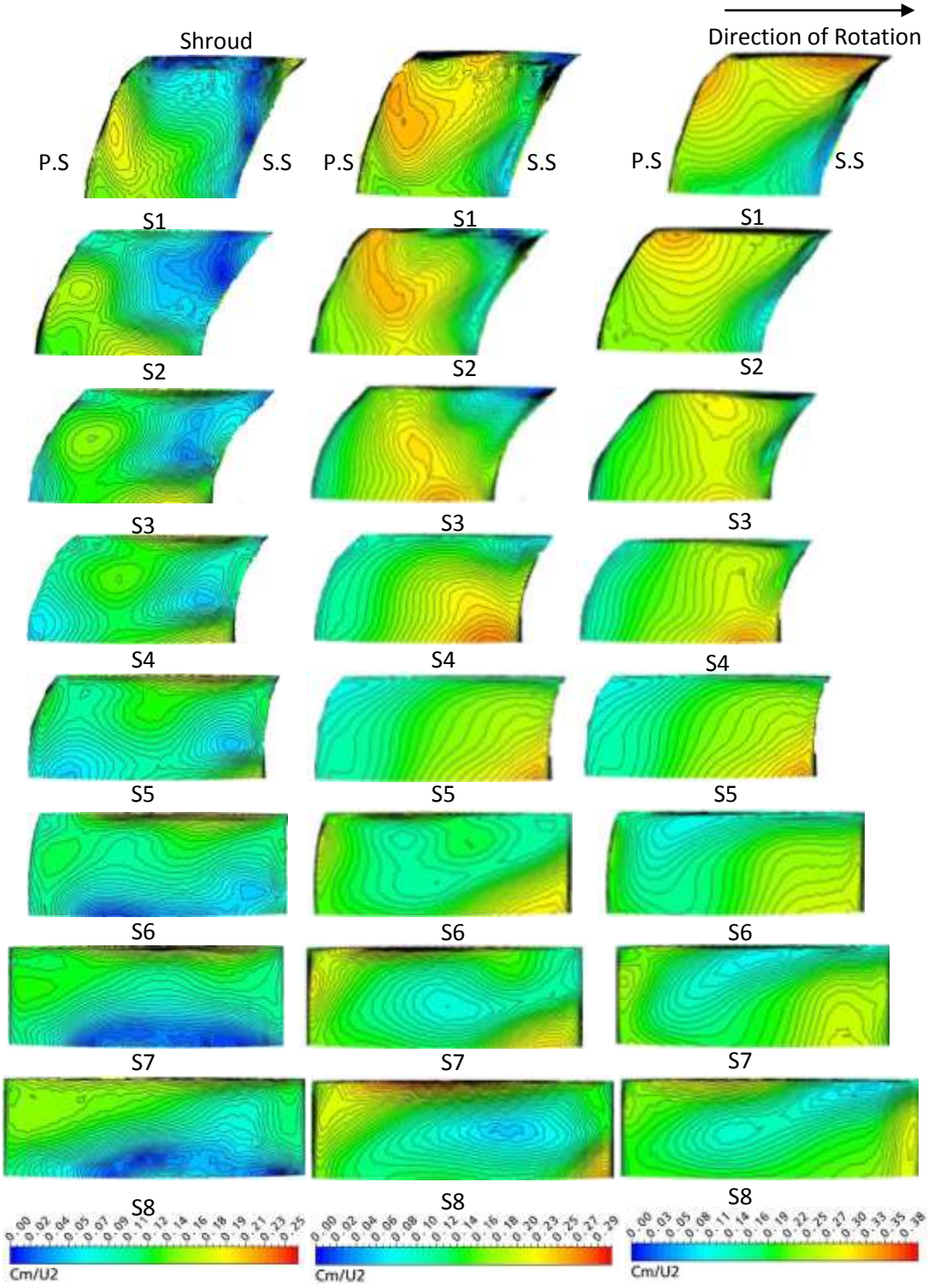

(a) $0.7Q_{design}$ (b) Q_{design} (c) $1.3Q_{design}$

Figure 5-12 Velocity contour inside impeller passage in streamwise direction at (a) $0.7Q_{design}$ (b) Q_{design} and (c) $1.3Q_{design}$.

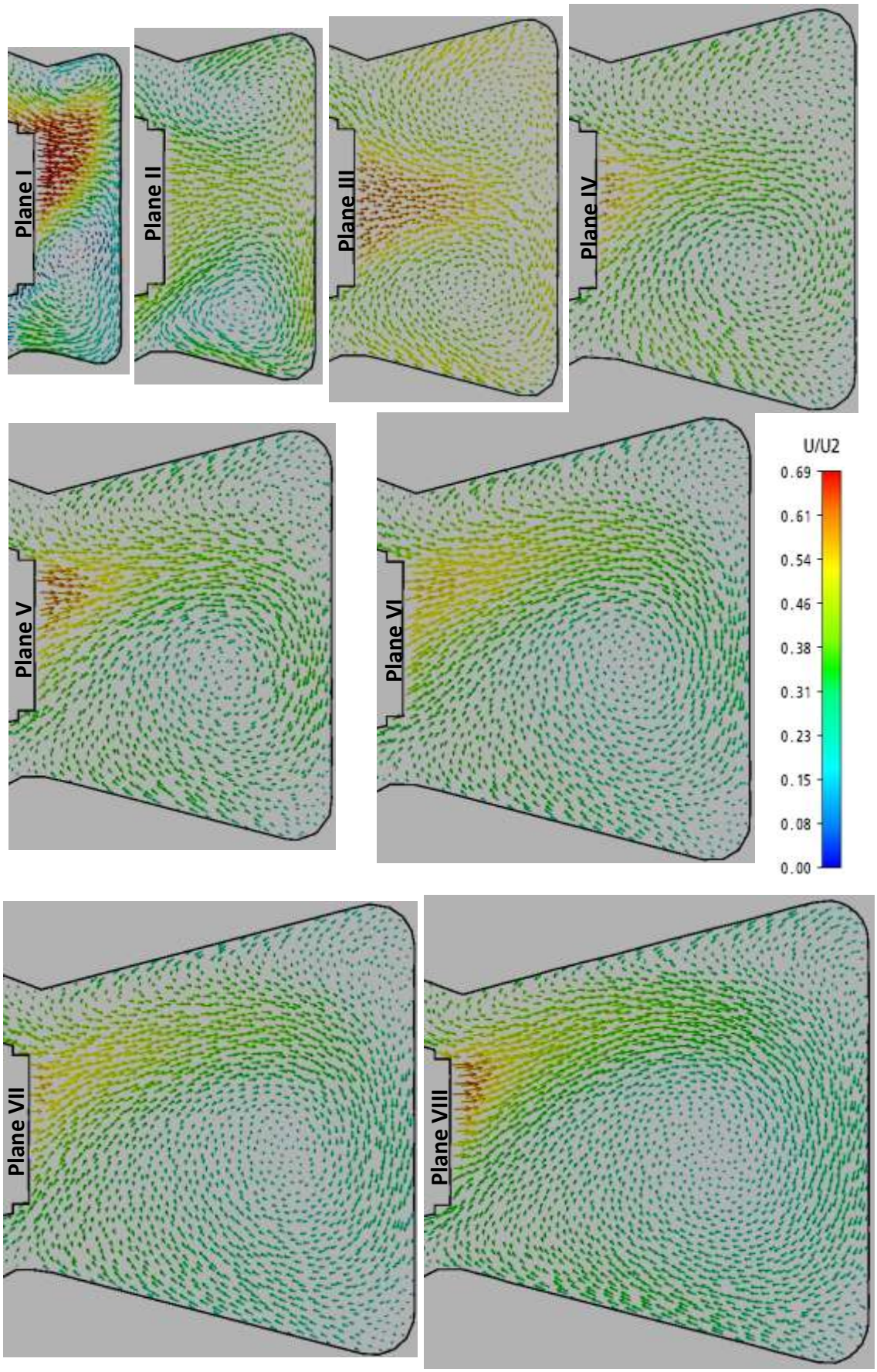

Figure 5-13 Velocity vector inside the volute casing at $0.7Q_{design}$.

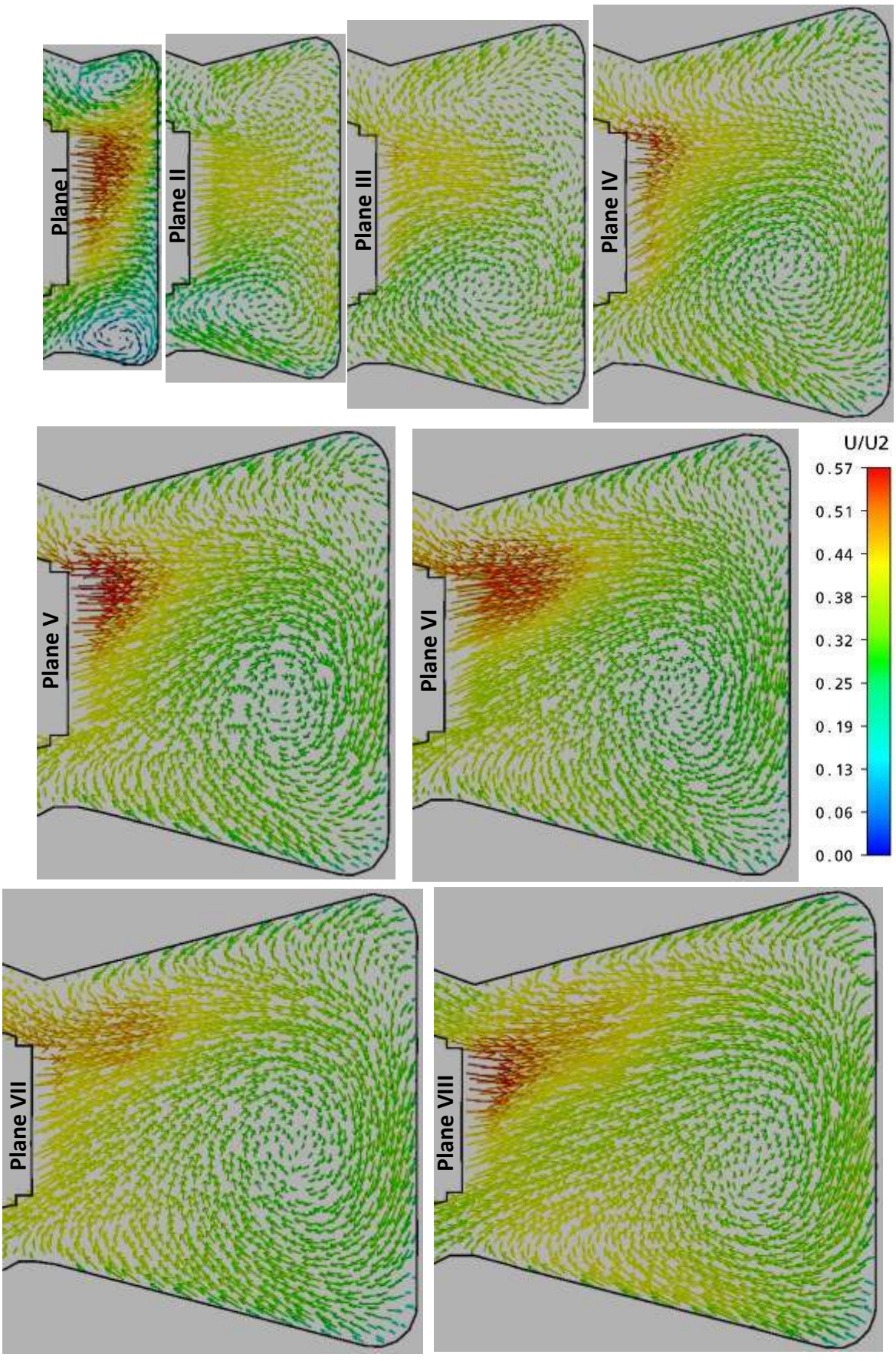

Figure 5-14 Velocity vector inside the volute casing at Q_{design}.

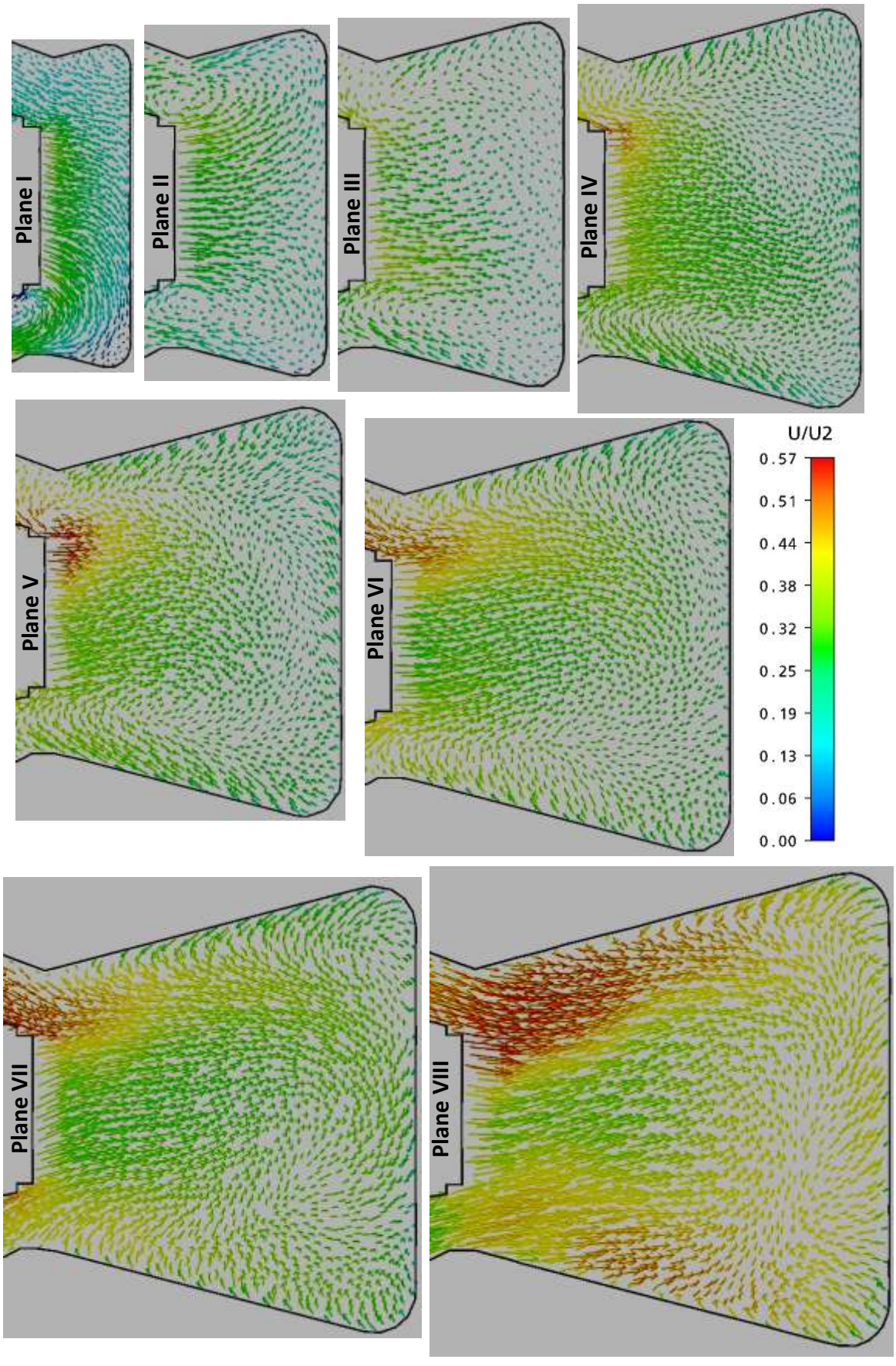

Figure 5-15 Velocity vector inside volute casing at $1.3Q_{design}$.

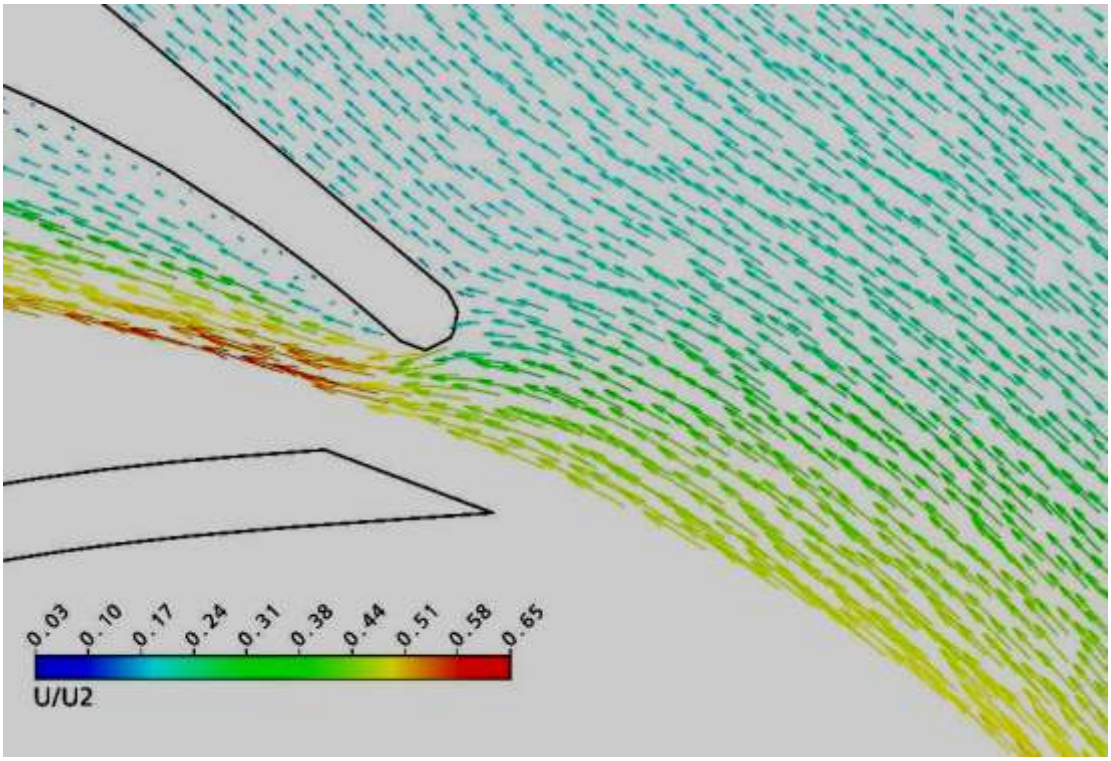

(a) $0.7Q_{design}$

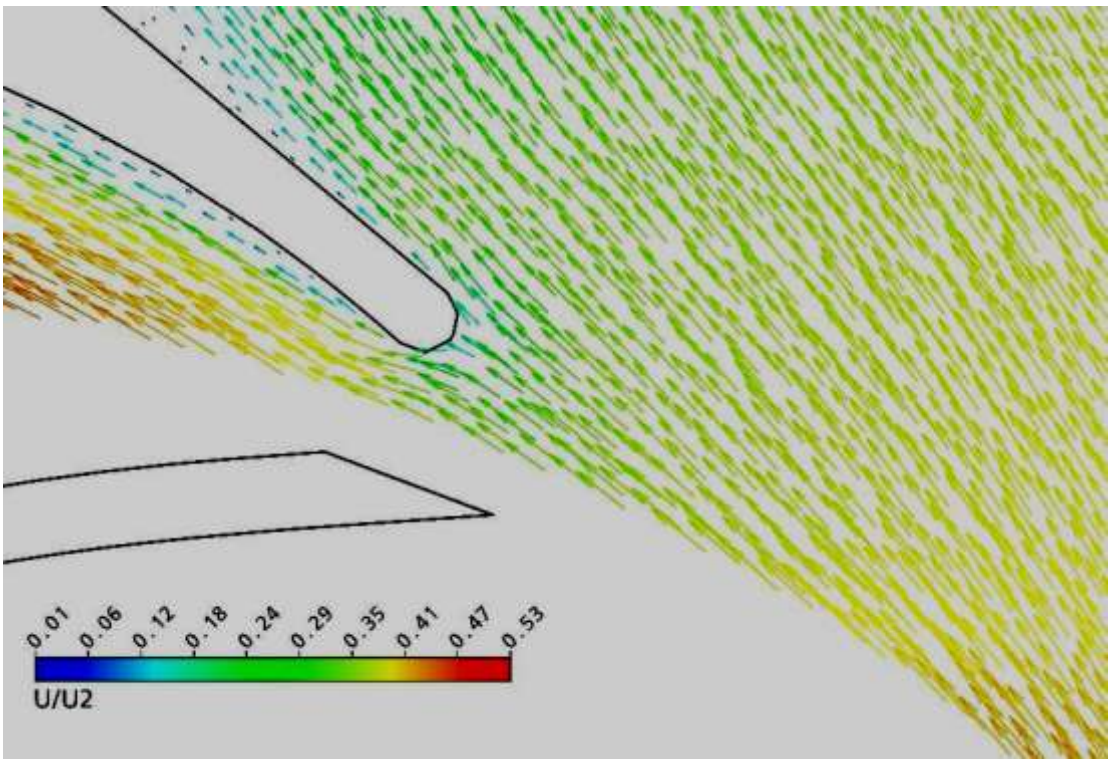

(b) Q_{design}

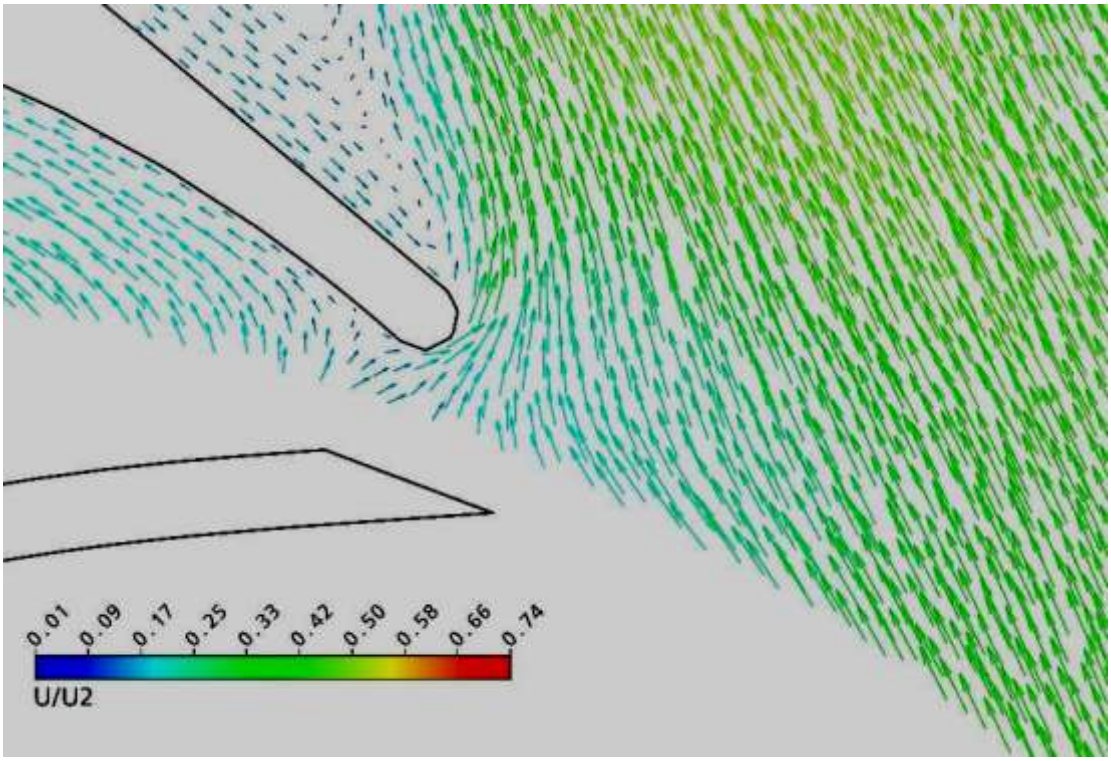

(c) $1.3Q_{design}$

Figure 5-16 Volute tongue incidence angle at different flow rates.

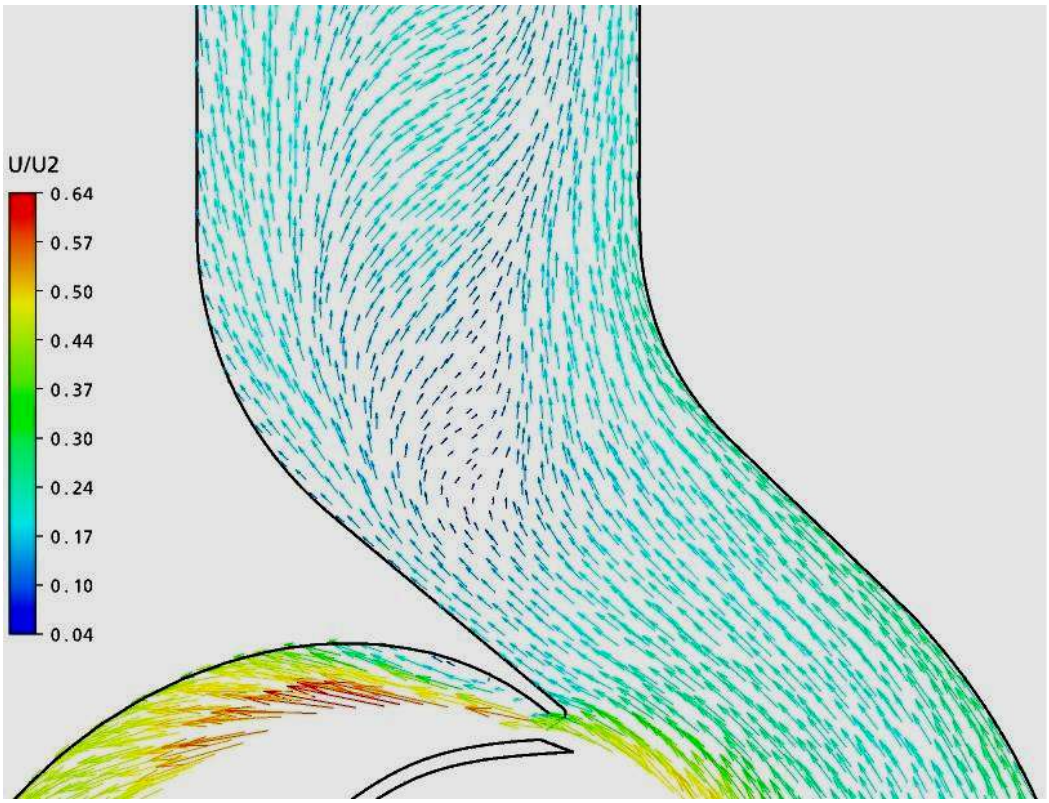

(a) $0.7Q_{design}$

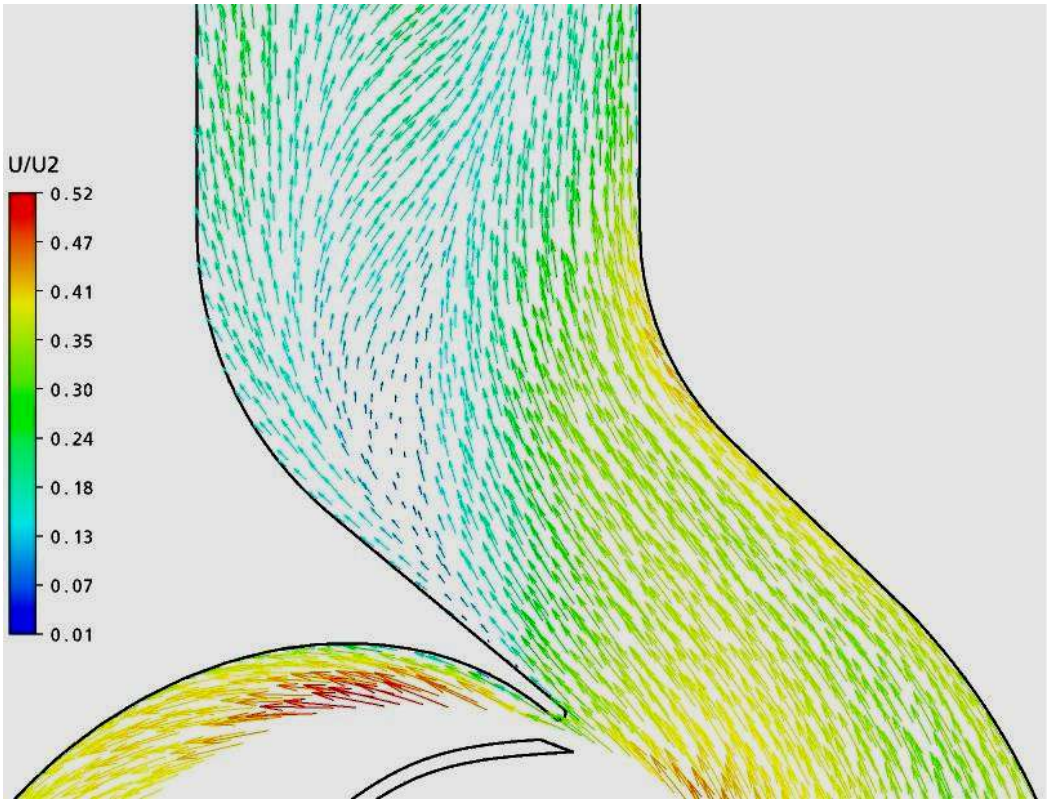

(b) Q_{design}

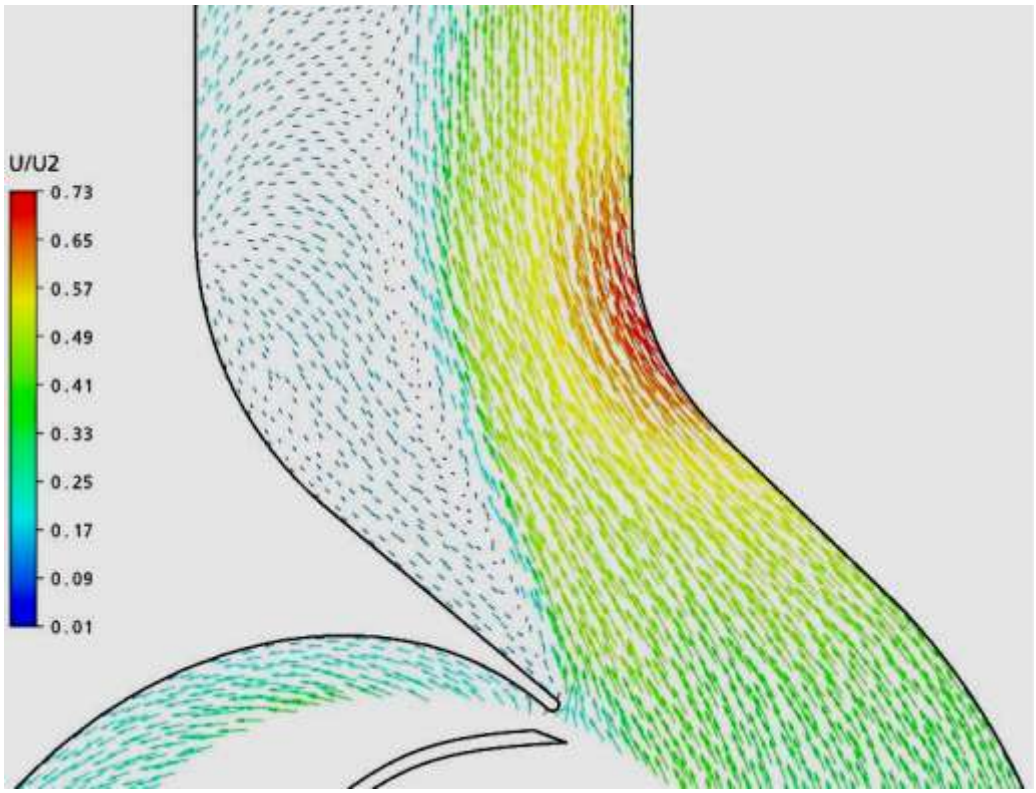

(c) $1.3Q_{design}$

Figure 5-17 Velocity vector near volute exit at different flow rates.

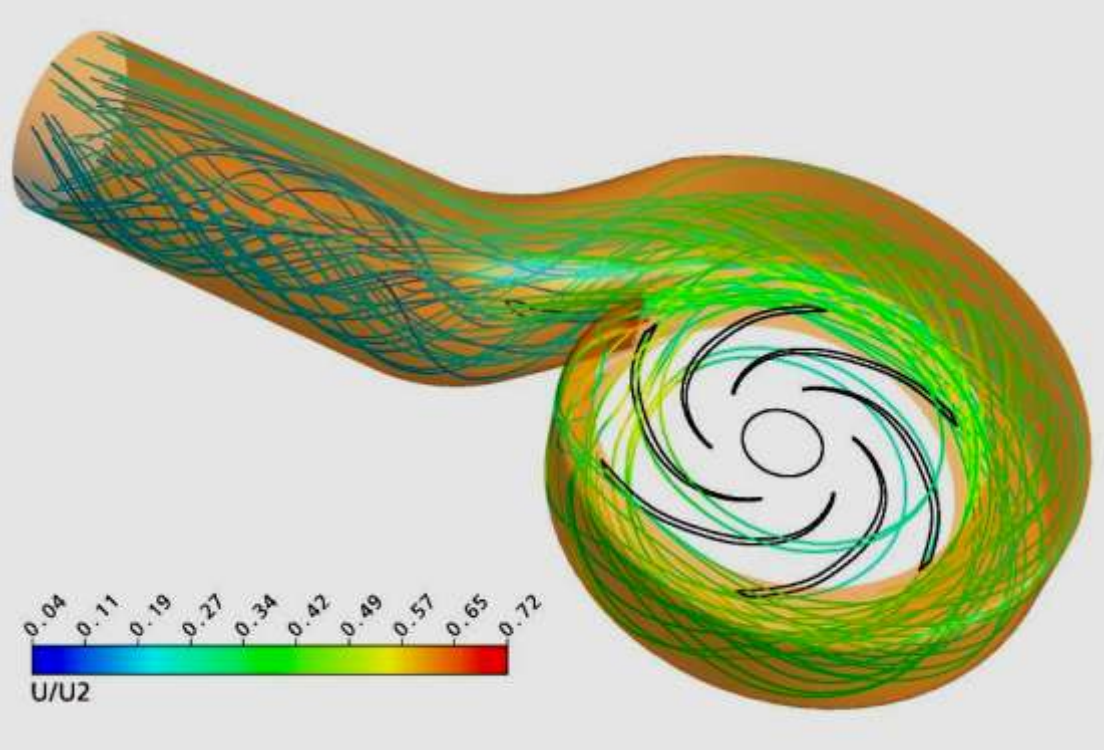

(a) $0.7Q_{design}$

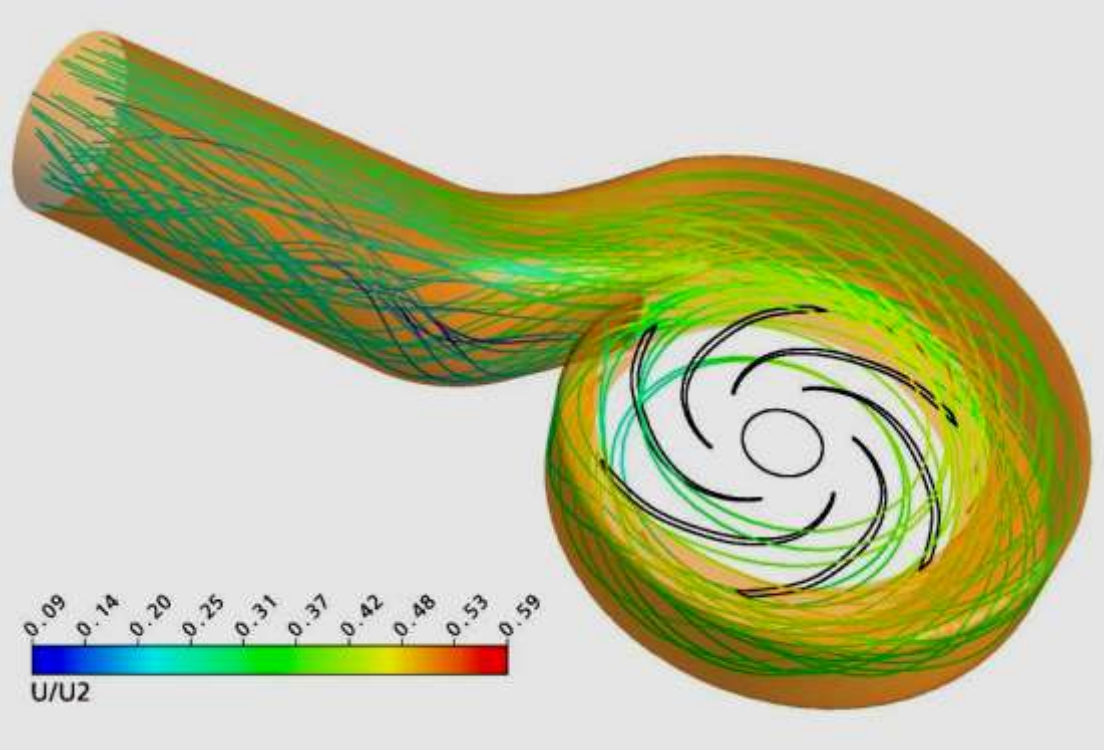

(b) Q_{design}

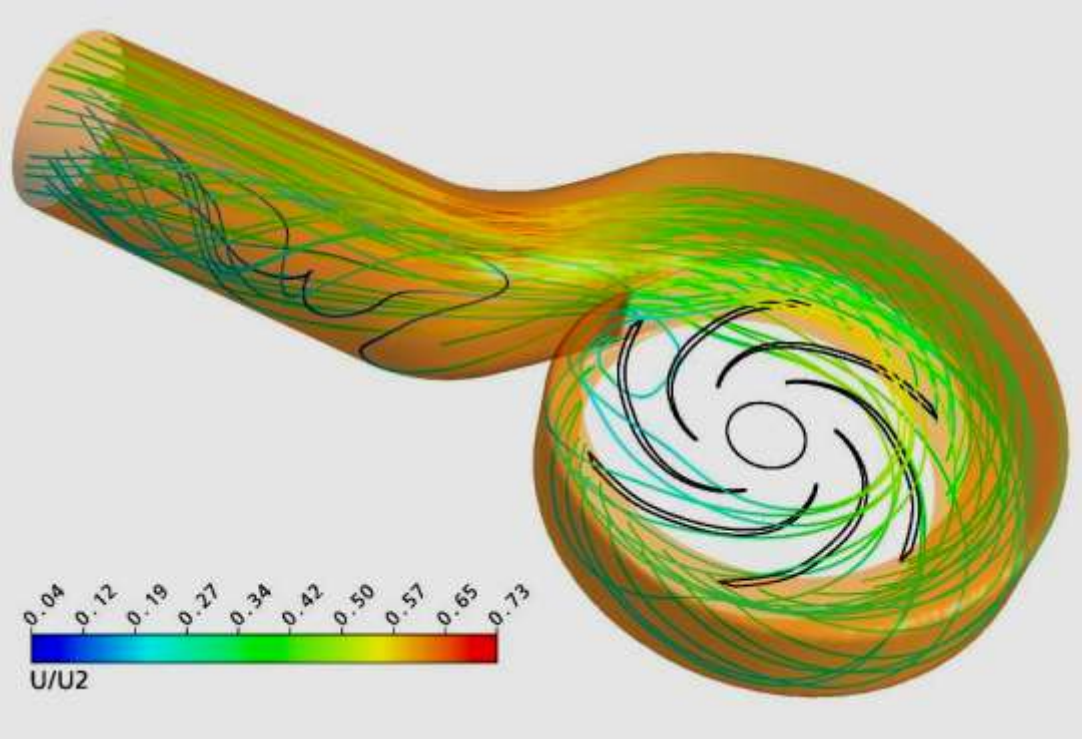

(c) $1.3Q_{design}$

Figure 5-18 Streamlines inside volute casing at different flow rates.

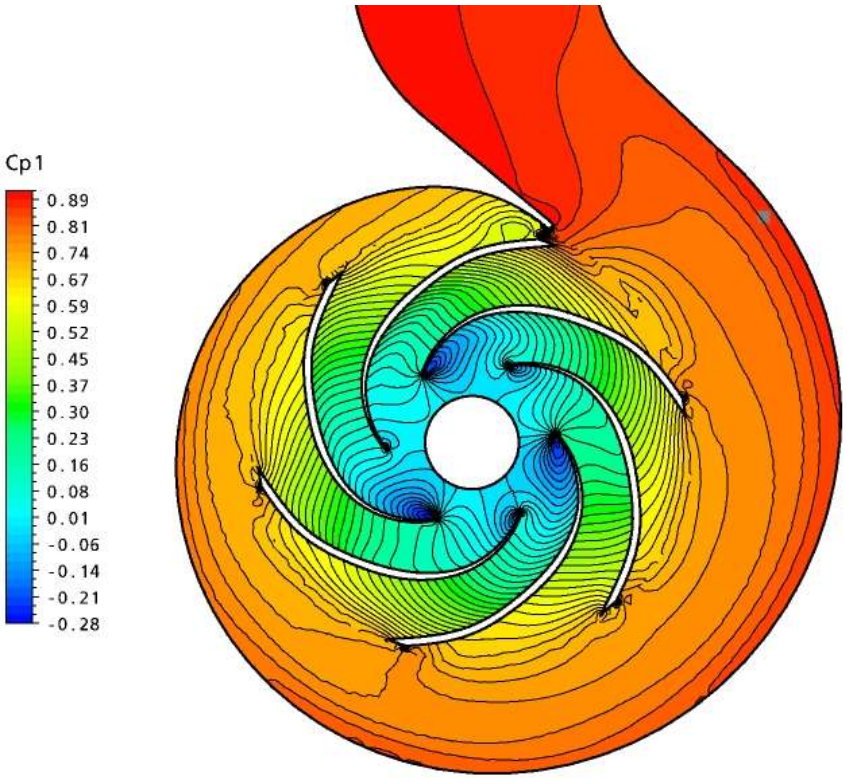

(a) $0.7Q_{design}$

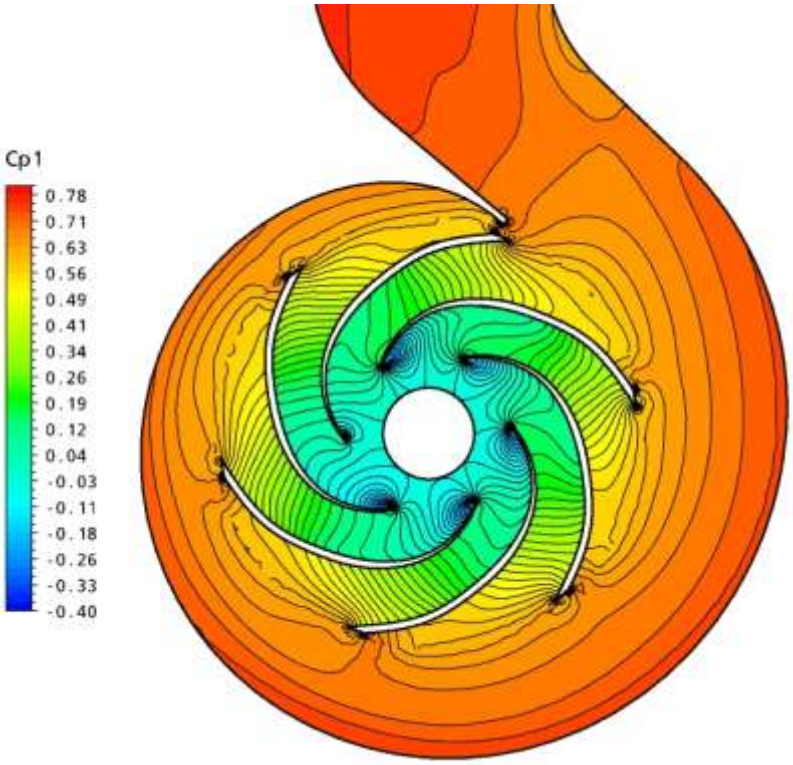

(b) Q_{design}

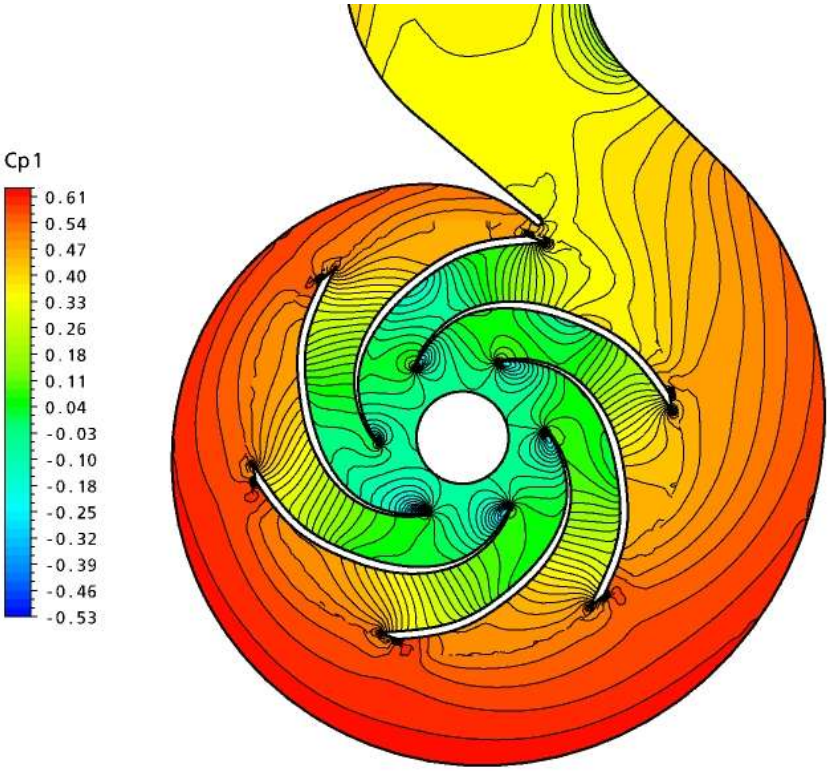

(c) $1.3Q_{design}$

Figure 5-19 Pressure distribution around volute casing at various flow rate.

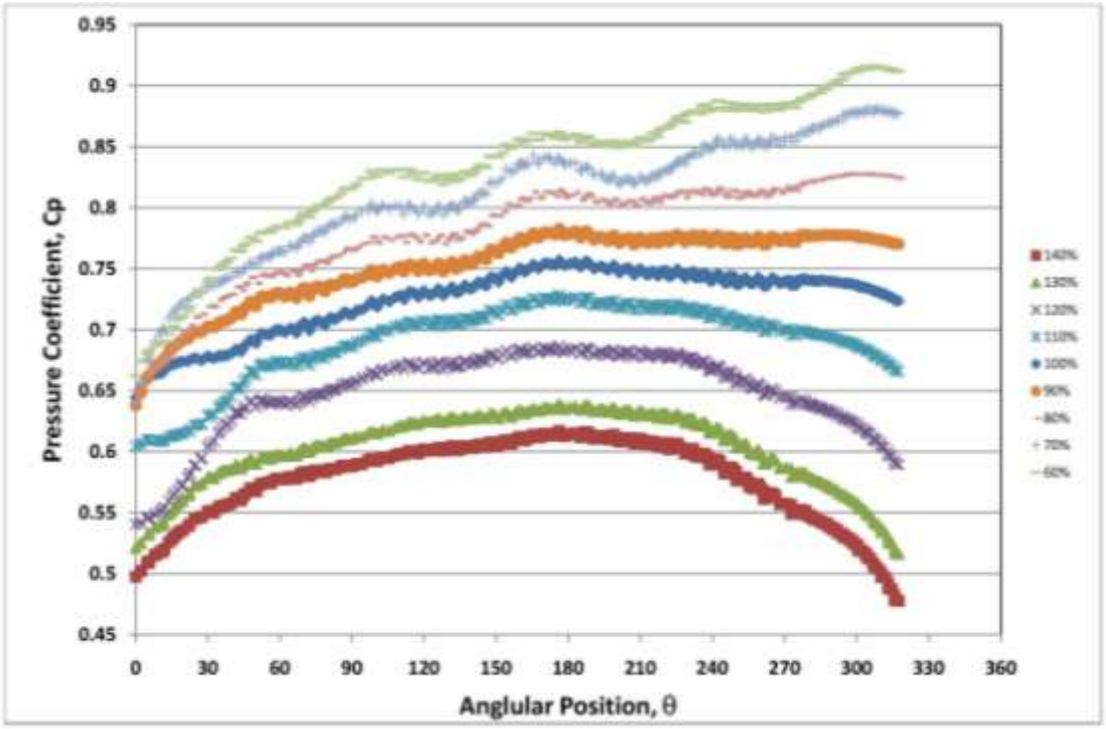

Figure 5-20 Pressure coefficient on the volute casing wall in circumferential direction.

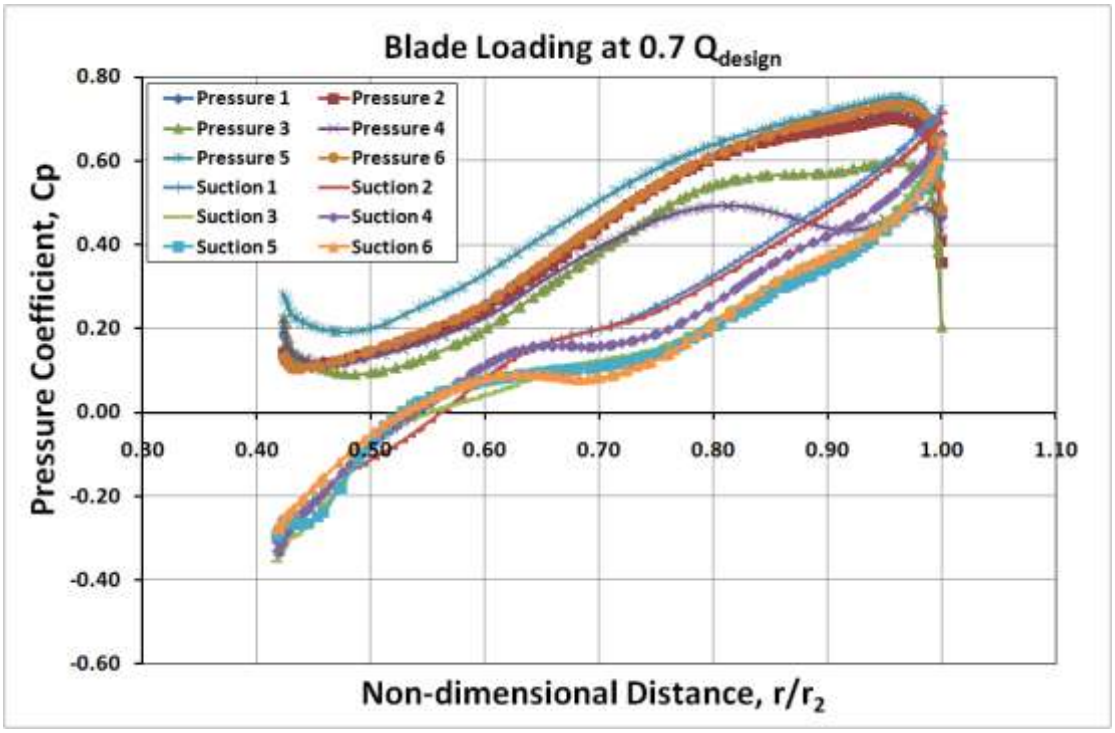

(a) $0.7Q_{design}$

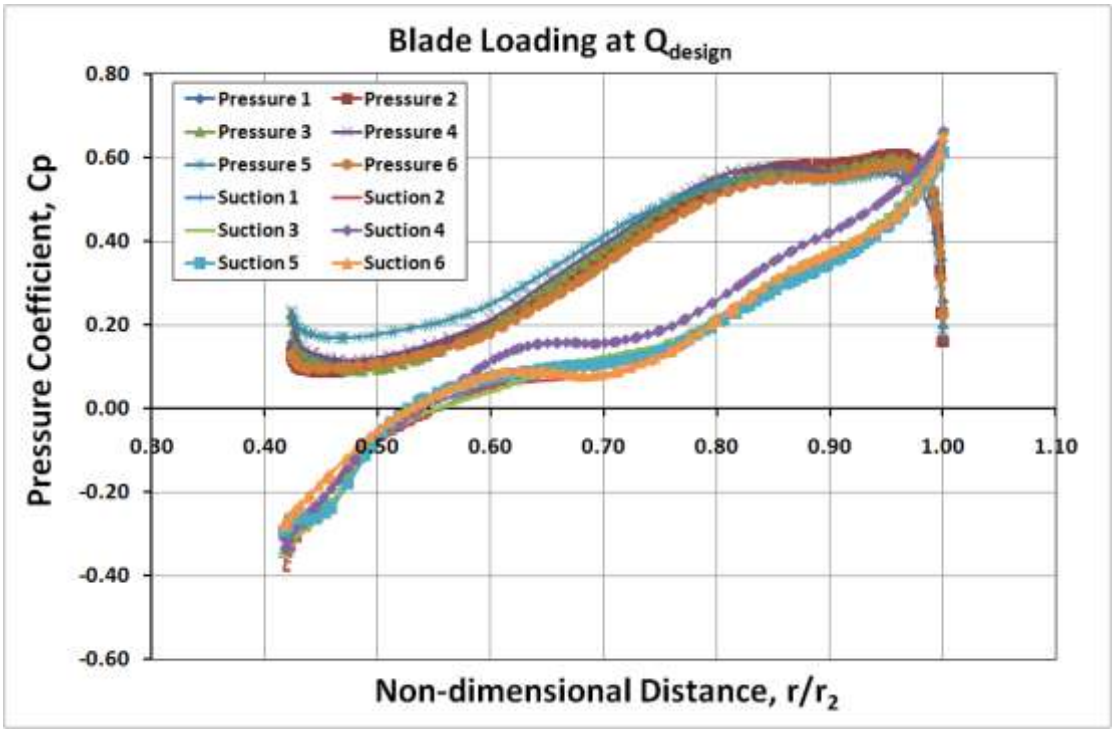

(b) Q_{design}

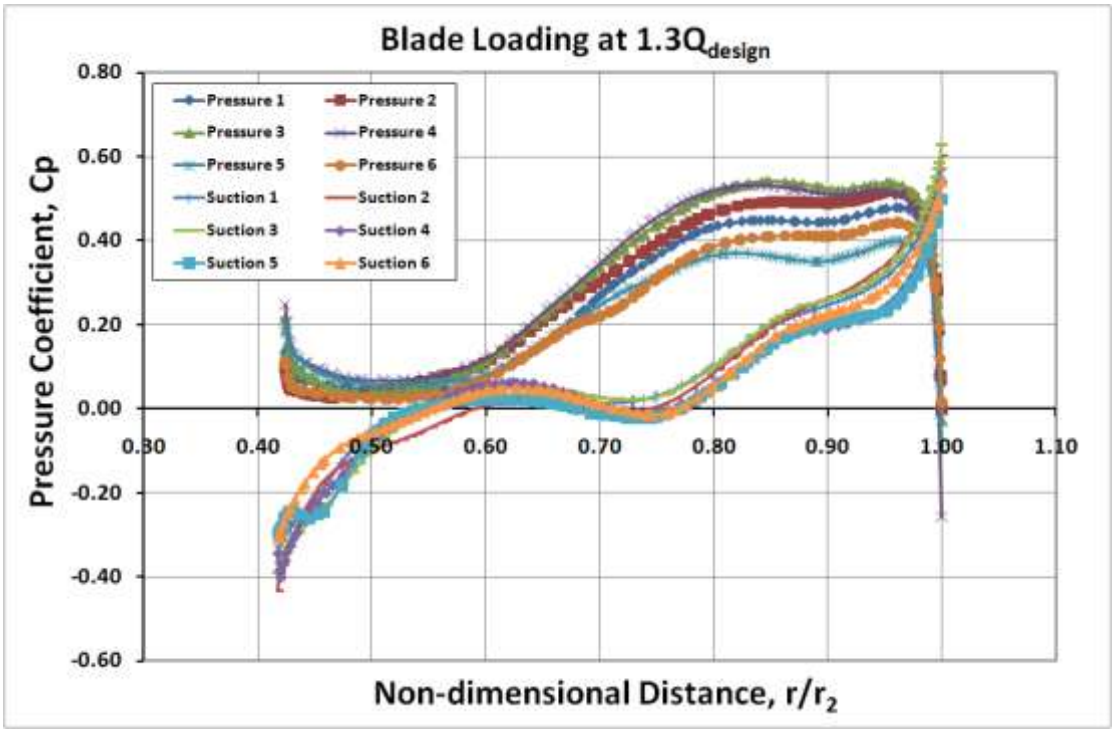

(c) $1.3Q_{design}$

Figure 5-21 Pressure loading on impeller blades at (a) $0.7Q_{design}$ (b) Q_{design} and (c) $1.3Q_{design}$.

CHAPTER 6 UNSTEADY IMPELLER VOLUTE TONGUE INTERACTIONS

In Chapter 5, it has been highlighted that the jet wake flow formation within the impeller passage is depending on the upstream and leading edge flow conditions as well as the flow rate. Vortex flow formation occurs when the flow discharge circumferentially from impeller into volute casing. In this chapter, an unsteady analysis of the jet wake flow and impeller volute interaction will be discussed.

6.1 Wake Flow Interaction at Impeller Exit

Dring et al. (1982) indicated two distinct mechanisms of rotor-stator interactions: potential and wake interactions. The potential interaction is a potential flow effect induced by the inviscid interaction because of the relative motion between rotor blades and stator vanes. Wake interaction originated from the impingement and convection of wakes shed from the impeller passages and moving through the successive diffuser passages.

Figure 6-1, Figure 6-2 and Figure 6-3 show a series instantaneous non-dimensional meridional velocity at the impeller exit with different flow rate. The frame is taken at a cut plane at the impeller exit Passage 6 with $r/r_2 = 0.99$. The figures are plotted according to the impeller trailing edge relative position to the volute tongue at Passage 1, 6 and 5 as indicated in the enlarged box area in Figure 2-2. Passage 1 exit is closest to volute wall and tongue. Flow discharge from Passage 6 will interact strongly with volute tongue as the impeller rotates. At 0 °, the suction side of impeller blade trailing edge is aligned to the volute tongue and for every time step or blade rotation of 6 °, a frozen frame is made. The volute tongue position is marked with dotted line as shown in these figures. In these series of frozen frames, it is clearly

seen that evolution of the distorted velocity profile and jet/wake structure at impeller exit.

Figure 6-1 shows the jet wake flow pattern at $0.7Q_{design}$. As the impeller rotates, there is a strong impeller volute tongue interaction due to proximity of trailing edge and volute tongue. For Passage 6 at 0 ° blade rotation, the wake core is at impeller exit with low flow region spanning across hub suction corner towards pressure side. As the impeller rotates further, the wake core interaction with volute tongue becomes prominent.

From 6 ° to 30 ° blade rotation, a wake core interaction with volute tongue is observed. From 6 ° to 12 ° blade rotation, the wake core is suppressed when the impeller blade suction side moved passed the volute tongue. This can be referred as wake shedding from impeller exit and subsequently impingement on volute tongue. From 18 ° to 30 ° blade rotation after the volute tongue moved pass the wake core, the wake core profile did not changed much as compared to the 6 ° and 12 ° rotation.

This wake flow shedding action or interaction caused the wake core profile distorted. This can be explained that the blade passing frequency is much higher than the wake flow shedding frequency at the impeller exit. The blade passing frequency f_{bp} at the impeller exit is 145 Hz. However the fluid velocity over blade tip velocity is only 0.7 and is much lower than f_{bp}. Hence the wake flow shedding and momentum of fluid at impeller exit is being carried away and suppressed by impeller blade and volute tongue interaction.

After 30 ° blade rotation, the wake core interaction with volute tongue is loosely coupled. This can be seen from Figure 6-1 that the wake core or low flow region fading slowly from 30 ° to 48 ° blade rotation.

For Passage 1 and 5, the impeller and volute interaction is weak as compared to passage 6 due to unblocked impeller exit. As the impeller rotates deep into the mid passage of the Passage 6, the wake core of at the impeller exit at Passage 1 and 5 are concentrating on the suction hub side. The wake core shape and intensity is remained constant. When the volute tongue is passed through the mid span of Passage 6, then there is a diffusion of the wake core at Passage 1 and 5. The diffusion of the wake core is spanning from suction side to pressure on hub region.

This kind of wake flow pattern is much depends on the upstream jet/wake formation at mid passage and as well as the severity of flow separation caused by the leading edge as discussed in Section 5.2.4. As the impeller blade trailing edge advancing in angular direction, the wake core position and strength also changed accordingly. From $0°$ to $30°$, the wake core is emerging and diminishing afterwards. This is coincided with the rising and dropping of the pump delivery head as shown in Figure 4-6. The wake flow pattern is remained diagonal even a full blade-to-blade pitch is over.

Figure 6-2 shows the jet wake flow pattern at Q_{design} near impeller exit. The jet wake flow pattern is different from part load condition $0.7Q_{design}$. When the trailing is just aligned with volute tongue at $0°$ blade rotation, the wake core is concentrating near impeller suction. As explained in Figure 5-12(b), the accumulation of wake flow is because of flow structures development upstream of impeller passage. Similar to $0.7Q_{design}$, there is a wake flow shedding from impeller and wake flow impingement on volute tongue when the impeller is rotating. The wake core is slowly diffused at impeller Passage 6 and no strong impeller volute interaction reflection upstream as the impeller rotates. As the volute tongue moving deep into the impeller exit, the

accumulation of low flow region emerged again on the suction side of the blade trailing edge. For Passage 1 and 5, there is no strong impeller volute tongue interaction near impeller exit.

Figure 6-3 shows the jet wake flow pattern at $1.3Q_{design}$ near impeller exit. The wake flow at impeller Passage 6 is spanning diagonally from suction shroud corner to pressure hub corner. The wake of flow core is near pressure hub corner with high velocity flow concentrated on shroud side. Initially, there is an accumulation of low flow near suction shroud corner. As the impeller rotates and volute tongue deep into impeller exit, the wake flow core is slowly diffused away in impeller rotating direction. Again, there is a wake impeller and volute tongue interaction at higher flow rate. For Passage 1 and 5, the impeller and volute tongue interaction is weak and the wake flow continues to present as the impeller rotates.

After comparing the velocity profile at different flow rates, it is suggested that velocity profile near impeller exit is strongly coupled with impeller volute tongue interaction. The velocity profile at each flow rates near impeller exit also strongly depends on the jet wake flow pattern developed inside the passage. At $0.7Q_{design}$, impeller exit flow shows a highly distorted velocity profile as compared to Q_{design} and $1.3Q_{design}$.

6.2 Distorted Impeller Exit Flow

The previous section highlighted the strong impeller volute interaction near volute tongue region. It is found that only impeller Passage 6 wake flow development is coupled with the impeller rotation and volute tongue while the adjacent passages are not affected. In this section, the impeller exit flow is studied in detail and to

further understand the flow unsteadiness in circumferential direction by using the velocity components.

The flow discharge from the impeller can be resolved into axial, radial and circumferential components. Only the radial velocity component is in interest in this case. Figure 6-4 to Figure 6-12 show a series of instantaneous radial velocity coefficient V_r/U_2 at different flow rates and three different locations namely bottom, mid and top plane across the impeller exit at z/b_2=0.10, 0.50 and 0.90. The radial velocity extracted at circumferential location which is at R/R2=0.97, 1.00, 1.02 and 1.04 respectively at each plane. 0.97R2 plane is inside the impeller passage while 1.04R2 is outside the impeller and at the tip of volute tongue. In these figures, abscissa is the angular position of passage 1, 5 and 6 measured from a plane X-X between Plane V and VI as shown in Figure 2-2. Ordinate is the non-dimensional radial velocity coefficient V_r/U_2. A positive V_r/U_2 represents a net outflow and a negative V_r/U_2 represents a deficit outflow. The amount of flow reversal is referred to original V_r/U_2 that is 24 ° away from Blade 1 suction side in angular direction when trailing edge is aligned with volute tongue at 0 °. At 0 ° degree blade rotation, the impeller blade trailing edge is aligned with the volute tongue as shown in Figure 2-2. When the impeller rotates 12 °, 24 °, 26 ° and 48 °, the volute tongue will be at different position between the suction side (S.S) of Blade 1 and pressure side (P.S) of Blade 6.

Figure 6-4 to Figure 6-6, (a)-(e), show how V_r/U_2 is changing at top, mid and bottom planes at $0.7Q_{design}$ when the impeller rotates. On the top plane near impeller shroud as in Figure 6-4 (a), when the impeller trailing edge is aligned with the volute tongue, V_r/U_2 increases monotonically from suction to pressure side within blade-to-blade Passage 6.

When the impeller blade rotates and the trailing edge misaligned with volute tongue, the flow discharge from impeller Passage 6 is partially blocked and reversed due to the confined space near tip of volute tongue. From 12 ° to 48 ° blade rotation, minimum value of non-dimensional V_r/U_2 at 1.04R2 is negative which represent a deficit outflow and flow reversal at that point. The flow reversal of V_r/U_2 near volute tongue region occurs from 0.97R2 to 1.02 R2 as well. This suggested that the flow reversal is reflected from outside the impeller back into the impeller passage. The flow reversal not only occurs locally at the blade meeting point of trailing edge and volute tongue, but also around the trailing edge as well. This is because there is a negative and positive velocity gradient before and after the volute tongue position. Another observation between 24 ° to 48 ° blade rotation is that there is a V_r/U_2 hump formed between the suction side and volute tongue interaction point. A rapid increase of V_r/U_2 and steeper radial velocity gradient means that more flow is forced through this area.

At the mid plane of impeller exit, Figure 6-5 (a)-(e) show that V_r/U_2 has a similar interaction pattern at top plane. The V_r/U_2 increases monotonically from suction side to pressure side but with a less steep velocity gradient at 0 ° blade rotation. The velocity gradient at passage 6 can be linked to Figure 6-1 where the wake flow is concentrated on the suction side as compared to the top plane. As the impeller rotates, on the suction side of Blade 1 the V_r/U_2 has a lower peak value than the top plane. This represents the velocity profile in Figure 6-1 where the low flow region is spanning across the mid plane. The higher V_r/U_2 value on the suction side is only observed after volute tongue is half passed the impeller passage in rotation direction, at blade rotation 36 ° to 48 °. The minimum value of V_r/U_2 is -0.10 at mid plane is

lower than -0.05 at top plane at 24 °blade rotation which means that the flow reversal at mid plane is strongly coupled with volute tongue interaction.

However, at bottom plane near hub in Figure 6-6 (a) a flow reversal occurred even before the impeller volute interaction at $0.7Q_{design}$. At 0 °, the V_r/U_2 values are negative from 0.97R2 to 1.04R2, ranging from -0.04 to 0. This means that the wake flow is reversing into impeller passage due to lack of momentum as shown in Figure 6-1. When the impeller is rotated by 24° and 36° where the volute tongue is half passed the impeller passage, the flow reversal near the volute tongue region reached maximum amplitude, with V_r/U_2 more than -0.20. In these positions, the impeller volute tongue interaction is strongly affecting the flow field within or outside the impeller. The flow reversal V_r/U_2 is almost synchronised where V_r/U_2 at 0.97R2 and 1.04R2 are reversed at the same velocity gradient. When the impeller reaches the blade rotation of 48 °, the V_r/U_2 is still remained negative over wide area in the passage. It is also observed that there is very steep velocity gradient on the near the blade pressure side and suction sides.

With the combination from Figure 6-4 to Figure 6-6 , the complete picture of the distorted outflow profile at impeller exit can be mapped out as seen in Figure 6-1 of the jet/wake flow profile. Based on the top, mid and bottom plane profile, the largest flow reversal of V_r/U_2 always occurs when the volute tongue is half passed the impeller exit at 24 °or 36 °rotation. The maximum flow reversal V_r/U_2 is about 140%, 260% and 220% at 1.04R2.

Figure 6-7, Figure 6-8 and Figure 6-9 respectively show the V_r/U_2 at top, mid and bottom at Q_{design}. The velocity profiles at these three different locations are similar to $0.7Q_{design}$ where the radial velocity increases from suction to pressure side but with

different velocity gradient. In Figure 6-7, the top plane impeller volute interaction is significantly lower as compared to the top plane at $0.7Q_{design}$. The flow reversal V_r/U_2 at 1.04R2 is less than 70% as compared to 140% at $0.7Q_{design}$ at 24° rotation. Another observation is that the flow reversal is localised as well. In this case, the flow reversal only affected the V_r/U_2 at the interaction point between the impeller trailing edge and volute tongue, but will not create a wide "V"-shape flow reversal as seen in Figure 6-4 to Figure 6-6. From blade rotation 12° to 24°, the velocity gradient from suction to pressure side within Passage 6 is maintained even the flow reversal is occurred at the impeller volute tongue interaction point. As the impeller continues to rotate from 36° to 48°, a hump emerged before the flow reversal of V_r/U_2 due to volute tongue interaction. At top plane, there is no deficit outflow, or negative V_r/U_2 is observed throughout the impeller rotation.

At mid plane, Figure 6-8, a different trend from top plane is observed. The velocity gradient is steeper that top plane because of the wake core or low flow profile as shown in Figure 6-2. Due to the steep velocity gradient, the flow reversal of V_r/U_2 at 24° is only about 110% as compared to 200% at $0.7Q_{design}$ at 1.04R2. From blade rotation 36° to 48°, the V_r/U_2 on the pressure side is not affected by the impeller volute tongue interaction.

At bottom plane, Figure 6-9, there is no flow reversal when the blade tailing edge is aligned with the volute tongue. This is in contrast to $0.7Q_{design}$, where V_r/U_2 is negative even at 0° blade rotation. The V_r/U_2 is rather flat with on the suction and pressure sides when the trailing edge is aligned with volute tongue. As the impeller rotates to 24°, the V_r/U_2 flow reversal is only about 75% which is comparable to top plane.

Figure 6-10 to Figure 6-12 show the V_r/U_2 at top, mid and bottom planes at $1.3Q_{design}$. When the blade trailing edge is aligned with volute tongue at 0°, Figure 6-10 shows that the V_r/U_2 profile is a "S"-shape with low V_r/U_2 value from suction to pressure side. This is same as the profile as seen in Figure 6-3, where high velocity jet zone is occurring near shroud pressure side while low velocity wake flow zone is near shroud suction corner. As the impeller rotates from 12° to 48°, there is only less than 35% V_r/U_2 reversal as compared to other flow rates. However, there is very steep velocity gradient from the suction towards pressure side. The reason is because at high flow rate, the wake flow shedding from impeller exit is carrying a relatively high momentum that prevent from any flow reversal to occur when volute tongue moves deep into the passage.

At the mid plane, Figure 6-11, a similar impeller volute tongue interaction is observed. At 0° blade rotation, there is a relatively flat V_r/U_2 profile, which means that the outflow from impeller exit is very uniform. From 12° to 48° blade rotation, the flow reversal V_r/U_2 is relatively low and no deficit outflow observed. However, there is a steep velocity gradient right behind the impeller tongue volute interaction, the V_r/U_2 rises rapidly towards the pressure side.

At the bottom plane, Figure 6-12, an inverse "S-"shape of V_r/U_2 profile is observed. As compared to Figure 6-10 at top plane, the peak of V_r/U_2 is on the suction side rather than the pressure side. From blade rotation 0° to 48°, there is no flow reversal V_r/U_2 is observed. Only the V_r/U_2 at 1.04R2 is weakly affected by the impeller volute interaction starting from blade rotation 24° to 48°.This suggested that the impeller volute tongue interaction is not reflected upstream as seen at other flow rates and different plane.

After analyzing V_r/U_2 profile for different flow rates, at top, mid and bottom planes, it is noticed that Passage 1 and 5 are not affected by this impeller volute tongue interactions. Another observation is that the flow reversal V_r/U_2 on the suction side is flow rates dependent as well. At mid plane as shown in Figure 6-5, Figure 6-8 and Figure 6-11, the flow reversal V_r/U_2 at $0.7Q_{design}$ on the suction at is more than Q_{design} and $1.4Q_{design}$. At $0.7Q_{design}$ the V_r/U_2 at 12 ° from suction side in angular direction is only 0.05 before the interaction. After 36 ° rotation, the same location V_r/U_2 rises to 0.15 represents a 300% increase. Similarly, the V_r/U_2 at Q_{design} before rotation is only 0.09. After rotation, the V_r/U_2 rises to 0.12. However, at $1.3Q_{design}$ the flow reversal V_r/U_2 is very weak. Based on this observation it is suggested that the flow reversal V_r/U_2 is depends on the momentum of fluid carry at different flow rates.

This section gives an overview of how the impeller volute interaction at three different flow rates is affecting the flow within and outside the impeller. In general, as the impeller rotates and volute tongue moves into impeller passage in direction of rotation, a flow reversal V_r/U_2 is observed over that volute tongue region.

6.3 Pressure Pulsations

Figure 6-13 to Figure 6-15 shows the temporal and spatial static pressure distribution near volute tongue at different angular location blade trailing edge relative to volute tongue. The impeller is rotating in anti-clockwise direction.

At $0.7Q_{design}$ as in Figure 6-13, as the impeller rotates from -12 ° to 0 °, the pressure contour lines are extending from the volute tongue onto the pressure side of the blade. The stagnation pressure point is on the pressure side of the volute tongue. However, there is a localised high pressure spot on the pressure side blade trailing. This localised pressure spot is the fluid flow over the sharp edge corner that caused a

sudden pressure jump. As the impeller rotates from 6 ° to 18 °, there is a pressure core shedding near the trailing edge. This localised pressure core is due to wake flow recirculation on the suction side volute tongue as shown in Figure 5-16 (a).

Figure 6-14 shows that the isobar contours within the blade-to-blade overlap region are parallel and perpendicular to the blade pressure and suction sides at Q_{design}. This is in good theoretical agreement where the pressure is increase in stream wise direction within the impeller passage. However, after the blade-to-blade overlap region, or so called the "throat" area, the isobar lines are distorted. The distorted isobar lines are the evidence of the instantaneous fluctuation pressure at the impeller periphery as seen in Figure 4-6. The stagnation point is on the tip of volute tongue. This is in good agreement with Figure 5-16 (b) where flow incidence angle is zero at Q_{design}.

As the impeller rotating in anti-clockwise direction, from -12 ° to +18 ° the distorted isobar lines are fluctuating around the impeller periphery line. These localized pressure fluctuation is affecting the global pump delivery head as well. As in Figure 4-6 the pump delivery head is dependent on the location of the impeller trailing edge relative position with the volute tongue. The trailing edge and volute tongue have a localized high pressure envelop is due to the stagnation pressure point as well. However, as compared to $0.7Q_{design}$, there is no pressure core shedding on the blade trailing edge is observed.

Figure 6-15 shows the pressure contours at $1.3Q_{design}$ as the impeller rotates from -12 ° to 18 °. The stagnation pressure point is on the suction side of the volute tongue and there is two localised pressure spot on the trailing. One is on the pressure side and other one is on the suction side. As explained earlier, these localised pressure spot is

due to the fluid flow over the sharp edge corner at the trailing edge. As compared to $0.7Q_{design}$, the high pressure core emerges after impeller rotated from 6° to 18°. This emergence of the high pressure core is due to the blockage of fluid flow from impeller exit at high flow rate. The proximity of the volute tongue and the impeller trailing edge is preventing the fluid flow from the impeller to enter the volute casing smoothly due to positive flow angle and main flow blocking as shown in Figure 5-16 (c).

Based on the series of pressure contours plot with impeller rotating from -12° to +18°, the impeller volute tongue interaction is truly depends on the relative location of the blade trailing edge as well as the flow rate.

6.4 Concluding Remarks

This chapter highlighted the dynamics of the impeller volute tongue interaction at different flow rates and relative blade trailing edge position against the volute tongue.

The jet wake flow pattern and wake flow shedding and impingement is successful captured at the impeller exit by the simulation. The jet-wake flow occurs within the impeller passage and its formation is due to the pronounced high velocity exit flow pattern that coupled with low velocity reversed flow. However, the jet wake flow near impeller exit is flow rate dependent because its formation is much depends on the upstream flow structures near impeller inlet and leading edge.

At $0.7Q_{design}$, the wake flow shedding strongly affected by the volute tongue position. The wake flow core breaks up when the volute moved pass the impeller passage due to high blade passing frequency and low wake flow momentum. However, at Q_{design} and $1.3Q_{design}$, the wake flow shedding is weakly coupled with

impeller volute tongue interaction. The wake flow core is diffused slowly as volute tongue moved passed the impeller passage.

The analysis of impeller volute tongue interaction by resolving the impeller exit flow velocity into individual components shows how the flow within the impeller passage near impeller exit responding to impeller rotation. The non-dimensional velocity ratio of V_r/U_2 shows that flow reversal occurs as the volute tongue moved passed the impeller passage.

The flow reversal is flow rate and position dependent as well. On the top plane at impeller passage, at $0.7Q_{design}$, the V_r/U_2 dip and recovery is strong as compared to Q_{design} and $1.3Q_{design}$. This because at $0.7Q_{design}$ with lower fluid momentum, the flow reversal is more sensitive as compared to high momentum flow at Q_{design} and $1.3Q_{design}$. At mid plane, only the 1.3Qdesign shows less V_r/U_2 dip as compared to Q_{design} and $0.7Q_{design}$. The V_r/U_2 dip at $1.3Q_{design}$ is about 30% as compared to 75% at Q_{design} and 150% at 24° rotation. At bottom plane, the flow reversal at 0.7Qdesign is highest, about 200% as compared to Q_{design} and $1.3Q_{design}$ at 24° rotation. Again, at $1.3Q_{design}$, the flow reversal is not affected by the volute tongue passing.

Based on the static pressure distribution around volute casing at different flow rates and time history of pressure pulsation near trailing edge and volute tongue, it can be concluded that pressure fluctuations caused by the interaction between the blades and tongue of the volute casing, was reflected upstream to the impeller exit. The level and amplitude of the pressure fluctuations within the impeller passage grows and decays in magnitude as the trailing edge is aligned or away from the volute tongue.

The pressure fluctuations can be observed from the non-uniform and fluctuating isobar pressure contour near impeller. At $0.7Q_{design}$ and $1.3Q_{design}$, there are pressure

cores shedding near impeller trailing edge due to the flow recirculation and blockage as well.

From the analysis of the unsteady and dynamic impeller volute tongue interaction, it can be concluded that flow field near impeller is strongly coupled with flow rate and relative position of volute tongue against the impeller trailing.

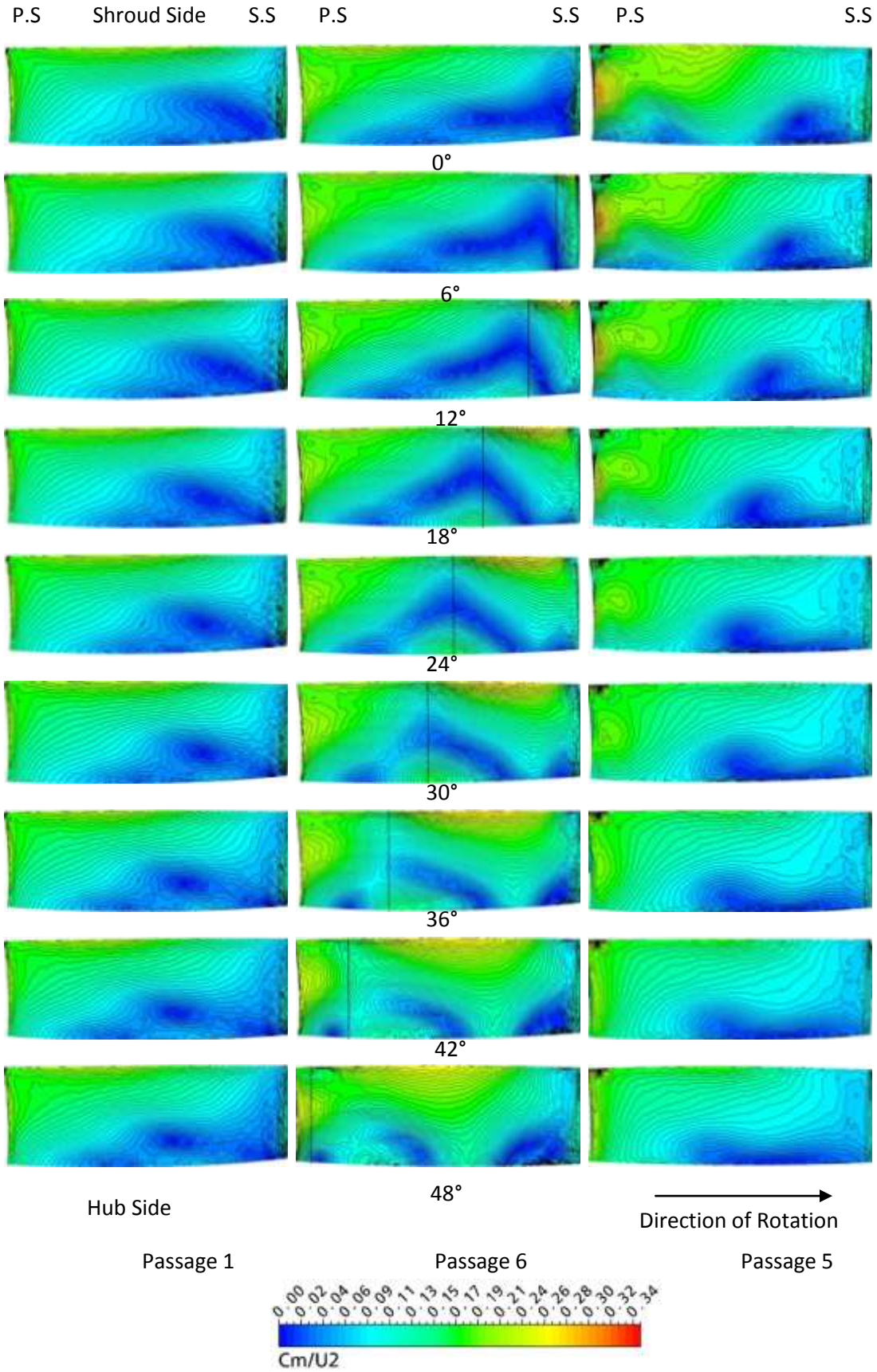

Figure 6-1 Distorted velocity profile near impeller exit at $0.7Q_{design}$.

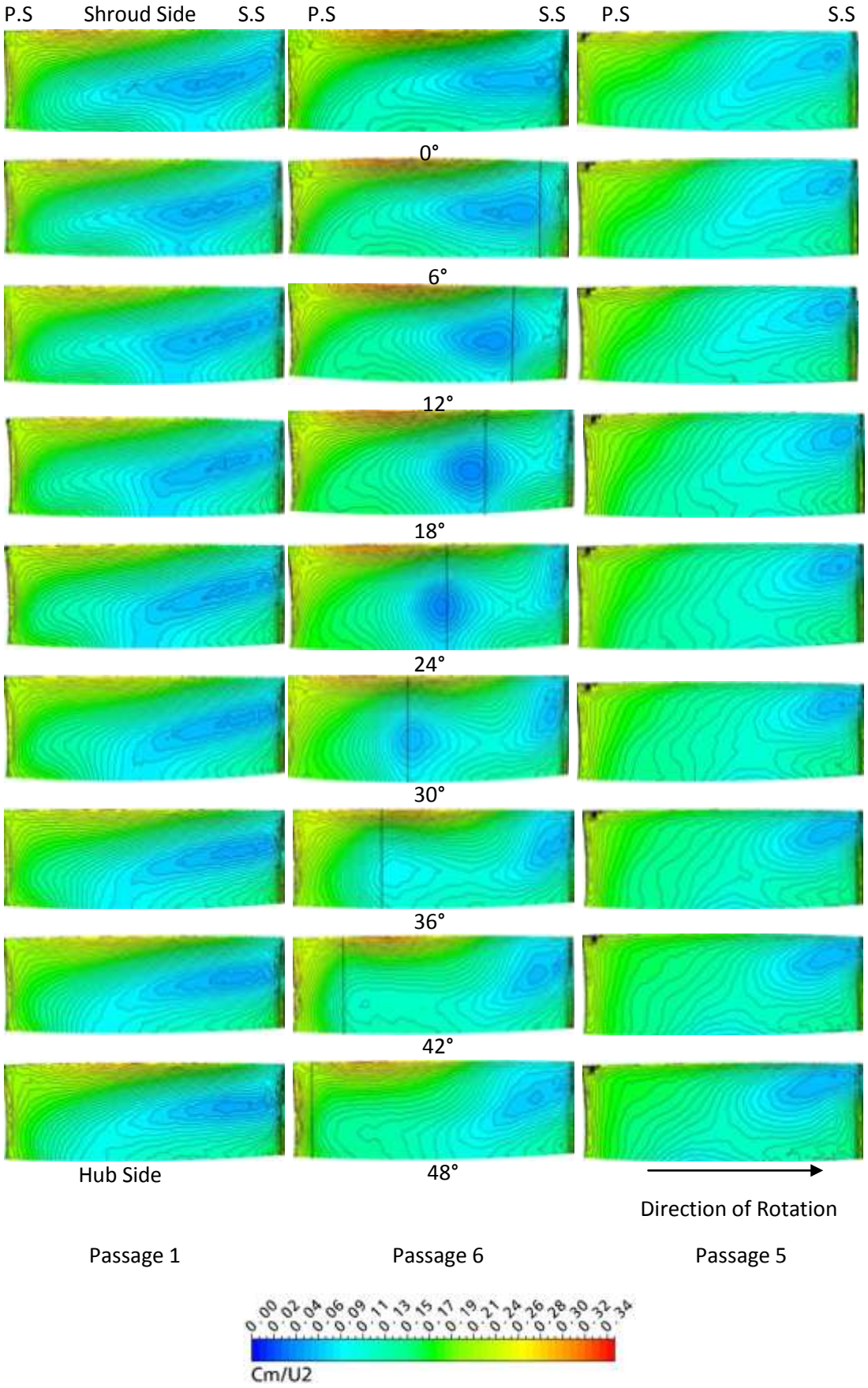

Figure 6-2 Distorted velocity profile near impeller exit at Q_{design} .

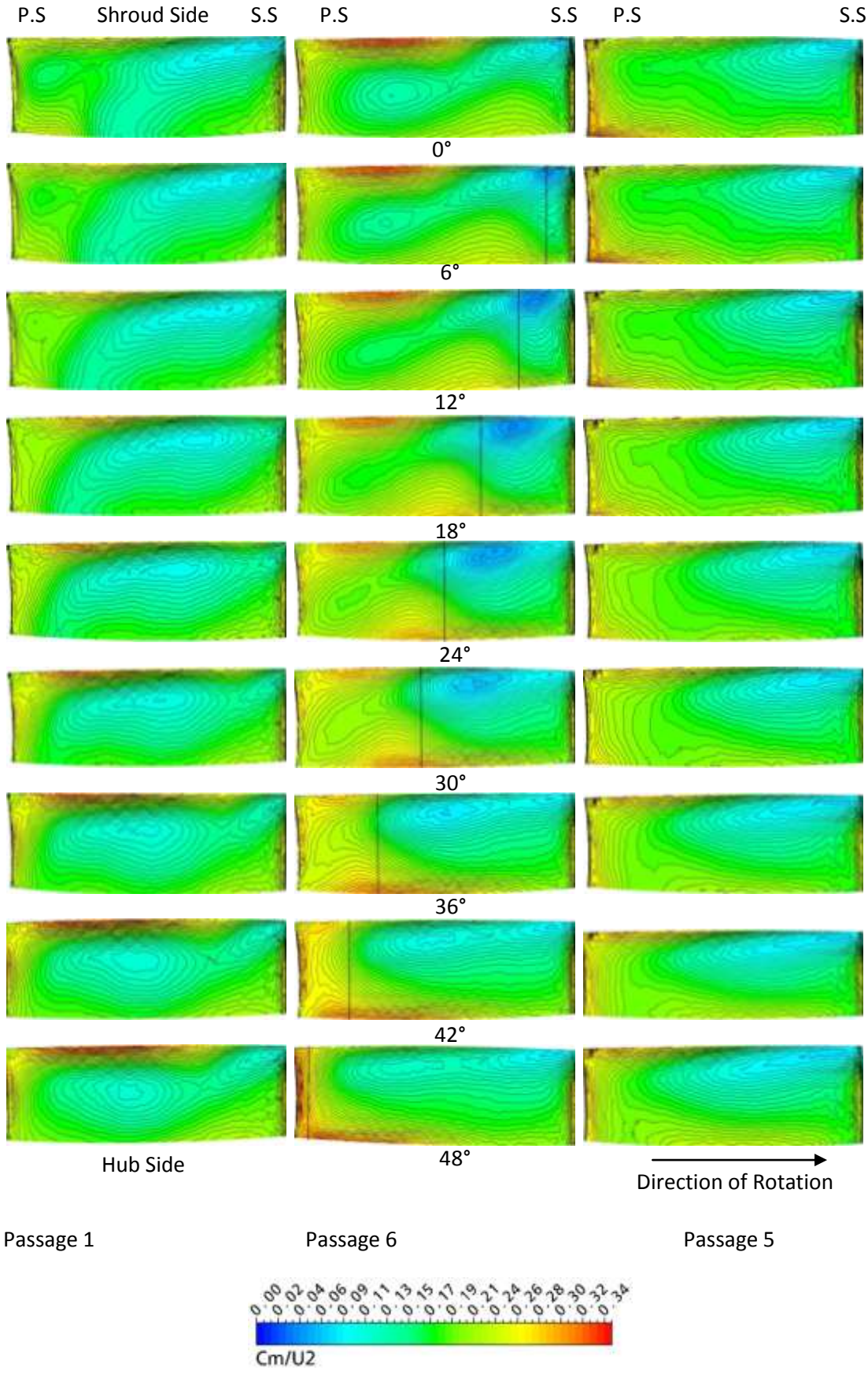

Figure 6-3 Distorted velocity profile near impeller exit at $1.3Q_{design}$.

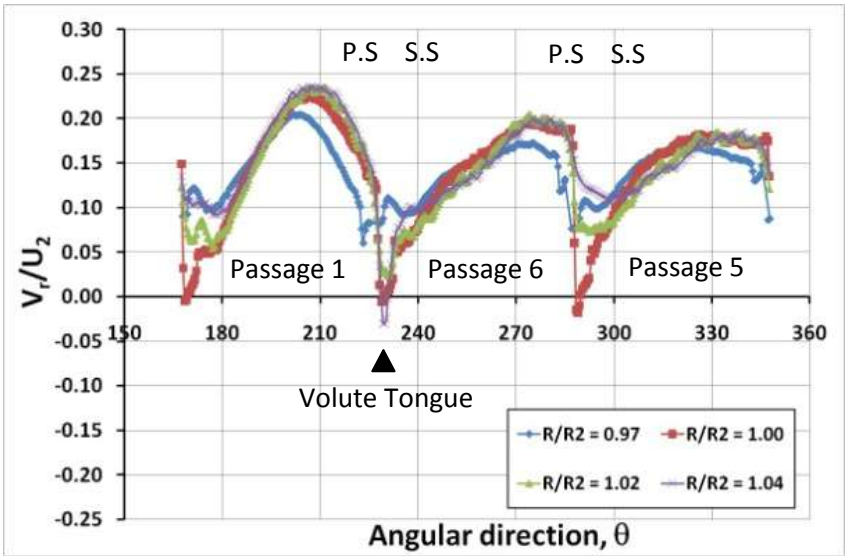
P.S S.S
P.S S.S
Passage 1
Passage 6
Passage 5
Volute Tongue
R/R2 = 0.97
R/R2 = 1.00
R/R2 = 1.02
R/R2 = 1.04
Angular direction, θ
V_r/U_2

(a) 0 °

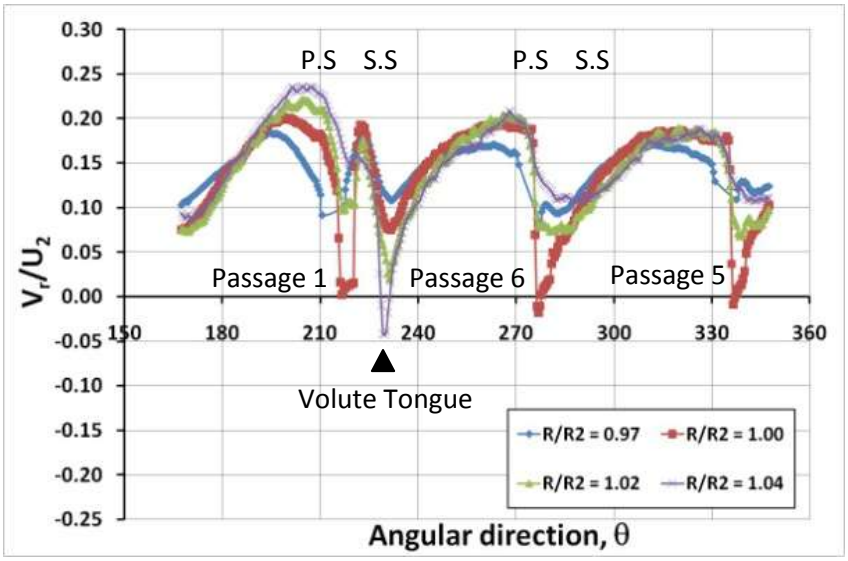
P.S S.S
P.S S.S
Passage 1
Passage 6
Passage 5
Volute Tongue
R/R2 = 0.97
R/R2 = 1.00
R/R2 = 1.02
R/R2 = 1.04
Angular direction, θ
V_r/U_2

(b) 12 °

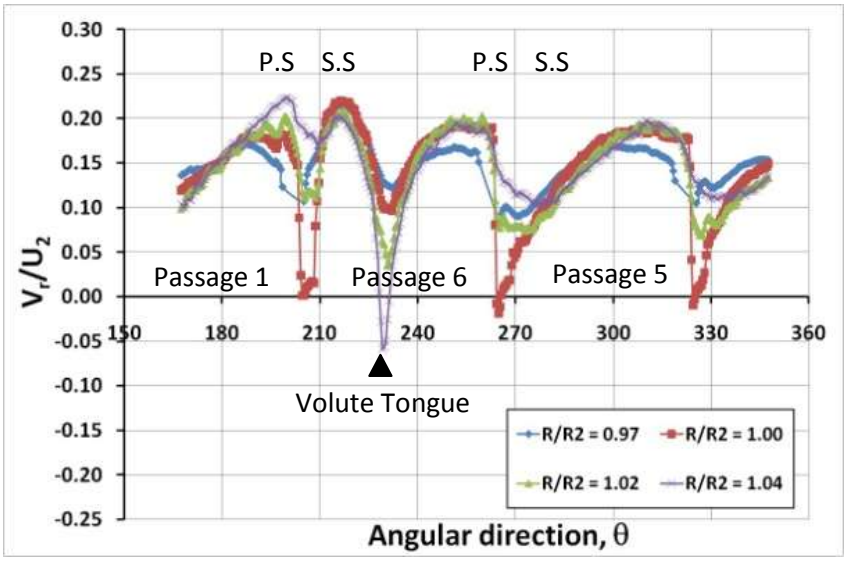
P.S S.S
P.S S.S
Passage 1
Passage 6
Passage 5
Volute Tongue
R/R2 = 0.97
R/R2 = 1.00
R/R2 = 1.02
R/R2 = 1.04
Angular direction, θ
V_r/U_2

(c) 24 °

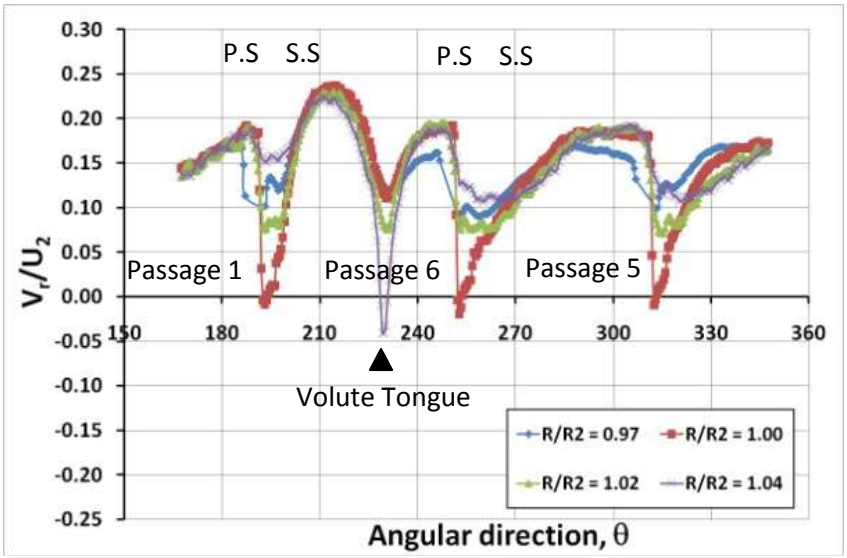

(d) 36 °

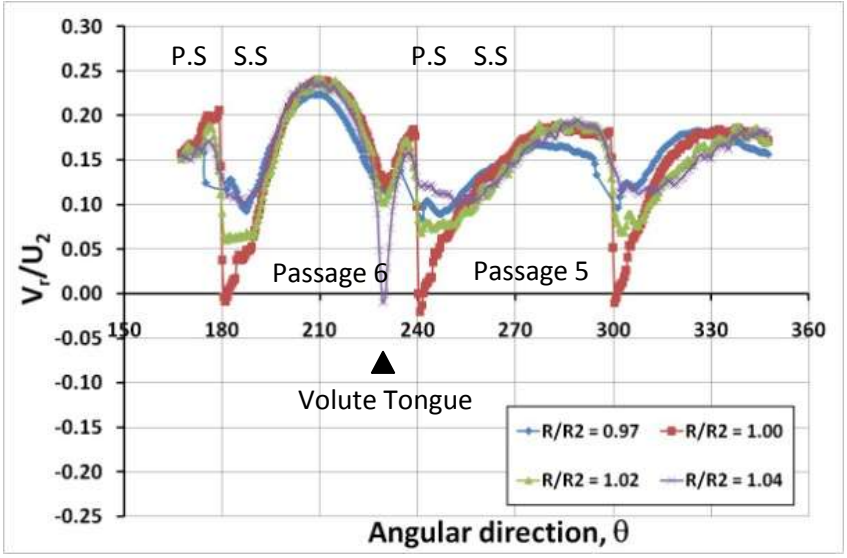

(e) 48°

Figure 6-4 Top Plane radial velocity coefficient V_r/U_2 at $0.7Q_{design}$.

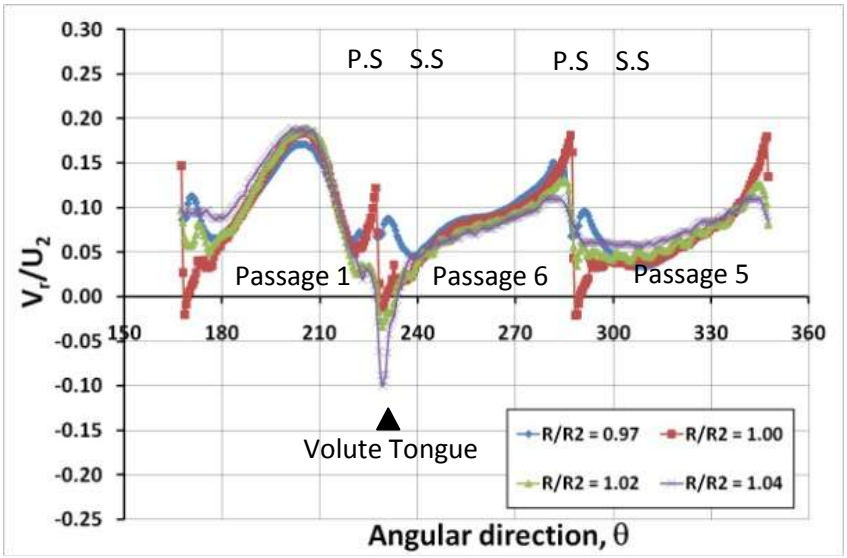
P.S S.S P.S S.S
Passage 1
Passage 6
Passage 5
Volute Tongue
R/R2 = 0.97
R/R2 = 1.00
R/R2 = 1.02
R/R2 = 1.04
Angular direction, θ
V_r/U_2

(a) 0 °

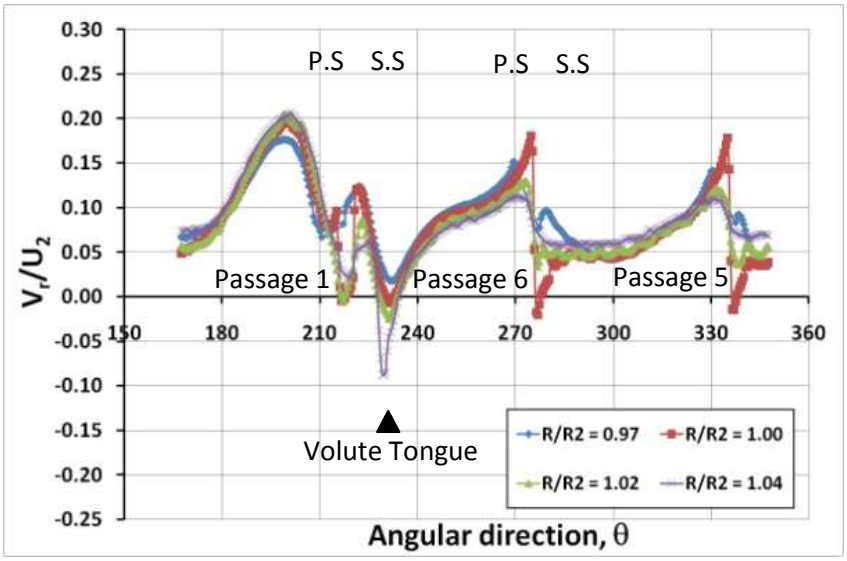
P.S S.S P.S S.S
Passage 1
Passage 6
Passage 5
Volute Tongue
R/R2 = 0.97
R/R2 = 1.00
R/R2 = 1.02
R/R2 = 1.04
Angular direction, θ
V_r/U_2

(b) 12 °

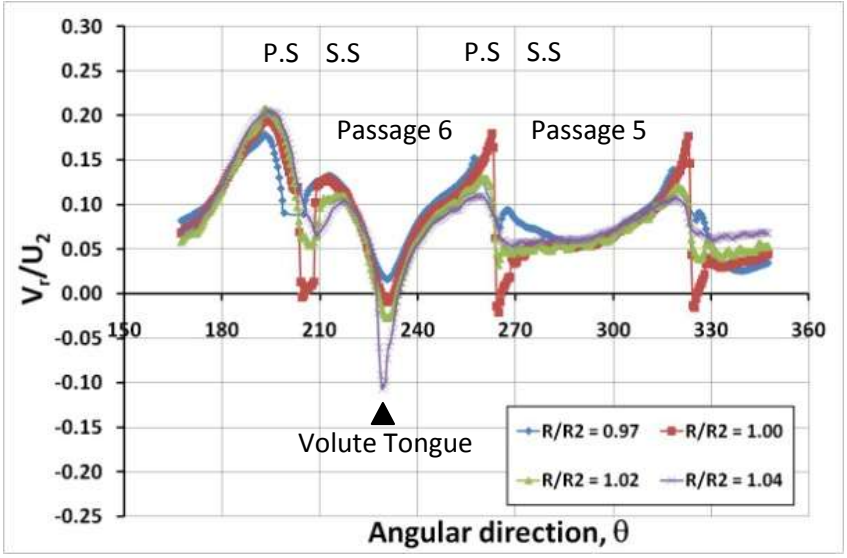
P.S S.S P.S S.S
Passage 6
Passage 5
Volute Tongue
R/R2 = 0.97
R/R2 = 1.00
R/R2 = 1.02
R/R2 = 1.04
Angular direction, θ
V_r/U_2

(c) 24 °

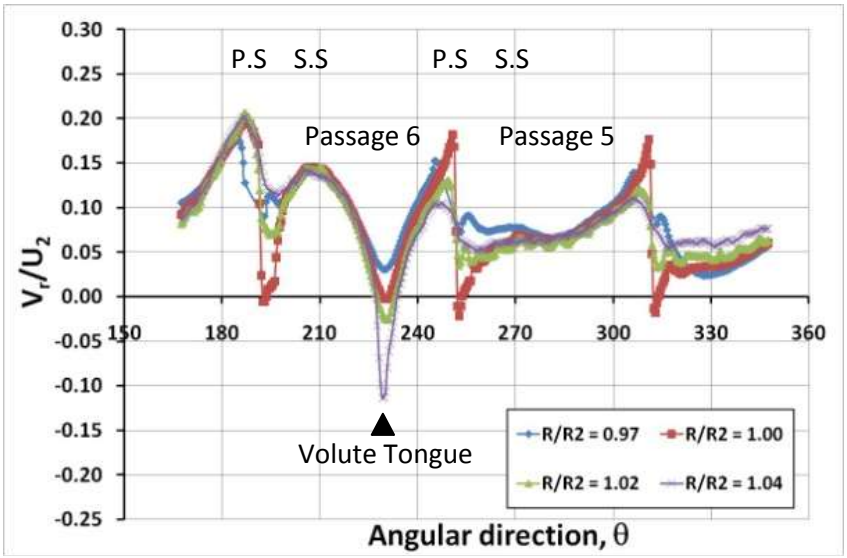

(d) 36 °

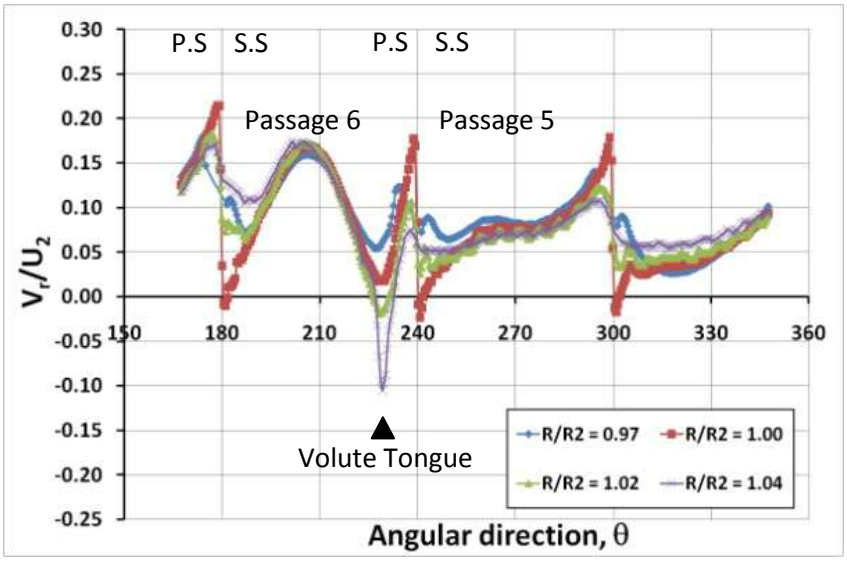

(e) 48°

Figure 6-5 Mid Plane radial velocity coefficient V_r/U_2 at $0.7Q_{design}$.

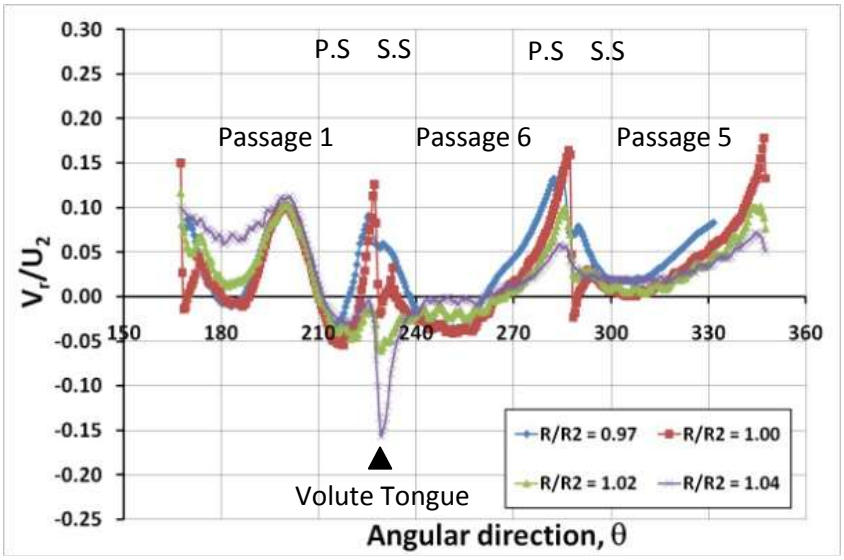
P.S S.S
P.S S.S
Passage 1
Passage 6
Passage 5
V_r/U_2
Volute Tongue
Angular direction, θ
R/R2 = 0.97
R/R2 = 1.00
R/R2 = 1.02
R/R2 = 1.04

(a) 0 °

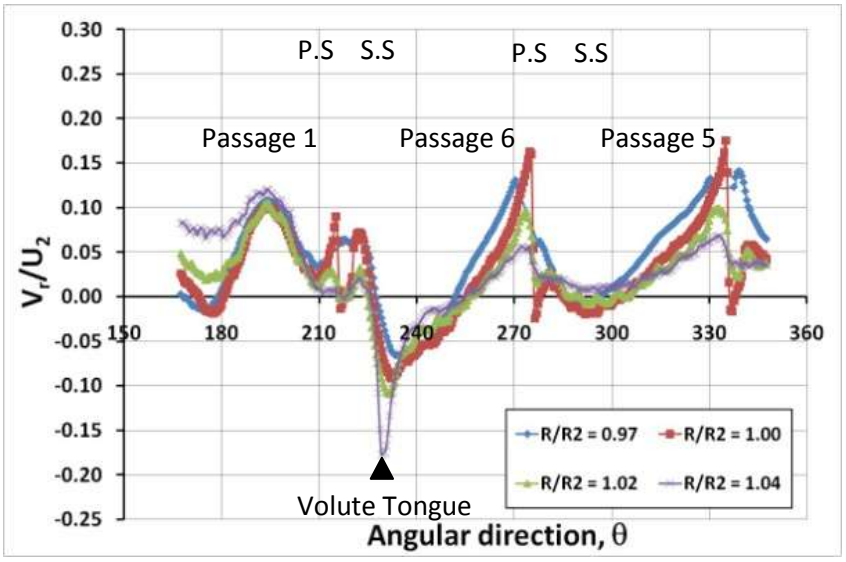
P.S S.S
P.S S.S
Passage 1
Passage 6
Passage 5
V_r/U_2
Volute Tongue
Angular direction, θ
R/R2 = 0.97
R/R2 = 1.00
R/R2 = 1.02
R/R2 = 1.04

(b) 12 °

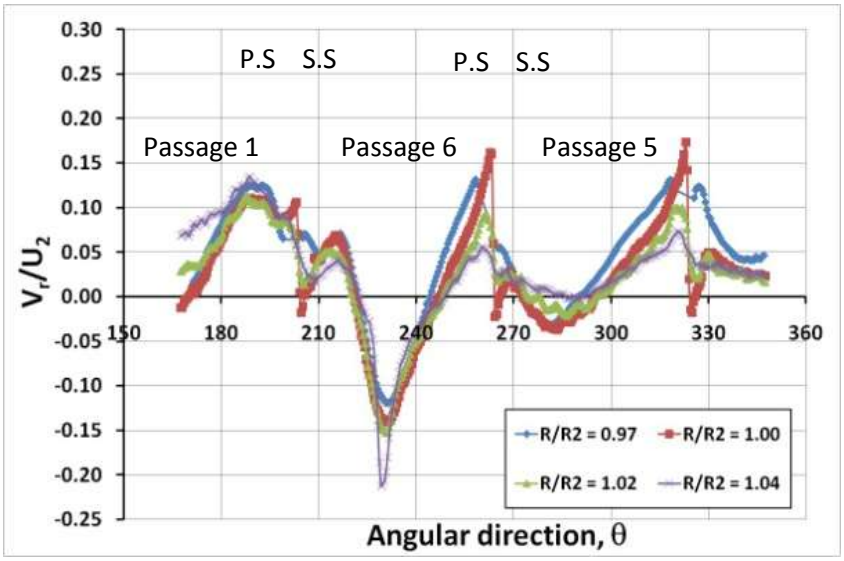
P.S S.S
P.S S.S
Passage 1
Passage 6
Passage 5
V_r/U_2
Angular direction, θ
R/R2 = 0.97
R/R2 = 1.00
R/R2 = 1.02
R/R2 = 1.04

(c) 24 °

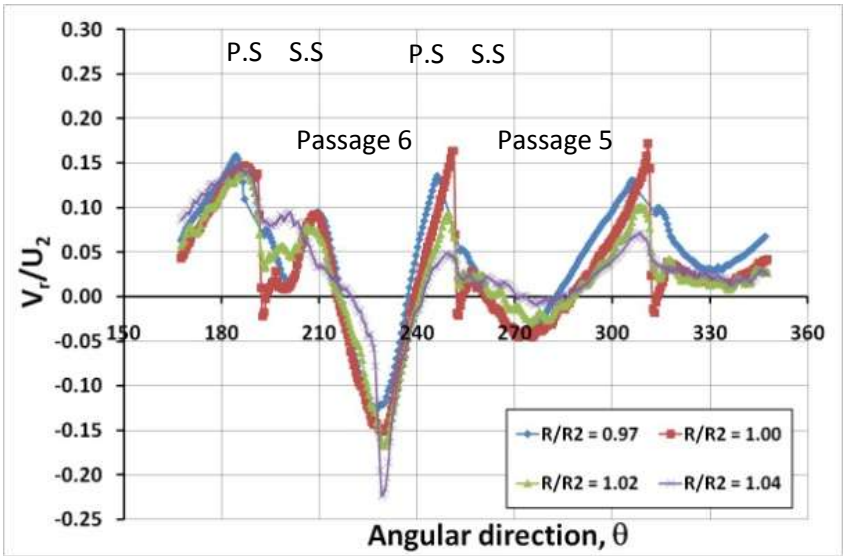

(d) 36 °

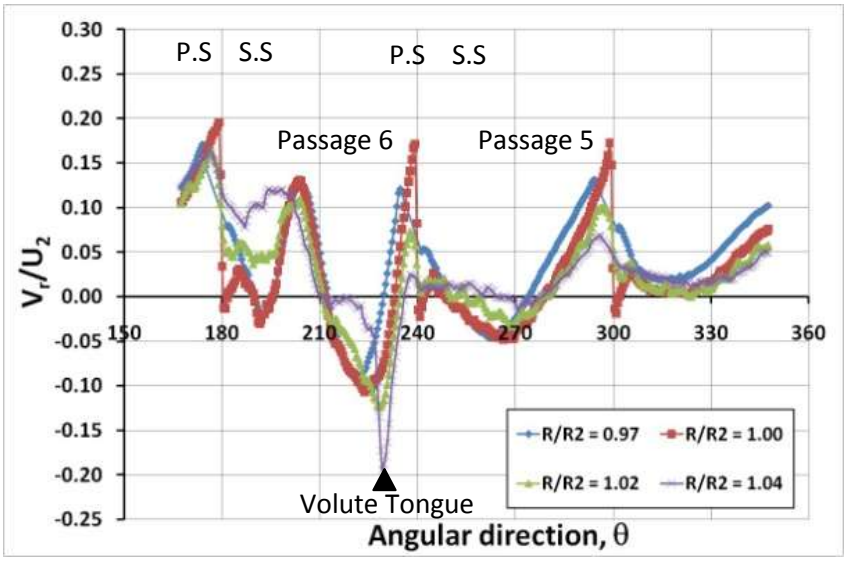

(e) 48°

Figure 6-6 Bottom Plane radial velocity coefficient V_r/U_2 at $0.7Q_{design}$.

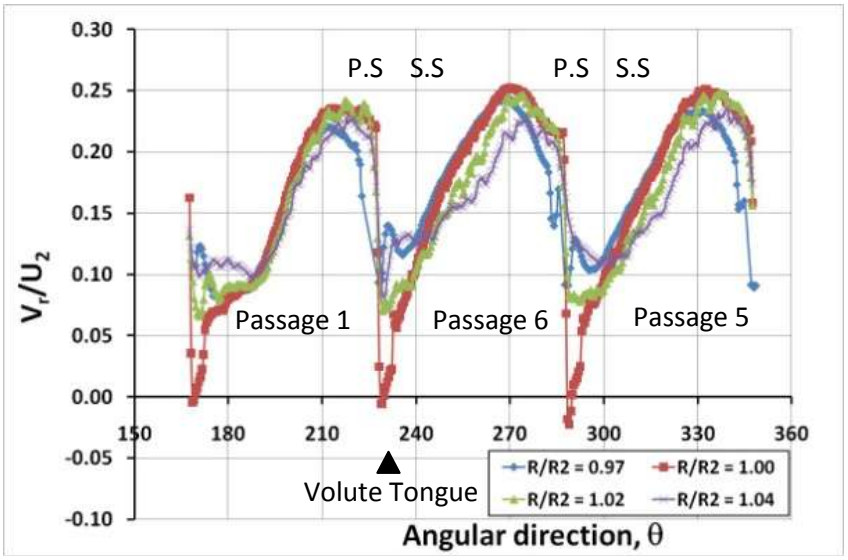
P.S S.S P.S S.S
Passage 1
Passage 6
Passage 5
Volute Tongue
R/R2 = 0.97
R/R2 = 1.00
R/R2 = 1.02
R/R2 = 1.04
Vr/U2
Angular direction, θ

(a) 0 °

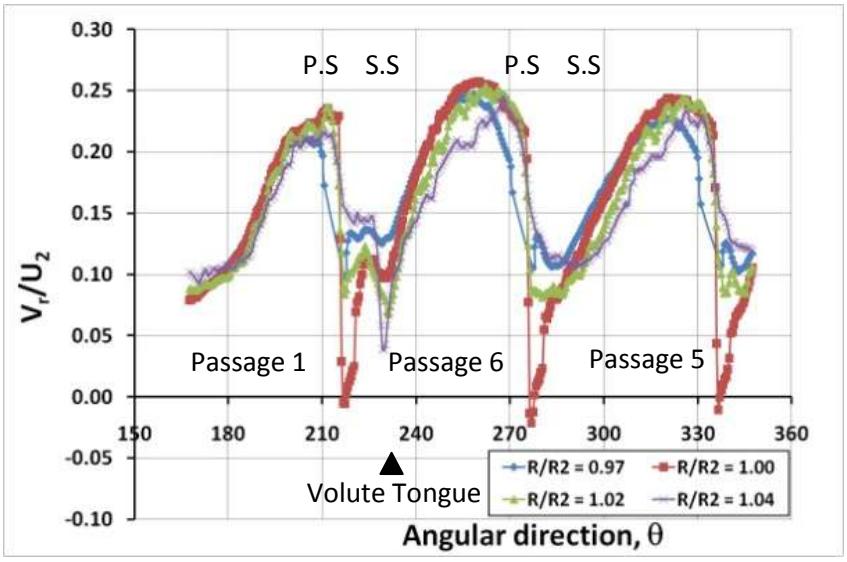
P.S S.S P.S S.S
Passage 1
Passage 6
Passage 5
Volute Tongue
R/R2 = 0.97
R/R2 = 1.00
R/R2 = 1.02
R/R2 = 1.04
Vr/U2
Angular direction, θ

(b) 12 °

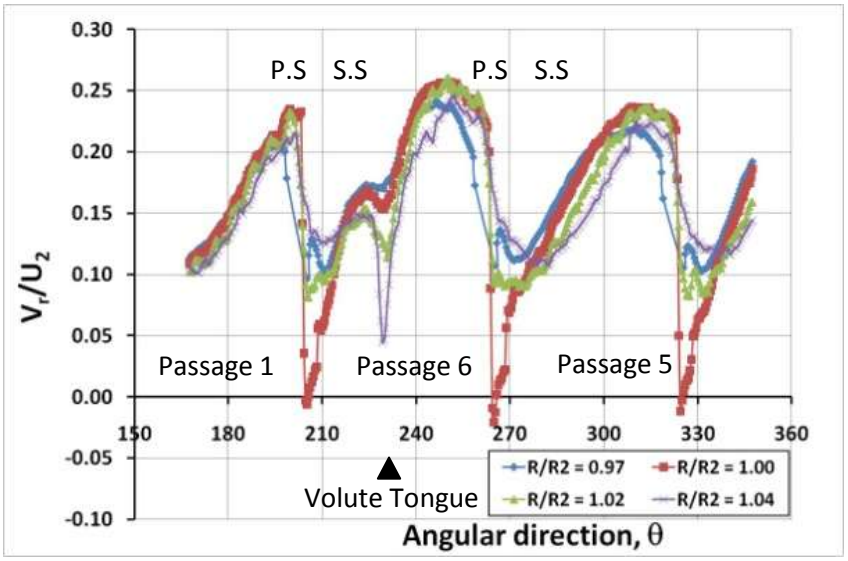
P.S S.S P.S S.S
Passage 1
Passage 6
Passage 5
Volute Tongue
R/R2 = 0.97
R/R2 = 1.00
R/R2 = 1.02
R/R2 = 1.04
Vr/U2
Angular direction, θ

(c) 24 °

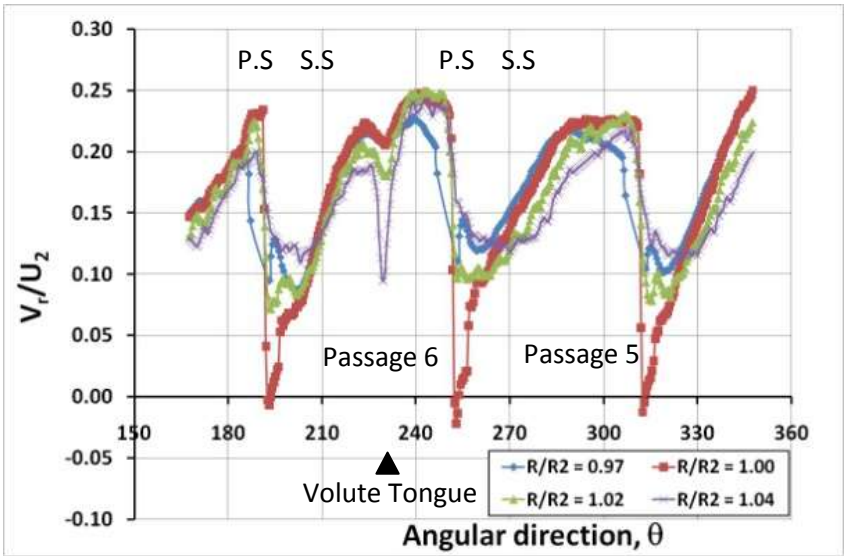

(d) 36 °

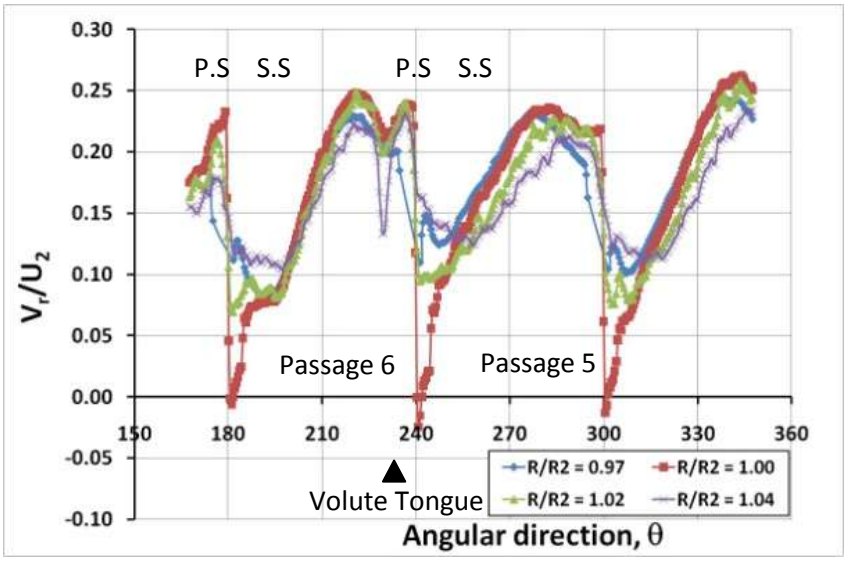

(e) 48°

Figure 6-7 Top Plane radial velocity coefficient V_r/U_2 at Q_{design} .

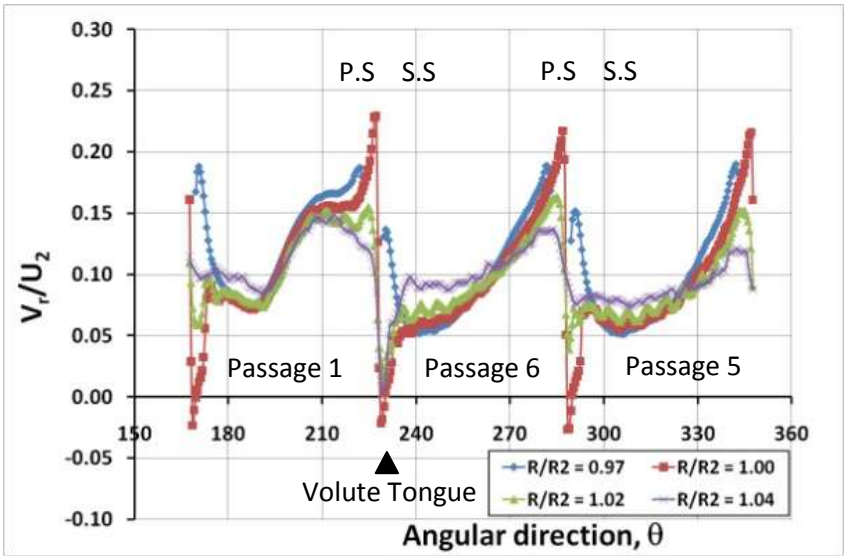
P.S S.S P.S S.S
Passage 1
Passage 6
Passage 5
Volute Tongue
R/R2 = 0.97
R/R2 = 1.00
R/R2 = 1.02
R/R2 = 1.04
Vr/U2
Angular direction, θ

(a) 0 °

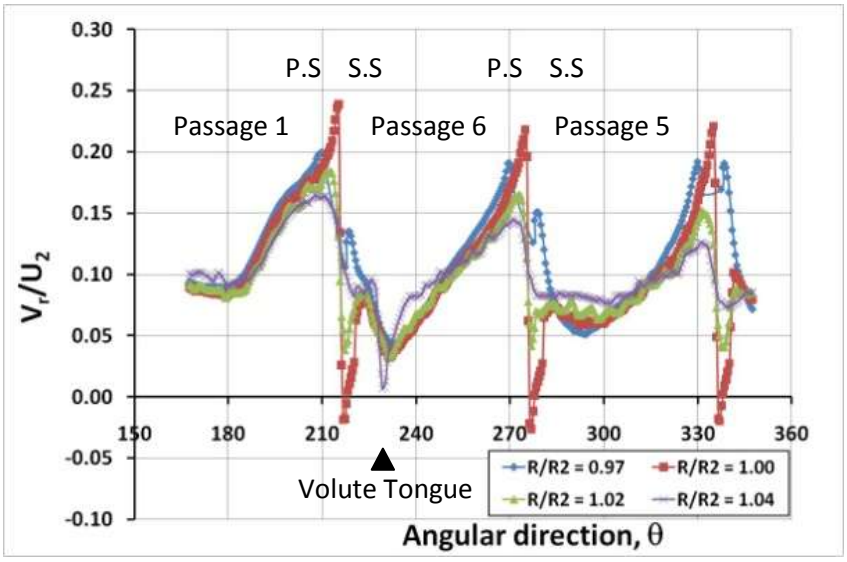
P.S S.S P.S S.S
Passage 1
Passage 6
Passage 5
Volute Tongue
R/R2 = 0.97
R/R2 = 1.00
R/R2 = 1.02
R/R2 = 1.04
Vr/U2
Angular direction, θ

(b) 12 °

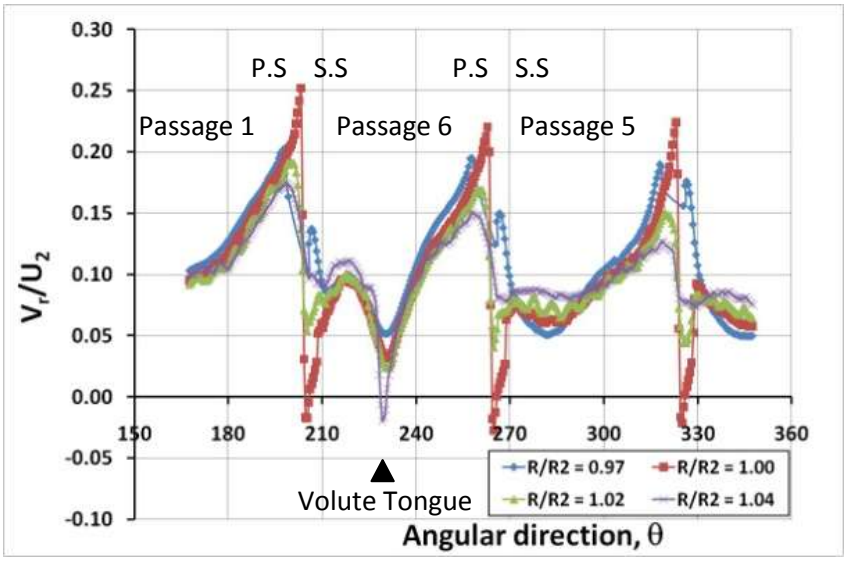
P.S S.S P.S S.S
Passage 1
Passage 6
Passage 5
Volute Tongue
R/R2 = 0.97
R/R2 = 1.00
R/R2 = 1.02
R/R2 = 1.04
Vr/U2
Angular direction, θ

(c) 24 °

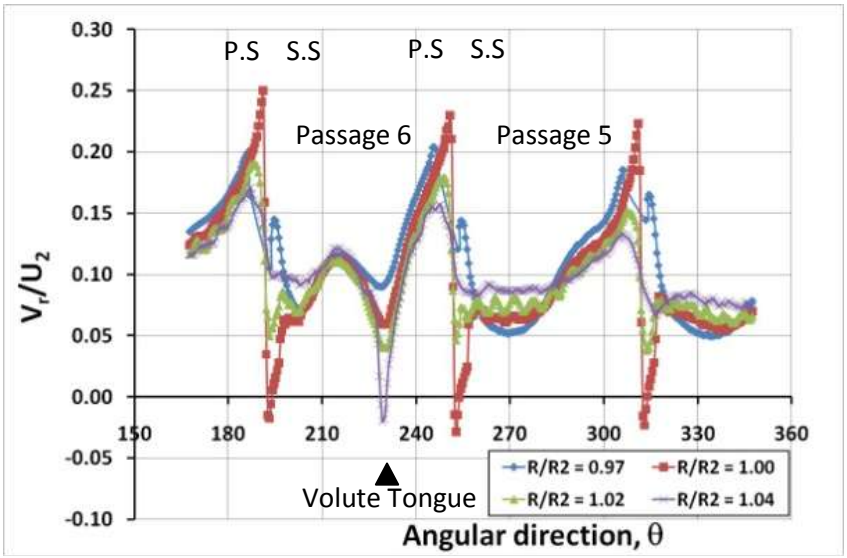

(d) 36 °

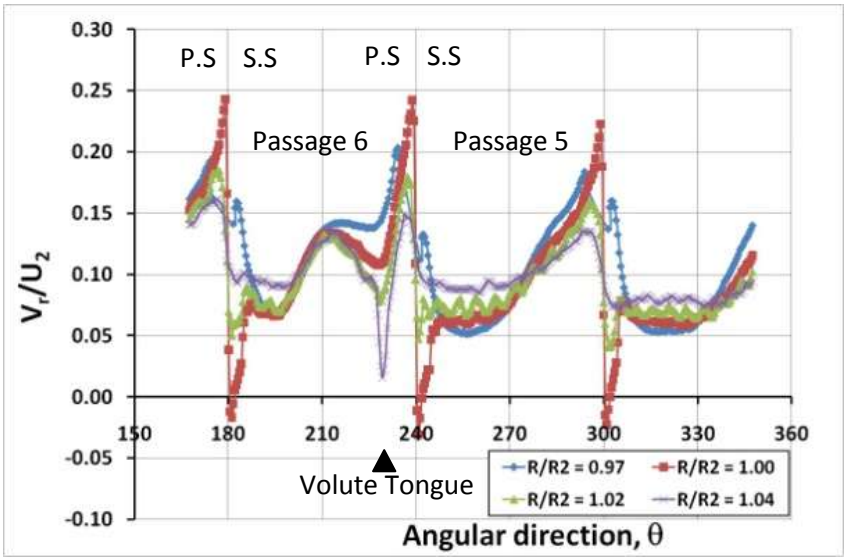

(e) 48°

Figure 6-8 Mid Plane radial velocity coefficient V_r/U_2 at Q_{design} .

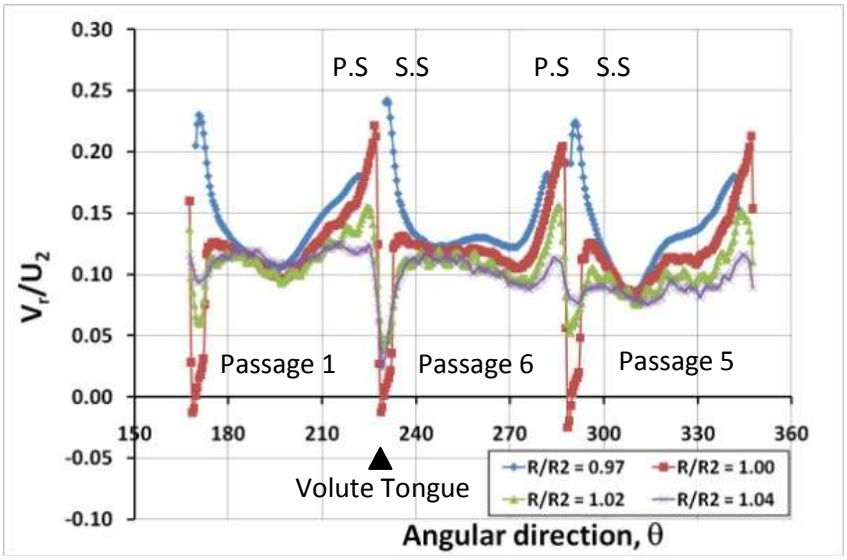
P.S S.S P.S S.S
Passage 1
Passage 6
Passage 5
Volute Tongue
R/R2 = 0.97
R/R2 = 1.00
R/R2 = 1.02
R/R2 = 1.04
Vr/U2
Angular direction, θ

(a) 0 °

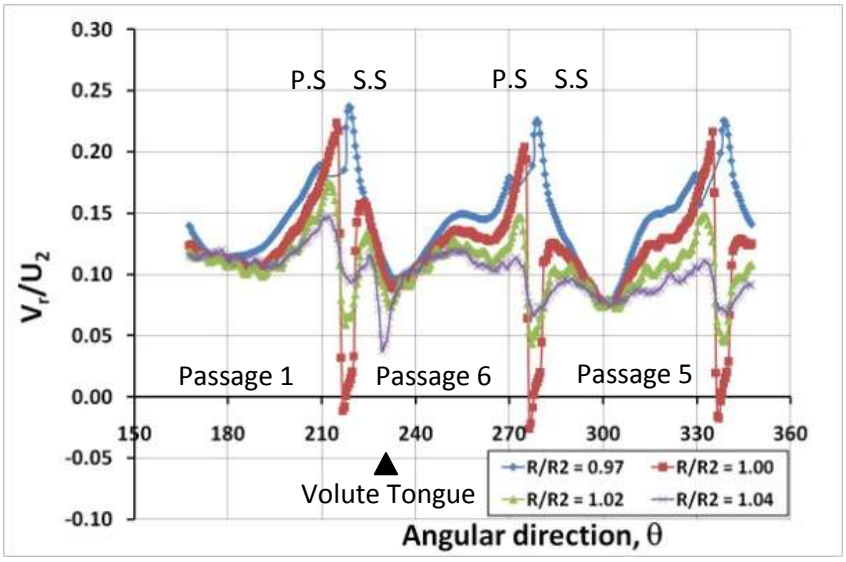
P.S S.S P.S S.S
Passage 1
Passage 6
Passage 5
Volute Tongue
R/R2 = 0.97
R/R2 = 1.00
R/R2 = 1.02
R/R2 = 1.04
Vr/U2
Angular direction, θ

(b) 12 °

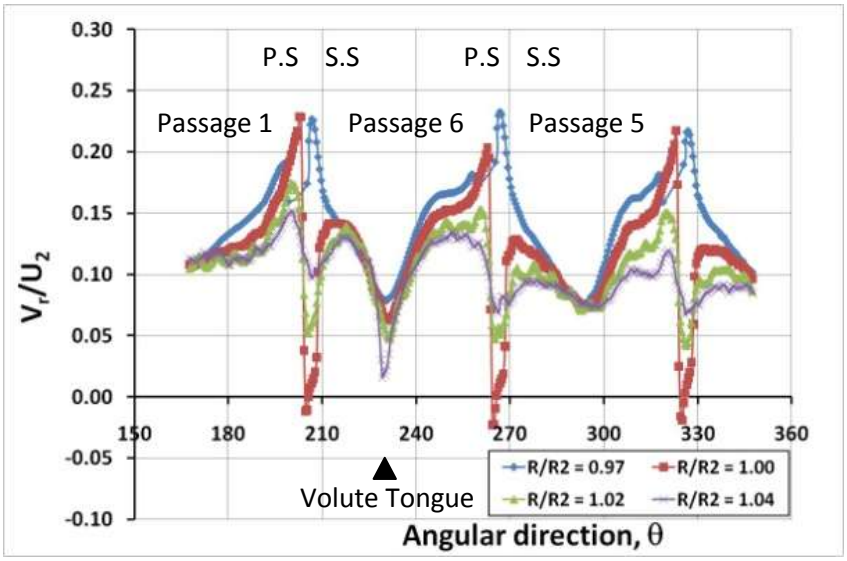
P.S S.S P.S S.S
Passage 1
Passage 6
Passage 5
Volute Tongue
R/R2 = 0.97
R/R2 = 1.00
R/R2 = 1.02
R/R2 = 1.04
Vr/U2
Angular direction, θ

(c) 24 °

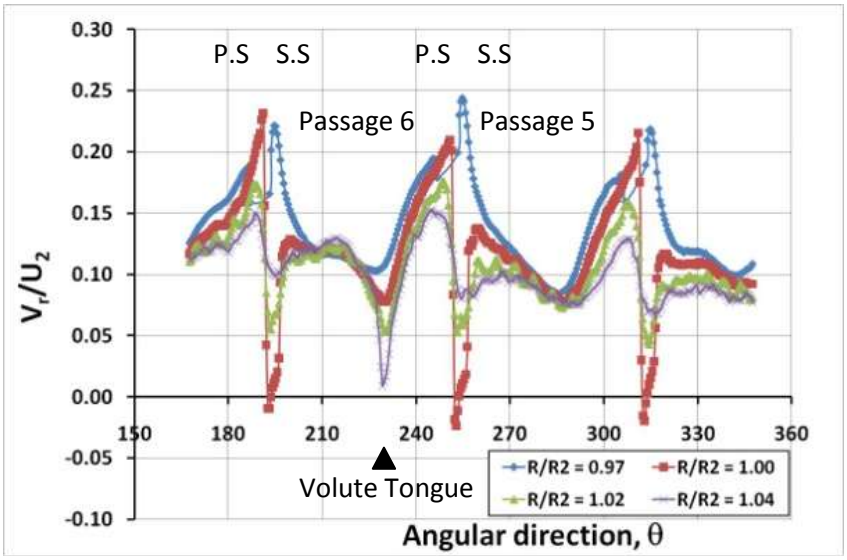

(d) 36 °

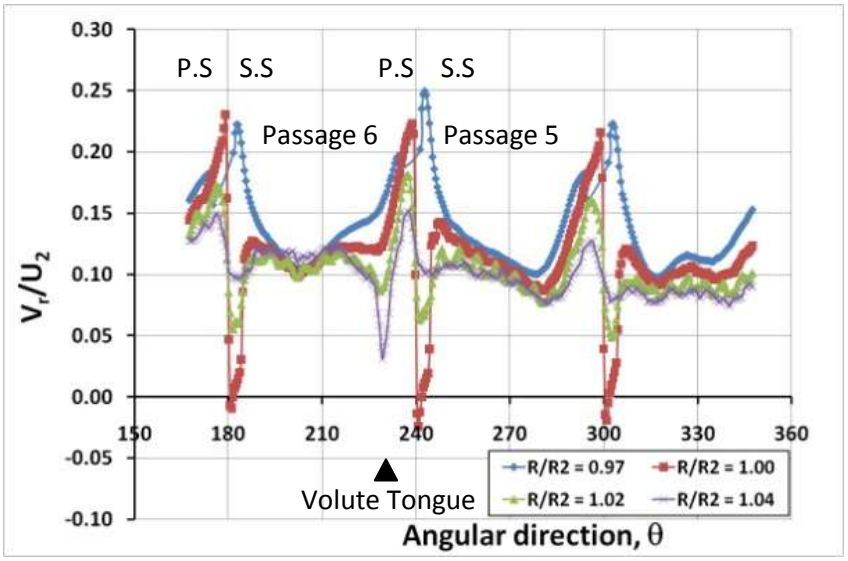

(e) 48°

Figure 6-9 Bottom Plane radial velocity coefficient V_r/U_2 at Q_{design} .

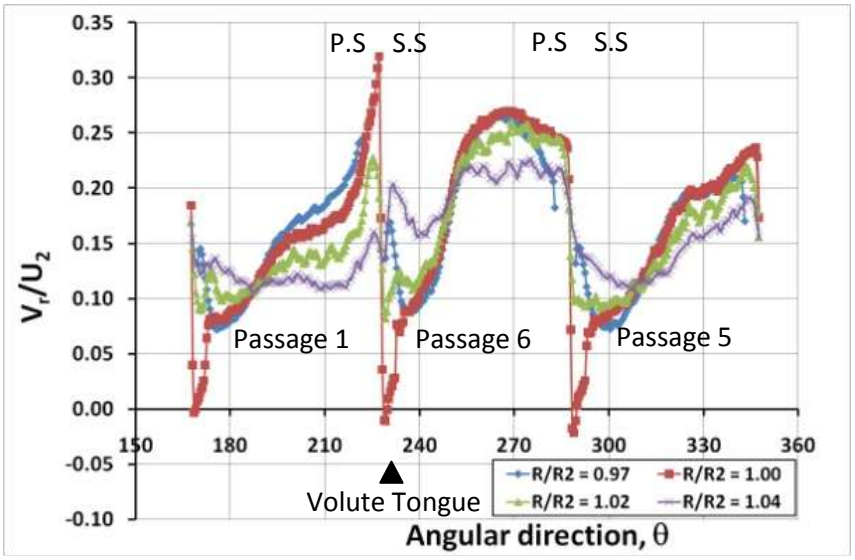
P.S
S.S
P.S
S.S
Passage 1
Passage 6
Passage 5
Volute Tongue
R/R2 = 0.97
R/R2 = 1.00
R/R2 = 1.02
R/R2 = 1.04
Angular direction, θ
Vr/U2

(a) 0 °

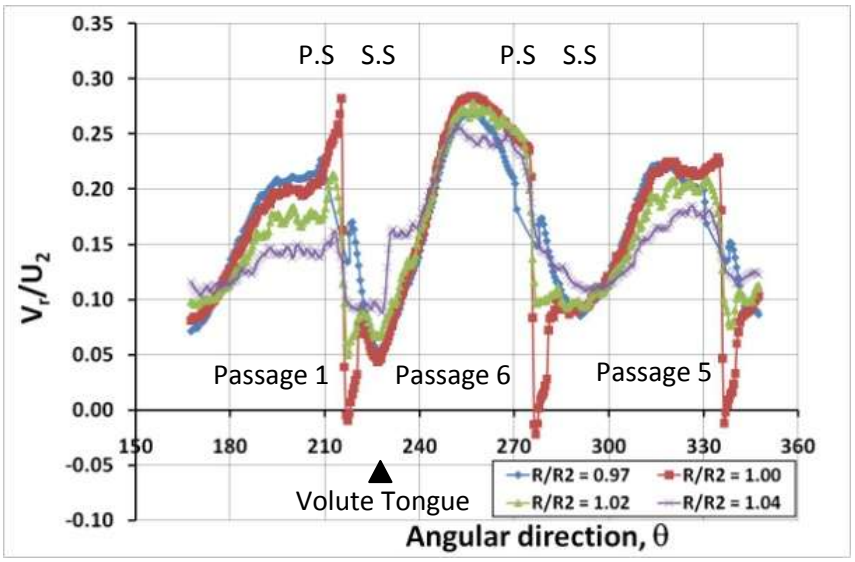
P.S
S.S
P.S
S.S
Passage 1
Passage 6
Passage 5
Volute Tongue
R/R2 = 0.97
R/R2 = 1.00
R/R2 = 1.02
R/R2 = 1.04
Angular direction, θ
Vr/U2

(b) 12 °

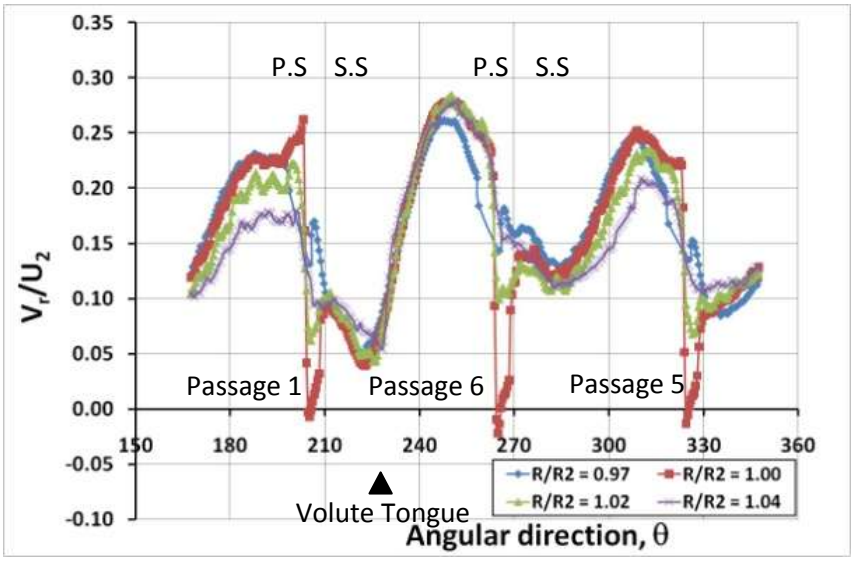
P.S
S.S
P.S
S.S
Passage 1
Passage 6
Passage 5
Volute Tongue
R/R2 = 0.97
R/R2 = 1.00
R/R2 = 1.02
R/R2 = 1.04
Angular direction, θ
Vr/U2

(c) 24 °

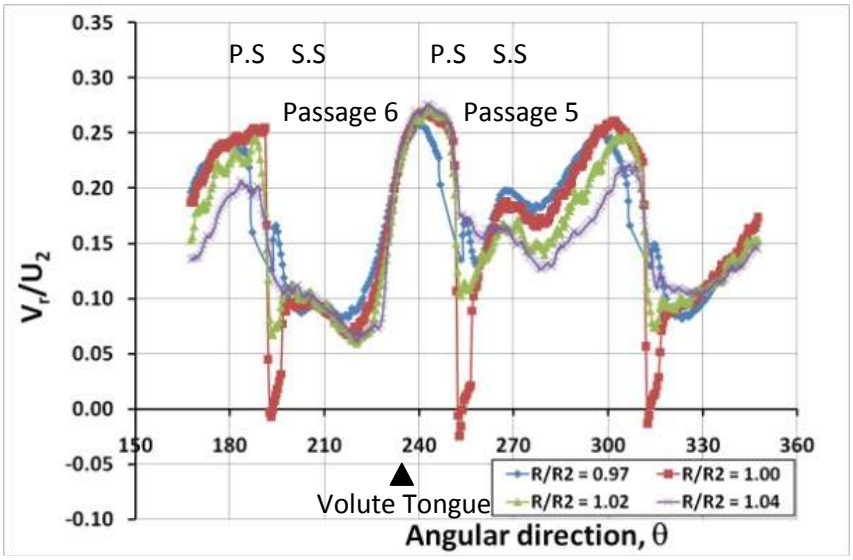

(d) 36 °

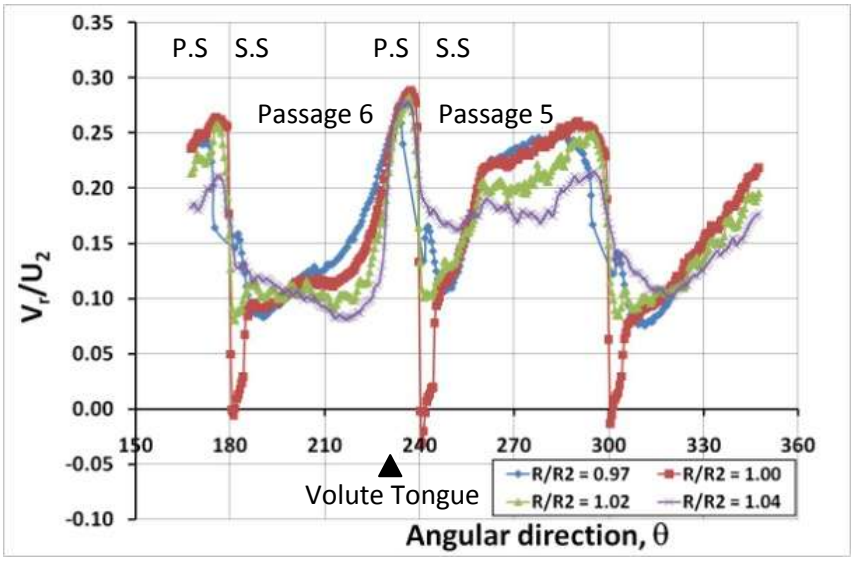

(e) 48°

Figure 6-10 Top Plane radial velocity coefficient V_r/U_2 at $1.3Q_{design}$.

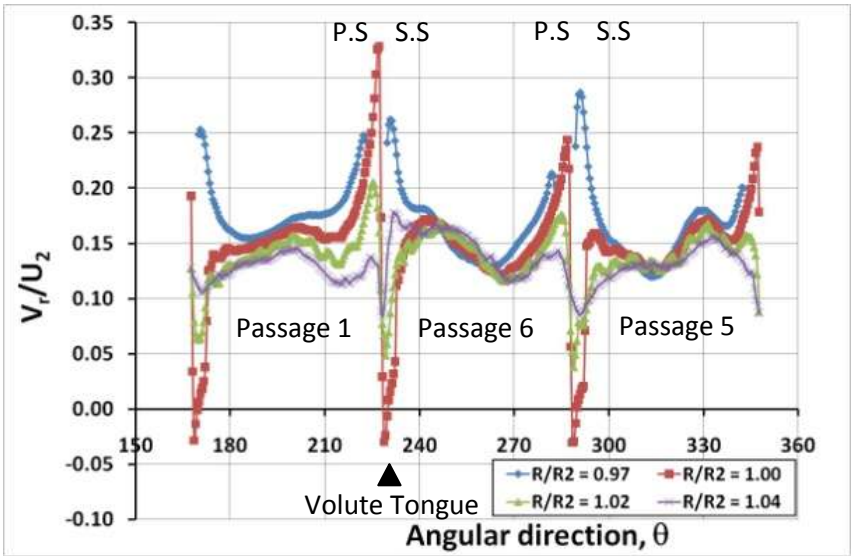
P.S S.S P.S S.S
Passage 1
Passage 6
Passage 5
Volute Tongue
R/R2 = 0.97
R/R2 = 1.00
R/R2 = 1.02
R/R2 = 1.04
Angular direction, θ
V_r/U_2

(a) 0 °

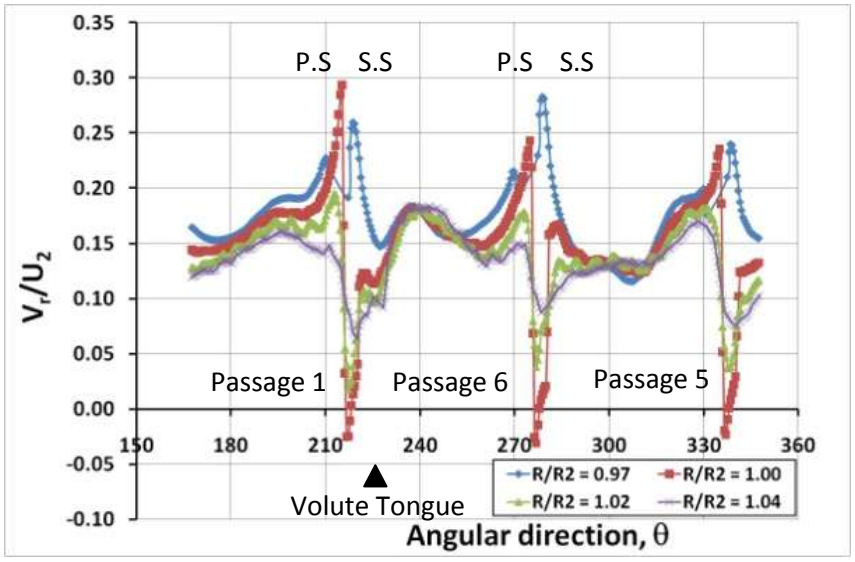
P.S S.S P.S S.S
Passage 1
Passage 6
Passage 5
Volute Tongue
R/R2 = 0.97
R/R2 = 1.00
R/R2 = 1.02
R/R2 = 1.04
Angular direction, θ
V_r/U_2

(b) 12 °

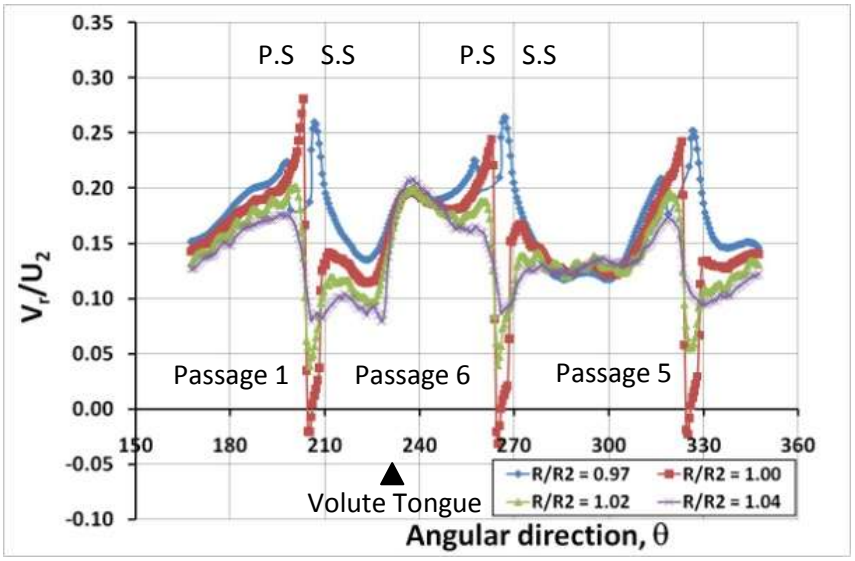
P.S S.S P.S S.S
Passage 1
Passage 6
Passage 5
Volute Tongue
R/R2 = 0.97
R/R2 = 1.00
R/R2 = 1.02
R/R2 = 1.04
Angular direction, θ
V_r/U_2

(c) 24 °

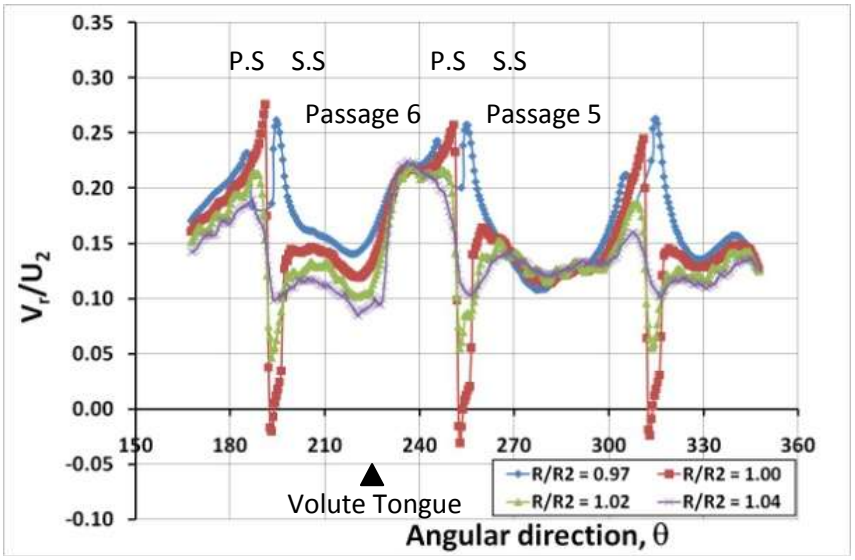

(d) 36 °

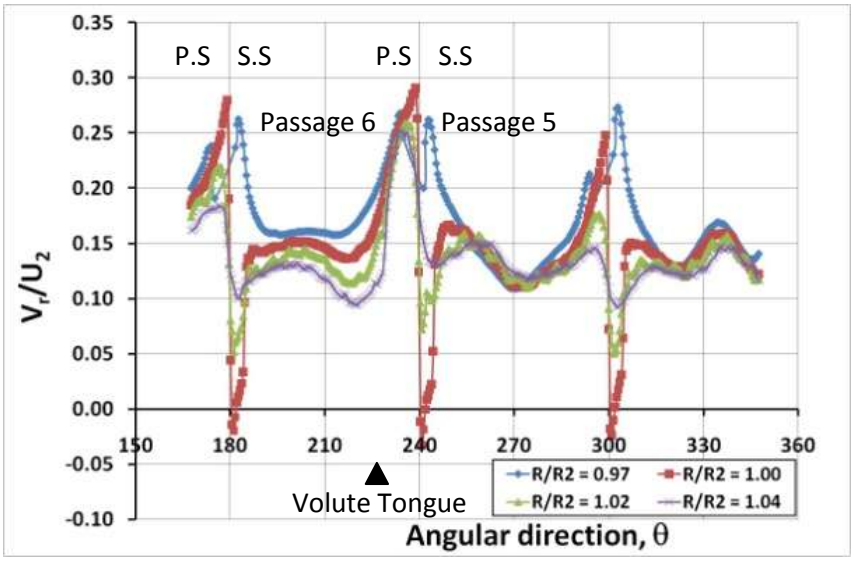

(e) 48°

Figure 6-11 Mid Plane radial velocity coefficient V_r/U_2 at $1.3Q_{design}$.

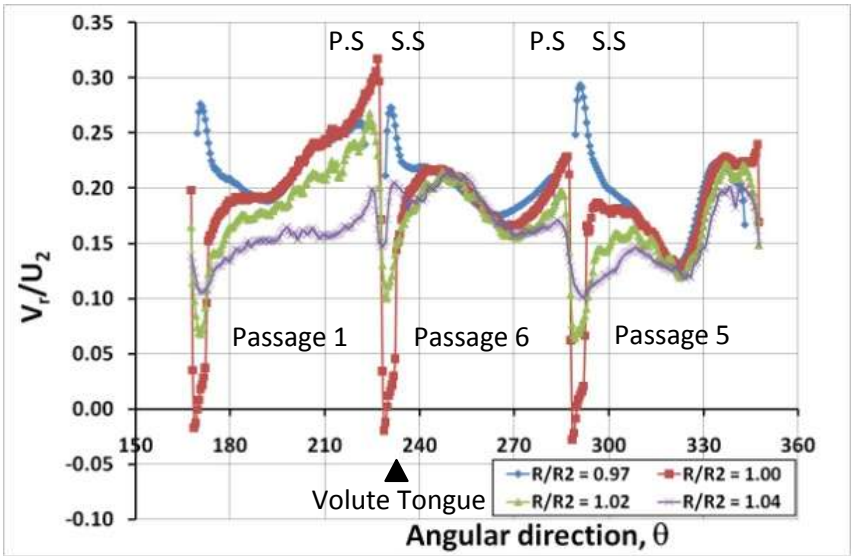
P.S S.S P.S S.S
Passage 1
Passage 6
Passage 5
Volute Tongue
R/R2 = 0.97
R/R2 = 1.00
R/R2 = 1.02
R/R2 = 1.04
Angular direction, θ
Vr/U2

(a) 0 °

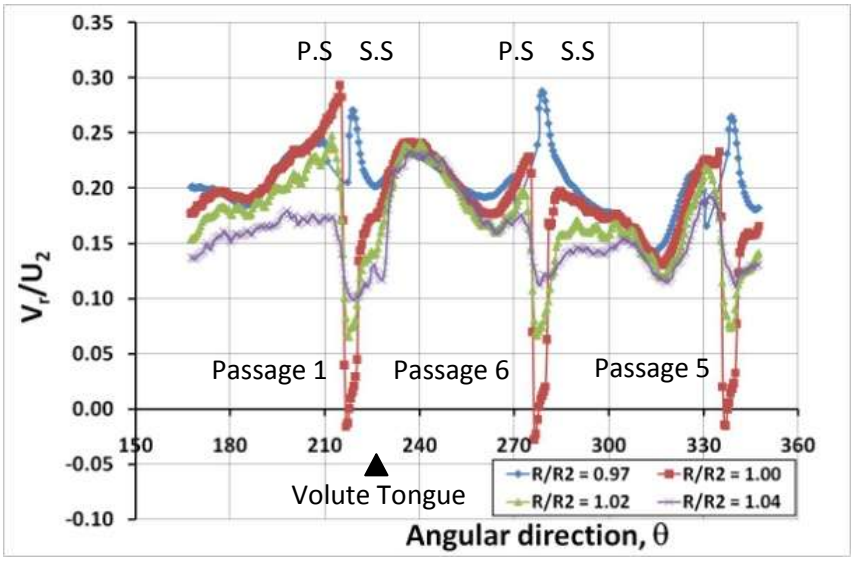
P.S S.S P.S S.S
Passage 1
Passage 6
Passage 5
Volute Tongue
R/R2 = 0.97
R/R2 = 1.00
R/R2 = 1.02
R/R2 = 1.04
Angular direction, θ
Vr/U2

(b) 12 °

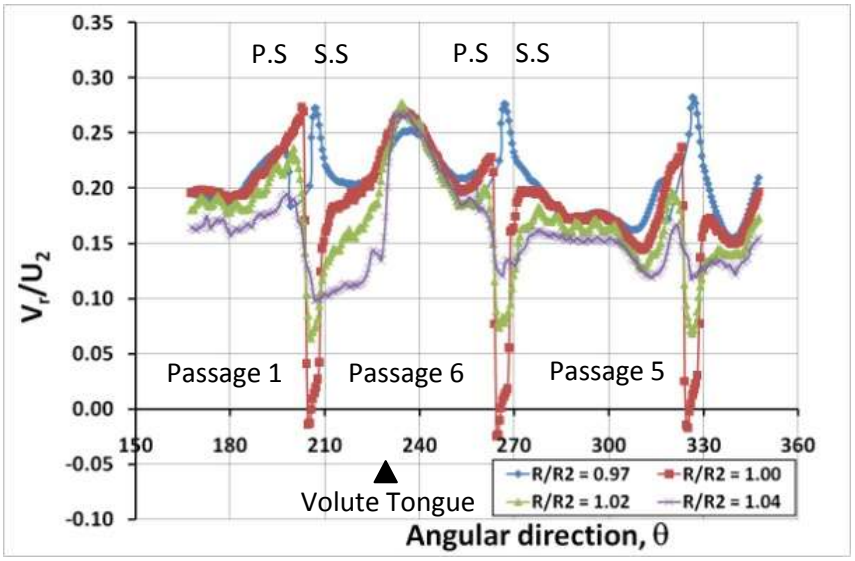
P.S S.S P.S S.S
Passage 1
Passage 6
Passage 5
Volute Tongue
R/R2 = 0.97
R/R2 = 1.00
R/R2 = 1.02
R/R2 = 1.04
Angular direction, θ
Vr/U2

(c) 24 °

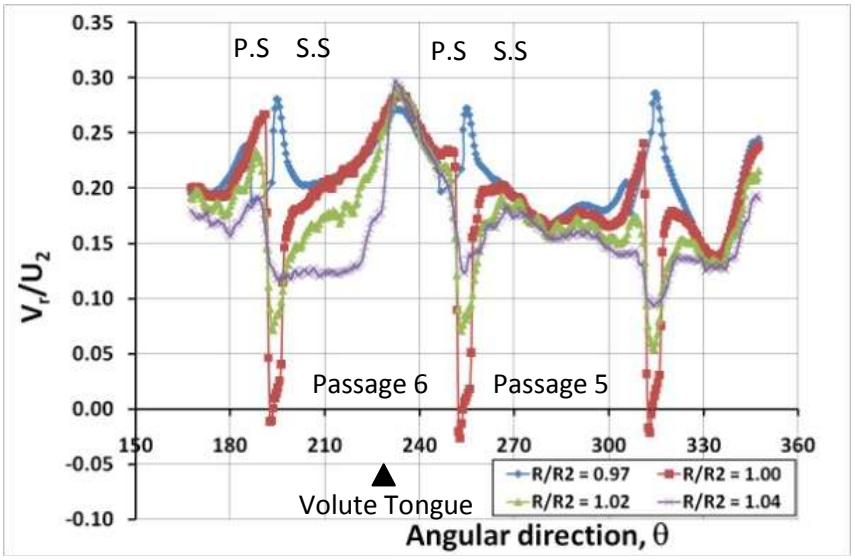

(d) 36 °

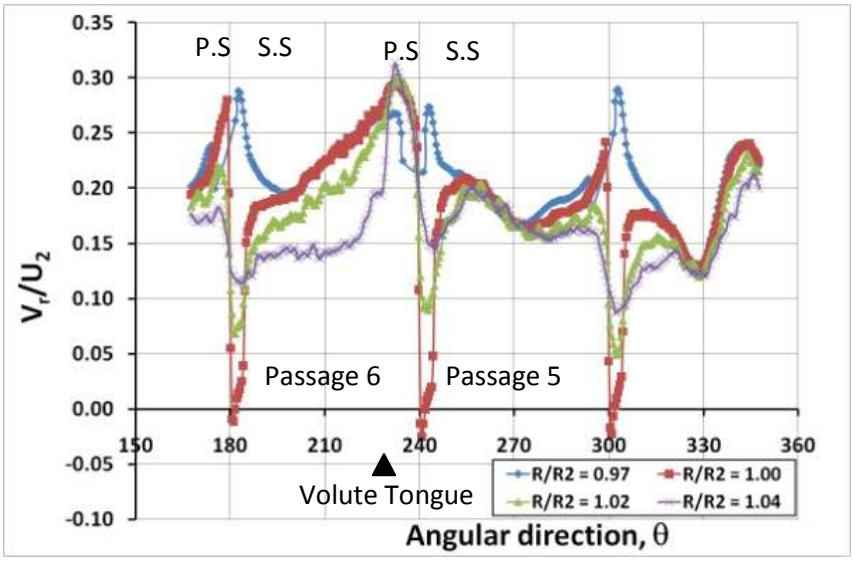

(e) 48°

Figure 6-12 Bottom Plane radial velocity coefficient V_r/U_2 at $1.3Q_{design}$.

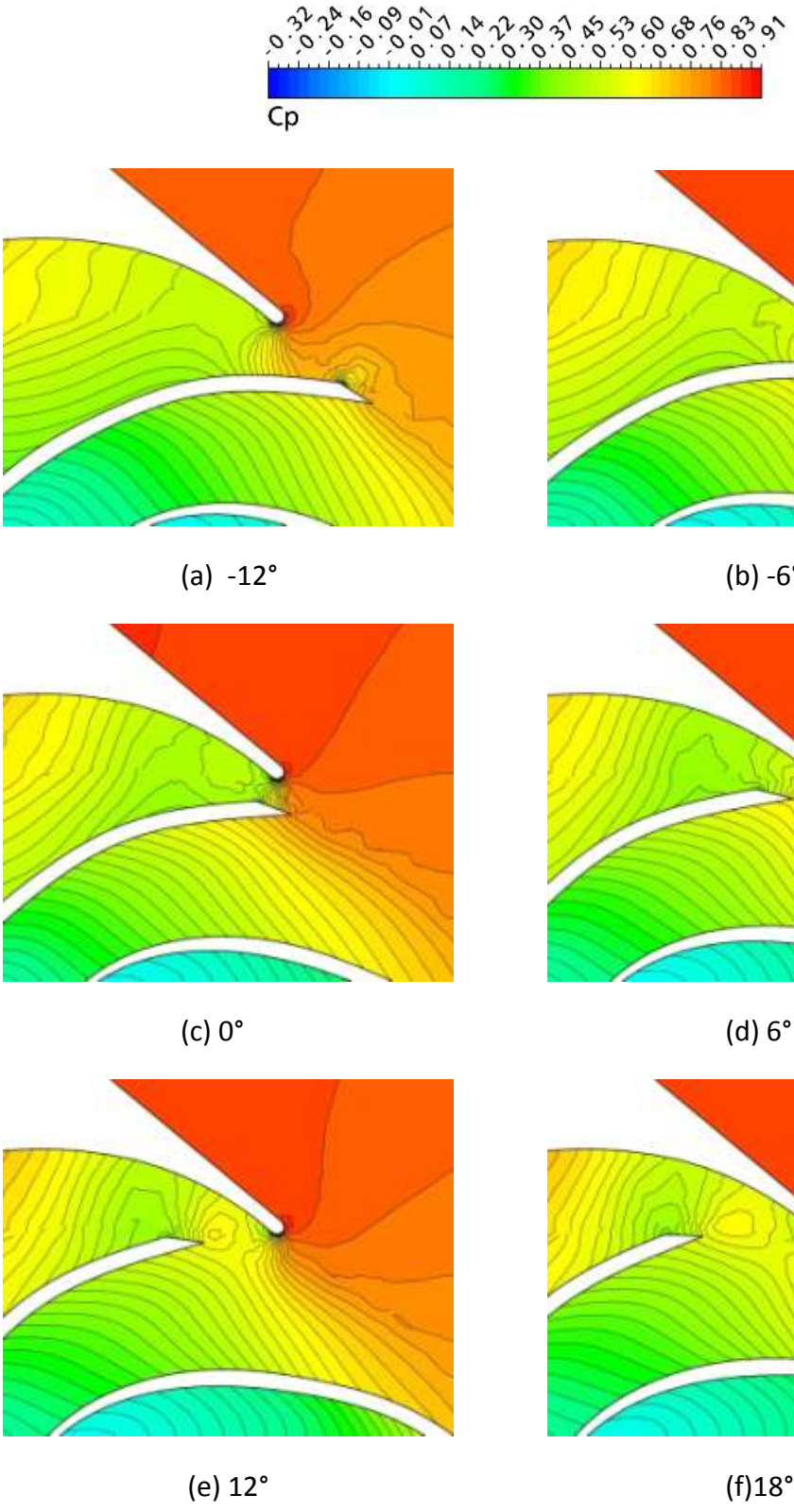

(a) -12° (b) -6°

(c) 0° (d) 6°

(e) 12° (f)18°

Figure 6-13 Pressure contours at $0.7Q_{design}$ with various relative volute tongue location.

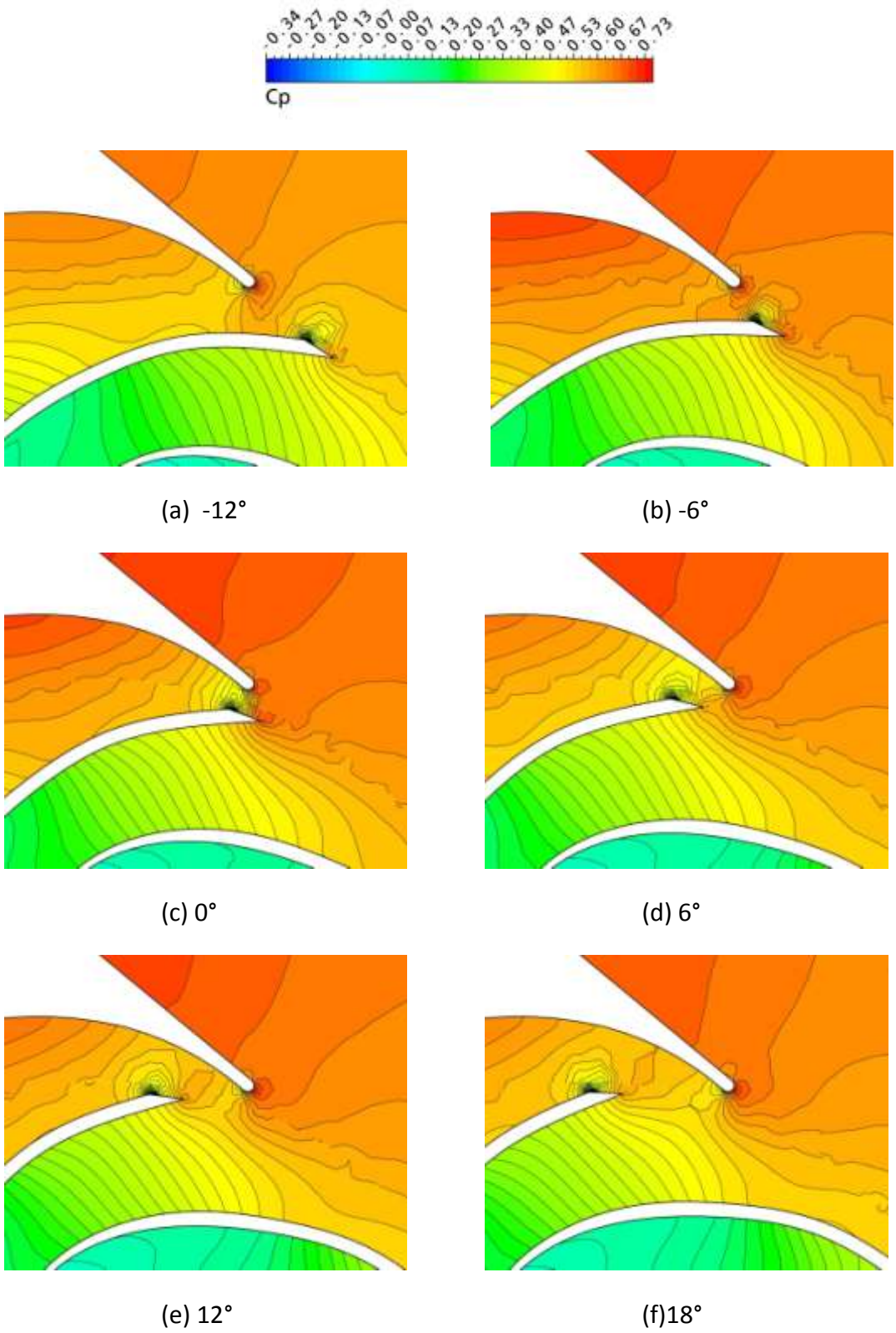

(a) -12°

(b) -6°

(c) 0°

(d) 6°

(e) 12°

(f)18°

Figure 6-14 Pressure contours at Q_{design} with various relative volute tongue location.

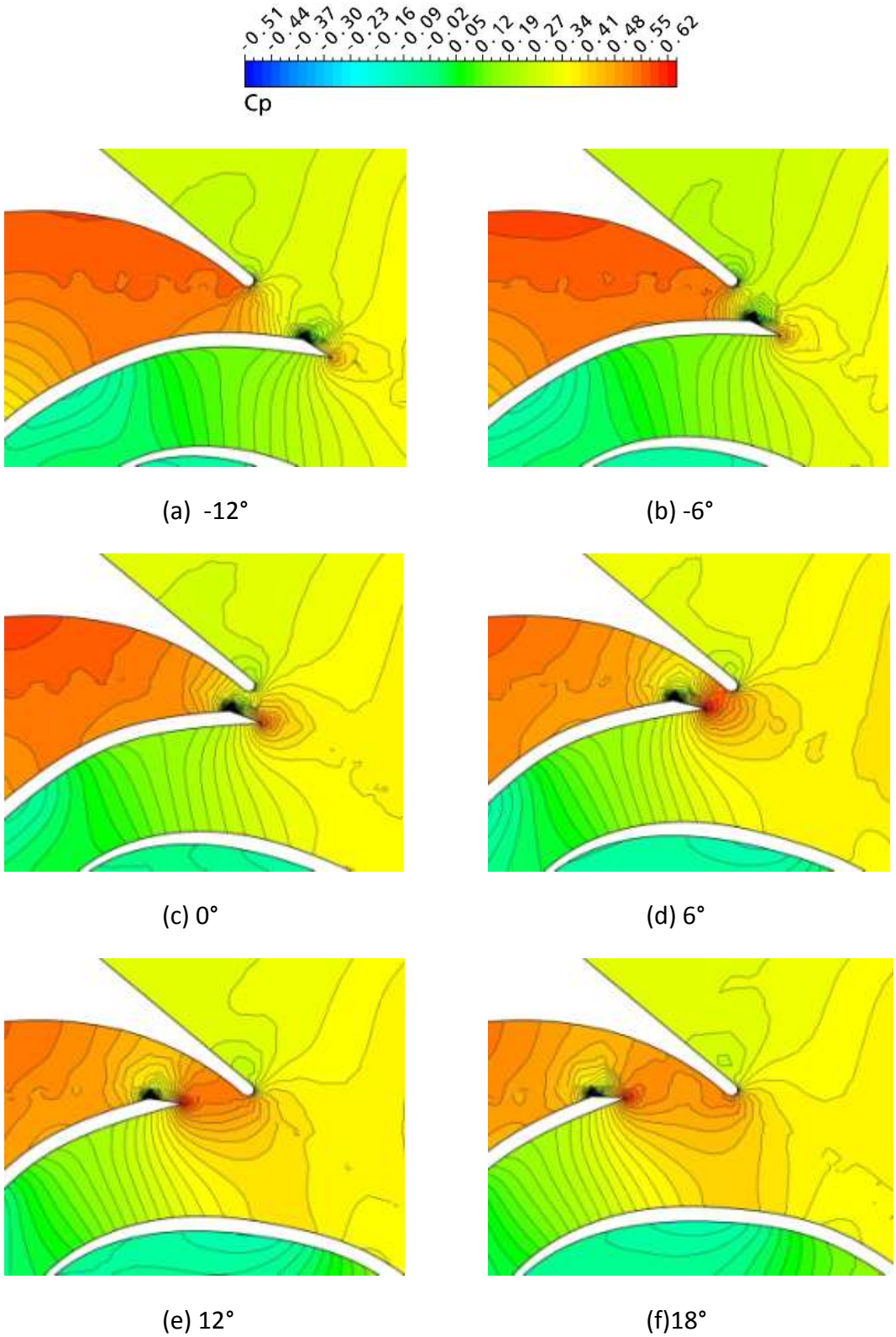

(a) -12° (b) -6°

(c) 0° (d) 6°

(e) 12° (f)18°

Figure 6-15 Pressure contours at 1.3Q_{design} with various relative volute tongue location

CHAPTER 7 CONCLUSIONS AND RECOMMENDATIONS

7.1 Conclusions

The complex pump internal flow field has been numerically investigated. The numerically predictions for steady and unsteady pump performance curves are in good agreement with experimental results over a wide range of flow rates. The numerical analysis captured the dynamics of the unsteady secondary flow structures starting from intake section, through the centrifugal impeller as well as inside the volute casing.

The numerical simulation at three different flow rates, $0.7Q_{design}$, Q_{design} and $1.3Q_{design}$ show that inlet flow structures of straight intake section is flow rate dependent and change its rotation direction either follows impeller rotation at low flow rate or to oppose impeller direction at high flow rate. For curved intake section pump, a pair of counter rotating vortices formed in the curved section before entering into impeller eye regardless of flow rates. Comparison of the pump performance of the curved and straight intake section show that the distorted inflow structures will have some effect on the pump performance. This is because the distorted inflow will cause the inlet velocity triangle to deviate from the design angle.

The three-dimensional turbulent flow field in a centrifugal pump is coupled with flow rate and impeller trailing edge relative position to volute tongue. Impeller passage flow at Q_{design} is smooth and follows the curvature of the blade but flow separation is observed at the leading edge due to non-tangential inflow condition. At $0.7Q_{design}$, there is a significant flow reversal and stalled flow near leading edge

shroud. At $1.3Q_{design}$, the flow separation is occurred on leading suction side and carries downstream to impeller passage.

The front shroud velocity pattern and leading edge flow separation has a great influence on the jet wake flow formation inside the impeller passage. A cross-sectional view of the impeller passage from leading edge to impeller exit shows that the wake flow near leading edge convected streamwise direction will has it core location moving from shroud o hub side and diffuses at $0.7Q_{design}$. At Q_{design} and $1.3Q_{design}$, the impeller passage flow is dominated by the jet flow rather near leading edge before decelerated to become a wake flow near impeller exit.

As for the pressure distribution, the pressure increase gradually along the stream-wise direction. The pressure lines are seen to be inclined in the circumferential direction. It is also found that the isobars are no longer perpendicular to the impeller suction surface at low flow rate. The results of unsteady analysis proved that the periodically pressure fluctuation is due to the position of impeller blade relative to tongue and the flow field within the volute casing is always unsteady and turbulent.

Analysis on surface streamlines on pressure and suction sides of the impeller vane show that streamlines are pressure driven in streamwise direction. On the vane pressure side, the streamlines follows the shroud and hub profile well. However, on the suction side, due to leading edge separation and flow rate influence, the streamlines are highly distorted near leading and trailing edges.

Counter rotating vortex flow is observed when impeller flow entering the volute casing circumferentially regardless of flow rates. Streamlines starting from impeller exit near volute tongue and circumferentially advancing in streamwise direction form a wrapping vortex tube before approach volute exit. At $0.7Q_{design}$, there is flow re-

entrance to volute tongue region because of negative flow incidence angle. However, wake flow formation behind volute tongue at $1.3Q_{design}$ is like a strong shearing flow due to positive flow incidence angle.

The pressure field is coupled with flow rate and impeller trailing edge relative position to volute tongue. This is because there is a strong pressure pulsation and change of pressure distribution around the impeller and volute casing when the impeller rotates. The blade pressure distribution different on the pressure and suction sides of the vanes also depend on flow rate as well.

From the impeller exit flow analysis, it shows that the wake flow shedding and impingement is strongly affected by the jet wake flow formation within the impeller passage and relative position of blade trailing edge. The jet wake flow pattern inside the impeller passage is coupled with the flow rate. Because leading edge flow separation and recirculation carry downstream to impeller passage affecting the distorted flow at impeller exit. At $0.7Q_{design}$, the wake flow shedding strongly affected by the volute tongue position. The wake flow core breaks up when the volute moved pass the impeller passage due to high blade passing frequency and low wake flow momentum. However, at Q_{design} and $1.3Q_{design}$, the wake flow shedding is weakly coupled with impeller volute tongue interaction. The wake flow core is diffused slowly as volute tongue moved passed the impeller passage.

The impeller exit flow velocity is further resolved into radial components to study the strong impeller volute tongue interaction. When the impeller trailing edge is aligned with the volute tongue, the radial velocity V_r/U_2 increases from suction to pressure side within blade-to-blade passage. However, when the impeller rotates, a

flow reversal of V_r/U_2 is observed around the volute tongue. This flow reversal V_r/U_2 can be characterized by the wake flow shedding and impingement.

7.2 Recommendations for Future Works

Even though existing work provided a good understanding of the secondary flow formation and development from intake section, through the centrifugal impeller and finally at volute casing, but there are still a lot of future works can be done to further understand and improve the pump performances. The following recommendations can be considered for future works:

1. From the analysis the inlet flow structure already proved to cause head coefficient deviation. The difference of pump NPSHr for different intake sections clearly highlighted the effect of inlet flow structures on cavitation from the experiment as well. It will be worthwhile to experimentally and numerically study how the inlet flow structures can influence the formation of cavitation inside the centrifugal pump.

2. The jet wake flow formation inside the impeller passage strongly depends on the upstream or inlet flow conditions as well as the flow rate. The impeller blade profile or curvature and passage geometry influence on the jet wake flow leaving the impeller should be considered in future by introducing other non-dimensional parameters that can quantify all these effects.

3. The current CFD model only investigates the flow in single phase. An attempt to model the flow field inside the centrifugal pump under multiphase flow condition and higher viscosity will be of great interest as

well. This is because multiphase flow and high viscosity flow in a centrifugal pump is very important, especially in oil and gas industry.

REFERENCES

Abramian, M., and Howard, J.H.G., 1994, "Experimental Investigation Of The Steady And Unsteady Relative Flow In A Model Centrifugal Impeller Passage", *ASME J. of Fluids Eng., Vol. 116, pp. 269-279*

Al-Qutub, A., Khalifa, A., and Khulief, Y., 2009, "Experimental Investigation Of The Effect Of Radial Gap And Impeller Blade Exit On Flow Induced Vibration At The Blade Passing Frequency In A Centrifugal Pump", *International J. of Rotating Machinery, Vol. 2009, Article I.D 704845*

Asuaje, M., Bakir, F., Kergourlay, G., Noguera, R., and Rey R., 2006, "Three-Dimensional Quasi-Steady Flow Simulation In A Centrifugal Pump: Comparison With Experiment Results", *Proc. IMechE Part A: J. Power and Energy, Vol. 220, pp. 239-256*

Ayder, E., Van den Braenbussche, R.A., and Brasz, J.J., 1993, "Experimental And Theoretical Analysis Of The Flow In A Centrifugal Compressor Volute", *ASME J. of Turbomachinery, Vol. 115, pp. 582-589*

Ayder, E., Van den Braenbussche, R.A., and Brasz, J.J., 1994, "Numerical Analysis Of Three-Dimensional Swirling Flow In Centrifugal Compressor Volutes", *ASME J. of Turbomachinery, Vol. 116, pp. 462-468*

Azzola, J., and Humphrey, J.A.C., Iacovides, H., and Launder B.E., 1986, "Developing Turbulent Flow In A U-Bend Of Circular Cross-Section: Measurement And Computation", *ASME J. of Fluids Eng., Vol. 108, pp. 214-221*

Barrio, R., Parrondo, J., and Blanco E., 2010, "Numerical Analysis Of The Unsteady Flow In The Near-Tongue Region In A Volute-Type Centrifugal Pump For Different Operating Points", *Computer and Fluids, 39, pp. 859-870*

Barrio, R., Blanco, E., Parrondo, J., Gonzalez, J., and Fernandez J., 2008, "The Effect Of Impeller Cutback On The Fluid-Dynamics Pulsations And Load At The Blade-Passing Frequency In A Centrifugal Pump", *ASME J. of Fluids Eng., Vol. 130, pp. 111021-11*

Berger, S. A., and Talbot, L., 1983, “Flow In Curved Pipes”, *Ann. Rev. Fluid Mech., Vol. 15, 461-512*

Blanco-Marigorta, E., Fernandez-Francos, J., Gonzalez-Perez, J., and Santolaria-Morros, C., 2000, “Numerical Flow Simulation in A Centrifugal Pump with Impeller-Volute Interaction”, *Proc. of ASME Fluids Engineering Division Summer Meeting, June 11-15. Massachusetts, Boston, U.S*

Bolpaire, S. and Barrand, J.P., 1999, “Experimental Study Of The Flow In The Suction Pipe Of A Centrifugal Pump At Partial Flow Rates In Unsteady Conditions”, *ASME J. of Pressure Vessel Technology, Vol. 121, pp.291-295*

Bolpaire S., Barrand J.P., and Caignaert G., 2002, “Experimental Study Of The Flow In The Suction Pipe Of A Centrifugal Impeller: Steady Conditions Compared With Fast Start-Up”, *International J. of Rotating Machinery, 8(3):215-222*

Bwalya, A.C., and Johnson M.W., 1996, “Experimental Measurements In A Centrifugal Pump”, *ASME J. of Fluids Eng., Vol. 116, pp. 692-697*

Byskov, R.K., Jacobsen, C.B., and Pedersen N., 2003, “Flow In A Centrifugal Pump At Design And Off-Design Conditions – Part II: Large Eddy Simulations”, *ASME J. Of Fluids Eng., Vol. 125, pp. 73-83*

Choi, Y.D., Nishino, K., Jurokawa, J., and Matsui J., 2004, “PIV Measurement of Internal Flow Characteristics of Very Low Specific Semi-open Impeller”, *Experiments in Fluids, 37, pp. 617-630*

Choi, Y.D., Kurokawa, J., and Matsui J., 2006, “Performance and Internal Flow Characteristics of a Very Low Specific Speed Centrifugal Pump”, *ASME J. of Fluids Eng., Vol. 128, pp. 341-349*

Chu, S., Dong, R., and Katz J., 1995, “Relationship Between Unsteady Flow, Pressure Fluctuations, And Noise In A Centrifugal Pump; Part B: Effects Of Blade-Tongue Interactions”, *ASME J. of Fluids Eng., Vol. 177, pp. 30-35*

Coutier-Delgosha, O., Fortes-Patella, R., Reboud, J.L., Hofmann, M., and Stoffel, B., 2003, "Experimental And Numerical Studies In A Centrifugal Pump With Two-Dimensional Curved Blades In Cavitating Condition", *ASME J. of Fluids Eng., Vol. 125, pp. 970-978*

Croba, D, and Kueny, J.L., 1996, "Numerical Calculation Of 2D, Unsteady Flow In Centrifugal Pumps: Impeller And Volute Interaction", *Int. J. for Num. Meth. Fluids Vol. 22, pp. 467–81*

Dong, R., Chu, S., and Katz, J., 1992, "Quantitative Visualization Of The Flow Within The Volute Of A Centrifugal Pump. Part B: Results And Analysis", *ASME J. of Fluids Eng., Vol. 114, pp. 396-403*

Dong, R., Chu, S., and Katz, J., 1997, "Effect Of Modification To Tongue And Impeller Geometry On Unsteady Flow, Pressure Fluctuations, And Noise In A Centrifugal Pump", *ASME J. of Turbomachinery, Vol. 119, pp. 506-515*

Dring, R. P., Joslyn, H. D., Hardwin, L. W., and Wagner, J. H., 1982 ''Turbine Rotor-Stator Interaction,'' *ASME J. Eng. Power*, V*ol. 104, pp. 729–742*

Eckardt, D., 1975, "Instantaneous Measurements In The Jet-Wake Discharge Flow Of A Centrifugal Compressor", *ASME J. of Eng. for Power, pp. 337-345*

Eckardt, D., 1976, "Detailed Flow Investigations Within A High Speed Centrifugal Compressor", *ASME J. of Fluids Eng., pp. 390-402*

Elholm, T., Ayder, E., and Van den Braembussche, R.A., 1992, "Experimental Study Of The Swirling Flow In Volute Of Centrifugal Pump", *ASME J. of Turbomachinery, Vol. 114, pp. 366-372*

Enayet, M. M., Gibson, M. M., Taylor, A. M. K. P., and Yianneskis, M., 1982, "Laser-Doppler Measurements Of Laminar And Turbulent Flow In A Pipe Bend", *Int. J. Heat & Fluid Flow, Vol. 3, No 4, pp. 213-219*

Feng, J.J., Benra F.K., and Dohmen H.J., 2007, “Numerical Investigation On Pressure Fluctuations For Different Configurations Of Vaned Diffuser Pumps” *International J. of Rotating Machinery, Vol. 2007, Article ID 34752*

Feng, J.J., Benra F.K., and Dohmen H.J., 2009, “Comparison Of Periodic Flow Fields In A Radial Pump Among CFD, PIV, And LDV Results” *International J. of Rotating Machinery, Vol. 2009, Article ID 410838*

Flack, R.D., Hamkins, C.P., and Brady, D.R., 1987, “Laser Velocimeter Turbulence Measurements In Shrouded And Unshrouded Radial Flow Pump Impellers”, *Int. J. Heat and Fluid Flow, Vol. 8, pp. 16-25*

Gonzalez, J., Fernandez, J., Blanco, E., and Santolaria, C., 2002, “Numerical Simulation Of The Dynamic Effects Due To Impeller Volute Interaction In A Centrifugal Pump”, *ASME J. of Fluids Eng., Vol. 124, pp. 348-355*

Gonzalez, J., and Santolaria, C., 2006, “Unsteady Flow Structure And Global Variables In A Centrifugal Pump”, *ASME J. of Fluids Eng., Vol. 128, pp. 937-946*

Gonzalez, J., Manuel, J., Oro, M., Diaz, K.M.A., and Blanco, E., 2009, “Unsteady Flow Pattern For A Double Suction Centrifugal Pump”, *ASME J. of Fluids Eng., Vol. 131, pp. 071102-1-9*

Gulich, J.F., 2008, “Centrifugal Pumps”, *Springer*

Gulich, J.F., 1999, “Impact Of Three-Dimensional Phenomena On The Design Of Rotodynamic Pumps”, *Proc. Instn. Mech. Engrs. Part C, Vol. 213, pp.59-70*

Gulich, J. F., and Bolleter, U., 1992, “Pressure Pulsations In Centrifugal Pumps”, *ASME J. Vibr. Acoust., Vol. 114, pp. 272–279*

Gulich, J.F., 1999, “Impact Of Three-Dimensional Phenomena On The Design Of Rotodynamic Pumps”, *Proc. Instn. Mech. Engrs. Vol. 213 Part C, pp. 59-70*

Hagelstein, D., Hillewaert, K., Braembussche, R.A.V.D., Engenda, A., Keiper, R, and Rautenberg, M., 2000, “Experimental And Numerical Investigation Of The Flow

In A Centrifugal Compressor Volute", *ASME J. of Turbomachinery, Vol. 122, pp. 22-31*

Hampkins, C.P., and Bross, S., 2002, "Use Of Surface Flow Visualization Methods In Centrifugal Pump Design", *ASME J. of Fluids Eng., Vol. 124, pp. 314-318*

Huang S., Islam M. F., and Liu P.F., 2006, "Numerical simulation of 3D turbulent flow through an entire stage in a multistage centrifugal pump", *Int. J. of Computational Fluid Dynamics, Vol. 20, No. 5, June, 309–314*

He, L., and Sato, K., 2001, "Numerical Solution Of Incompressible Unsteady Flows In Turbomachniery", *ASME J. of Fluids Eng., Vol. 123, pp. 680-685*

Hong, S.S., and Kang, S.H., 2002, "Exit Flow Measurement Of A Centrifugal Pump Impeller", *KSME International Journal, Vol. 16, No.9, pp. 1147-1155*

Horlock, J.H. and Denton J.D., 2005, "A Review Of Some Early Design Practice Using Computational Fluid Dynamics And A Current Perspective", *ASME J. of Turbomahcinery, Vol. 127, pp. 5-13*

Howard, J.H.G., and Kittmer, C.W., 1975, "Measured Passage Velocities In A Radial Impeller With Shrouded And Unshrouded Configurations", *ASME J. of Engineering for Power, pp. 207-213*

Huang, S., Islam, M. F., and Liu, P.F., 2006, "Numerical Simulation Of 3D Turbulent Flow Through An Entire Stage In A Multistage Centrifugal Pump", *Int. J. of Computational Fluid Dynamics, Vol. 20, No. 5, pp. 309–314*

Iversen, H.W., Rolling, R.E., and Carlson J.J., 1960, "Volute Pressure Distribution, Radial Force On The Impeller, And Volute Mixing Losses Of A Radial Flow Centrifugal Pump", *ASME J. of Eng. For Power, pp. 136-144*

Johnson, M.W., and Moore, J., 1980, "The Development Of Wake Flow In A Centrifugal Impeller", *ASME J. of Eng. for Power, Vol. 102, pp. 382-390*

Kaupert, K. A., and Staubli, T., 1999, “The Unsteady Pressure Field In A High Specific Speed Centrifugal Pump Impeller Part I: Influence Of The Volute”, *ASME J. of Fluids Eng., Vol. 121, pp. 621-626*

Kelder, J.D.H., Dijkers, R.J.H., van Esch, B.P.M., and Kruyt, N.P., 2001, “Experimental And Theoretical Study Of The Flow In The Volute Of A Low Specific-Speed Pump”, *Fluid Dynamics Research, Volume 28, Issue 4, pp. 237-310*

Kikuyama, K., Hasegawa, H., and Maeda, T., 1992, “Unsteady Pressure Change In Centrifugal Pump Impeller Passages Due To Inlet Swirl”, *J. of Fluids and Structures, Vol. 6, pp. 337-351*

Kosyna, G., Suryawijaya, P., and Friedrichs, J., 2001, “Improved Understanding Of Two Phase Flow Phenomena Based On Unsteady Blade Pressure Measurements”, *J. of Computational and Applied Mechanics, Vol. 2, No. 1, pp.45-52*

Lazarkiewicz, S., and Troskolanski, A.T., 1965, “Impeller Pumps”, *Pergamon Press*

Lefebvre, P.J., and Barker, W.P., 1995, “Centrifugal Pump Performance During Transient Operation”, *ASME J. of Fluids Eng., Vol. 117, pp. 123-128*

Liu, C.H., Vafidis, C., and Whitelaw, J.H., 1994, “Flow Characteristics Of A Centrifugal Pump”, *ASME J. of Fluids Eng., Vol. 116, pp. 303-309*

Lipski, W., 1979, “The Influence Of Shape And Location Of The Tongue Of Spiral Casing On The Performance Of Single Stage Radial Pumps”, *Proc. Of 6th Conference Fluid Machinery, Budapest, pp. 673-680*

Lobanoff, V.S., and Ross, R.R., 1992, “Centrifugal Pumps Design And Application”, *2nd Edition, Butterworth-Heinemann*

Majidi, K., and Siekmann, H.E., 2000, ‘‘Numerical Calculation Of Secondary Flow In Pump Volute And Circular Casing Using 3D Viscous Flow Techniques’’, *International J. of Rotating Machinery, 6(4), pp. 245-252*

Majidi K., 2005, “Numerical Study Of Unsteady Flow In A Centrifugal Pump”, *ASME J. of Turbomachinery, Vol. 127, pp. 363-371*

Menter, F.R., 1994, “Two-equation eddy-viscosity turbulence models for engineering applications”, *AIAA-Journal., 32(8), pp. 1598 - 1605*

Miner, S.M., 2000, “Evaluation Of Blade Passage Analysis Using Coarse Grids” *ASME J. Fluids Eng., Vol. 122, pp. 345-348*

Morfiadakis, E. E., Voutsinas, S. G., and Papantonis, D. E., 1991, “Unsteady Calculation In A Radial Flow Centrifugal Pump With Spiral Casing”, *International Journal For Numerical Methods In Fluids, Vol. 12, pp. 895-908*

Morgenroth, M., and Weaver, D.S., 1998, “Sound Generation By A Centrifugal Pump At Blade Passing Frequency”, *ASME J. of Turbomachinery, Vol. 120, pp. 736-743*

Murakami, M., Kikuyama, K., and Asakura, 1980, “Velocity And Pressure Distributions In The Impeller Passages Of Centrifugal Pump”, *ASME J. of Fluids Eng., 102, pp. 420-426*

Neumann, B., 1991, “The Interaction Between Geometry And Performance Of A Centrifugal Pump”, *Mechanical Engineering Publications*

Nursen, E.C., Ayder, E., 2003, “Numerical Calculation Of The Three-Dimensional Swirling Flow Inside The Centrifugal Pump Volutes”, *International J. of Rotating Machinery, 9: 247-253*

Parrondo-Gayo, J.L., Gonzalez-Perez, J., and Fernandez-Francos J., 2002, “The Effect Of The Operating Point On The Pressure Fluctuations At The Blade Passage Frequency In The Volute Of A Centrifugal Pump”, *ASME J. of Fluids Eng., Vol. 124, pp. 784-790*

Pedersen, N., Larsen, P.S., and Jacobsen, C.B., 2003, “Flow In A Centrifugal Pump At Design And Off-Design Conditions – Part I: Particle Image Velocimetry (PIV) And Laser Doppler Velocimetry (LDV) Measurement”, *ASME J. of Fluids Eng., Vol. 125, pp. 61-72*

Predin, A., and Bilus, I., 2003, “Influence Of Additional Inlet Flow On The Prerotation And Performance Of Centrifugal Impellers”, J. *of Hydraulic Research, Vol. 41, No. 2, pp. 207-216*

Rose, M.G., 2004, “Low Flow Rate Effects In A Centrifugal Pump Impeller”, *Proc. Instn. Mech. Engrs. Vol .218 Part A: J. Power and Energy, pp. 417-427*

Spence, R., and Amaral-Teixeira, J., 2008, “Investigation Into Pressure Pulsations In A Centrifugal Pump Using Numerical Methods Supported by Industrial Tests”, *Computers & Fluids, Vol. 37, 690-704*

Spence, R., and Amaral-Teixeira, J., 2009, “A CFD Parametric Study Geometrical Variations on the Pressure Pulsations and Performance Characteristics of a Centrifugal Pump”, *Computers & Fluids, 38, 1243-1257*

Stepanoff, A.J., 1957, “Centrifugal And Axial Flow Pumps: Theory, Design And Application”, *2nd Ed. John Wiley & Sons Inc.*

Tamm, A., Ludwig, G., and Stoffel, B., 2001, “Numerical, Experimental And Theoretical Analysis Of The Individual Efficiencies Of A Centrifugal Pump”, *Proceeding of ASME FEDSM’01, New Orleans, Louisiana, May 29 – June 1*

Tsukamoto, H., and Oshashi, H., 1982, “Transient Characteristics Of A Centrifugal Pump During Starting Period”, *ASME J. of Fluids Eng., Vol. 104, pp. 6-14*

Tsukamoto, H., Matsunaga, S., Yoneda, H., and Hata, S., 1986, “Transients Characteristics Of A Centrifugal Pump During Stopping Period”, *ASME J. of Fluids Eng., Vol. 108, pp. 392-399*

Van den Braembussche, R.A., and Hande, B.M., 1990, “Experimental And Theoretical Study Of The Swirling Flow In Centrifugal Compressor Volutes”, *ASME J. of Turbomachinery, Vol. 112, pp. 38-43*

Van den Braembussche, R.A., Ayder, E., Hagelstein, D., Rautenberg, M., and Keiper, R., 1999, “Improved Model For The Design And Analysis Of Centrifugal Compressor Volutes”, *ASME J. of Turbomachinery, Vol. 112, pp. 619-625*

Visser, F.C., Brouwers, J.J.H., and Jonker, J.B., 1999, “Fluid Flow In A Rotating Low-Specific-Speed Centrifugal Impeller Passage”, *Fluid Dynamics Research, 24, pp. 275-292*

Wang, H., and Tsukamoto, H., 2003, “Experimental and Numerical Study of Unsteady Flow in a Diffuser Pump at Off-Design Conditions”, *ASME J. of Fluids Eng., Vol. 125, pp. 767-778*

Westra, R.W., Broersma, L., van Andel, K., and Kruyt, N.P., 2010, “PIV Measurements And CFD Computations Of Secondary Flow In A Centrifugal Pump Impeller”, *ASME J. of Fluids Eng., Vol. 132, pp. 061104-1-8*

Whitelaw, J.H., and Yu, S.C.M., 1993, “Turbulent flow in characteristics in an S-shaped diffusing duct”, Flow Measurement and Instrumentation, Vol. 3, No. 4, pp. 171-179.

Wilcox, D.C., 1986, “Multiscale model for turbulent flows”, 24th Aerospace Sciences Meeting. AIAA

Wislicenus, G.F., 1965, “Fluid Mechanics Of Turbomachinery”, *Dover Publications Inc.*

Wright, T., Madhaven, S., and Dire J., 1984, “Centrifugal Fan Performance With Distorted Inflows”, *ASME J. of Gas Turbines and Power, Vol. 106, pp. 895-900*

Wuibaut, G., Dupont, P., Bois, G., Caignaert, G., and Stanislas, M., 2001, “Analysis Of Low Velocities Within The Impeller And The Vaneless Diffuser Of A Radial Flow Pump”, *Proc. Instn. Mech. Engrs. Vol. 215 Part A, pp. 801-808*

Wuibaut, G., Bois, G., Dupont, P., Caignaert, G., and Stanislas, M., 2002, “PIV Measurements In The Impeller And The Vaneless Diffuser Of A Radial Flow Pump In Design And Off-Design Operating Conditions”, *ASME J. of Fluids Eng., Vol. 124, pp. 791-797*

Zangeneh, M., Schleer, M., Ploger, F., Hong, S.S., Roduner, C., Ribi, B., and Abhari, R.S., 2004, “Investigation Of An Inversely Designed Centrifugal Compressor

Stage-Part I: Design And Numerical Verification", *ASME J. of Turbomachinery, Vol. 126, pp. 73-81*

Zhang, M.J., Pomfret, M.J., and Wong, C.M., 1996a, "Three-Dimensional Viscous Flow Simulation In A Backswept Centrifugal Impeller At The Design Point", *International J. of Computers & Fluids Vol. 25, No. 5, pp. 497-507*

Zhang, M.J., Pomfret, M.J., and Wong, C.M., 1996b, "Performance Prediction Of A Backswept Centrifugal Impeller At Off-Design Conditions", *International J. F. Numerical Methods In Fluids, Vol. 23, pp. 883-895*

Zhao, Z.M., 2002, "Design of Centrifugal Pump Using Computational Fluid Dynamics", *M.Eng. Thesis, National University of Singapore*

PUBLICATIONS

Conference Papers:

1. K.W Cheah, T.S Lee, S.H Winoto, Z.M Zhao, 2006, "Numerical Simulation and Turbulent Flow Investigation of a Centrifugal Pump", Eleventh Asian Congress of Fluid Mechanics, 22-25 May, Kuala Lumpur, Malaysia
2. K W Cheah, T S Lee, S.H Winoto, 2006, "Numerical Flow Simulation in a Centrifugal Pump", 6th ASEAN ANSYS Conference, 31 Oct to 2 Nov, Singapore
3. K.W. Cheah, T.S. Lee , S.H. Winoto, 2007, "Numerical Flow Simulation & Visualization In A Centrifugal Pump", 9th Asian Symposium on Visualization 4-9 June, Hong Kong, ASV0108-001
4. K.W. Cheah, T.S. Lee, S.H. Winoto, 2007, "Numerical Analysis of Unsteady Fluid Flow in a Centrifugal Pump", The 9th Asian International Conference on Fluid Machinery. October 16-19, Jeju, Korea, No. AICFM9-191.
5. K.W. Cheah, T.S. Lee and S.H. Winoto, "Unsteady Fluid Flow Study in a Centrifugal Pump by CFD Method", The 7th ASEAN ANSYS Conference, 30th ~ 31st Oct, 2008, Biopolis, Singapore,
6. K.W. Cheah, T.S. Lee and S.H. Winoto, 2008, "Numerical Analysis of Impeller-Volute Tongue Interaction and Unsteady Fluid Flow in a Centrifugal Pump", The 4th International Symposium on Fluid Machinery and Fluid Engineering, 24th - 27th Nov, 2008, Beijing, China, NO. 4ISFMFg1E- IL-10
7. K.W. Cheah, T.S. Lee and S.H. Winoto, 2011, "Secondary Flow Structures in a Centrifugal Pump", The 11th Asian Symposium on Visualization, June 5-9, Toki Messe (Niigata Convention Centre), Niigata, Japan, ASV11-14-04,

Journal Papers:

1. K W Cheah, T S Lee, S.H Winoto, Z M Zhao, 2007, “Numerical Flow Simulation in a Centrifugal Pump at Design and Off-Design Conditions”, International Journal of Rotating Machinery, Vol. 2007, Article ID 83641.
2. K.W.Cheah, T.S. Lee and S.H. Winoto, 2010, “Numerical Study of Inlet and Impeller Flow Structures in Centrifugal Pump at Design and Off-design Points”, International Journal of Fluid Machinery and Systems, Vol. 4, No.1, pp. 25-32
3. K.W.Cheah, T.S. Lee and S.H. Winoto, 2011, “Unsteady Analysis of Impeller-Volute Interaction in Centrifugal Pump”, International Journal of Fluid Machinery and Systems, Vol. 4, No. 3, pp. 349-359